UNIVERSITY OF CAMBRIDGE

Department of Chemical Engineering

A Sensor for Combustion Thermometry based on Blue Diode Lasers

Iain Stewart Burns

Magdalene College

This dissertation is submitted for the degree of Doctor of Philosophy
8th February 2006

A sensor for combustion thermometry based on blue diode lasers

Iain Stewart Burns

Summary

Spatially-resolved measurements of flame temperature have been demonstrated with diode lasers for the first time. The technique is based on the use of blue diode lasers to perform laser-induced fluorescence on indium atoms seeded to the flame. Temperature measurements have been carried out in laminar flames both by the two-line atomic fluorescence technique, and also by a novel line-shape thermometry method that requires the use of only a single diode laser.

The first part of this work involved the development of blue extended cavity diode lasers with favourable tuning properties. Two custom-designed extended cavity diode lasers (ECDL) have been built, emitting at wavelengths of around 410 nm and 451 nm respectively. These devices are capable of mode-hop free tuning over ranges greater than 90 GHz. The performance of these devices exceeds that of commercially available systems and a patent application has been filed.

High resolution fluorescence spectroscopy has been performed on both the $5^2P_{1/2} \rightarrow 6^2S_{1/2}$ and $5^2P_{3/2} \rightarrow 6^2S_{1/2}$ transitions of indium atoms seeded at trace quantities into atmospheric pressure flames. In both cases, the spectra obtained show excellent agreement with a theoretical fit based on the individual hyperfine components of the transition.

The two ECDLs have been used to build a sensor for the measurement of temperature in combustion systems. It is much simpler, more compact, less expensive, and more versatile than any previously existing device. The two lasers were used sequentially to probe indium atoms seeded to the flame. The ratio of the resulting fluorescence signals is related to the relative populations in the two sub-levels of the spin-orbit split ground state of indium, and thus to the temperature. Temperature measurements have been successfully performed in a laminar flame and the data thus obtained do not need to be corrected by any 'calibration constant'. This novel thermometry technique offers a robust alternative to traditional methods involving bulky high power lasers. A further development has been made by demonstrating a fluorescence line-shape thermometry technique requiring only a single diode laser excitation source.

Progress has been made towards the goal of rapid temperature measurements appropriate to the study of turbulent flames. This involved the development of a simple technique for actively locking the wavelength of the blue diode laser to a resonance line of the tellurium molecule. A high-speed thermometry system would work by rapidly switching between the two locked laser beams using an optical modulator.

Preface

This dissertation is the result of my own work and includes nothing which is the outcome of work done in collaboration except where specifically indicated in the text.

In total this document contains approximately 43000 words.

I confirm that the work contained in this dissertation, or any part thereof, has not been submitted for any other degree.

The research presented here has been carried out at the Department of Chemical Engineering, University of Cambridge between January 2003 and January 2006.

Acknowledgements

I would like to express my gratitude to the following people and organisations:

Johan Hult, who has been the main supervisor of this project. It has been a privilege to work with Johan and I have benefited immensely from his clear explanations and his boundless enthusiasm for research. Thanks to Johan also for organising our research visit to Lund, and giving me the chance to try fishing in the lakes of Småland.

Clemens Kaminski, the overall supervisor, for the opportunity to work on an exciting research project in his laboratory, and for his continuous enthusiasm, which has been a source of motivation.

Georg Hartung, for his energetic contribution to our experimental collaboration.

All other members of the Laser Analytics Group for providing a positive research environment.

John Black, of Rolls-Royce plc for his helpful tuition on performing CARS experiments, and for the loan of experiment equipment.

Paul Ewart, of Oxford University for the loan of experimental equipment.

Wei-Yao Ma, of the electronics workshop for fabricating certain components.

The Paul Instrument Fund of the Royal Society for funding the blue-diode laser TLAF project.

The UK Engineering and Physical Sciences Research Council (EPSRC) for providing me with a CASE studentship.

Rolls-Royce plc for partially funding this studentship.

St John's College Cambridge, for providing me with a Research Fellowship, which allows me to continue my research here.

All the lads from Magdalene-Emma grad football team for the ups and downs of the past three seasons.

My family for their constant encouragement and support.

And finally, special thanks to Dana Niry.

List of Publications

Peer-reviewed journal articles:

I.S. Burns, J. Hult, C.F. Kaminski,
"Spectroscopic use of a novel blue diode laser in a wavelength region around 450 nm,"
Applied Physics B, 79, 491, 2004

J. Hult, I.S. Burns, C.F. Kaminski,
"Measurements of the indium hyperfine structure in an atmospheric-pressure flame by use of diode-laser-induced fluorescence,"
Optics Letters, 29, 827, 2004

J. Hult, I.S. Burns, C.F. Kaminski,
"Two-line atomic fluorescence flame thermometry using diode lasers,"
Proceedings of the Combustion Institute, 30, 1535, 2005

J. Hult, I.S. Burns, C.F. Kaminski,
"Wide bandwidth mode-hop free tuning of extended cavity GaN diode lasers,"
Applied Optics, 44, 3675, 2005

J. Hult, I.S. Burns, C.F. Kaminski,
"High repetition-rate wavelength tuning of an extended cavity diode laser for gas phase sensing,"
Applied Physics B, 81, 757, 2005

I.S. Burns, J. Hult, C.F. Kaminski,
"Use of $^{130}Te_2$ for frequency referencing and active stabilisation of a violet extended cavity diode laser,"
Spectrochimica Acta Part A, in press 2006

I.S. Burns, J. Hult, G. Hartung, C.F. Kaminski,
"A thermometry technique based on atomic lineshapes using diode laser LIF in flames,"
Submitted for publication, 2006

Conference Publications:

I.S. Burns, J. Hult, C.F. Kaminski,

"Laser induced fluorescence spectroscopy in flames using diode lasers,"
LACEA, IX, 2004

I.S. Burns, J. Hult, C.F. Kaminski,
"Diode laser induced fluorescence spectroscopy for combustion thermometry,"
Journal of Physics: Conference Series, 15, 201, 2005

J. Hult, I.S. Burns, C.F. Kaminski,
"New Light Sources – Wide Tuning Range and Rapid Scanning Blue Extended Cavity Diode Lasers,"
LACSEA, X, 2006

I.S. Burns, J. Hult, C.F. Kaminski,
"Frequency locking of blue/violet extended-cavity diode lasers for dynamic sensing applications,"
LACSEA, X, 2006

Patent Application:

J. Hult, I.S. Burns, C.F. Kaminski,
"An Extended Cavity Diode Laser",
European Patent Application, Reference number: WO2005008852, 13th July 2004

Table of Contents

Chapter 1

Introduction

It seems likely that, for the foreseeable future, the majority of the global energy supply will continue to be generated by burning hydrocarbon fuels. It is therefore essential to gain a better understanding of combustion, in order to develop automotive engines, gas turbines, and other devices, that use fuel more efficiently and emit minimal quantities of harmful pollutants such as soot and NO_x. The experimental study of flames and engines is an important part of this effort and laser-based diagnostic techniques represent a unique tool for performing such investigations.

Combustion environments are typically characterised by elevated temperatures, turbulent flow patterns and complex chemistry. The design of practical combustors such as gas turbine engines promotes turbulence in the combustion zone to enhance mixing of fuel and air. Turbulence is a phenomenon that has fascinated scientists for many centuries, and it is still not fully understood. The chemical reactions occurring simultaneously complicate matters considerably. Although various types of computational models do exist, which can describe some aspects of the behaviour of turbulent flames, they are still unable to give reliable predictions of such

crucial phenomena as NO_x formation or flame extinction. Experimental investigation is therefore an essential part of the effort to develop a better understanding of turbulent reacting flows.

Combustion devices represent a challenging environment in which to make accurate physical measurements. This is because the quantities being measured, such as temperature and pressure, and the concentrations of various chemical species, are all subject to rapid turbulent fluctuations. It is therefore necessary to make very rapid measurements to capture this dynamic behaviour. The flame is also highly spatially inhomogeneous, and it is therefore desirable to probe a very small point within it, or in some cases a line or planar surface composed of many such points. Laser based techniques are the only way to fulfil these criteria of high temporal and spatial resolution.

Various laser techniques have been developed over the past 30 years for spatially resolved measurements of temperature and of species concentrations in flames (Eckbreth 1996; Kohse-Höinghaus et al. 2005). These involve focussing a laser beam to a point in the flame and detecting light that is scattered from that point due to interactions of the laser with the molecules present. These interactions may involve Rayleigh Scattering, Raman Scattering, laser-induced fluorescence, or other more complex phenomena. A common feature of all of these previous implementations has been the use of high-power lasers, whose cost and complexity has limited their use to a small number of research laboratories.

A new technique, described in this dissertation, instead employs compact and inexpensive diode lasers, similar to those used in compact-disc players. The results that are presented here represent the first use of diode lasers for spatially resolved measurements of flame temperature. Practicality and

cheapness are far from being the only advantages of the novel diode-laser flame-temperature sensor. The diode lasers employed are continuous wave sources and are thus capable of much higher measurement repetition rates than the pulsed lasers that have frequently been used in the past. The spectral purity and stability of diode lasers is also far superior to that of typical dye lasers and this allows very accurate measurements to be performed.

Although they have never before been used for spatially-resolved temperature measurements, diode lasers have been used extensively in practical sensors. This includes increasingly widespread application in process monitoring on chemical plants and is mainly focussed on the measurement of species concentration. Existing diode laser technologies are almost exclusively based on absorption spectroscopy, which is a line-of-sight technique. This can only be used to measure average temperatures in situations where the temperature is fairly homogeneous along the entire optical path of the laser (clearly this is not the case in turbulent combustion environments). That is because the strength of the signal through which temperatures are inferred has a non-linear relationship with temperature. If the temperature varies along the laser beam path then averaging will introduce large unaccountable errors, by causing a bias towards lower temperatures.

The objective of the present work was to develop a new diode laser method for the measurement of combustion temperatures with high-spatial resolution, in contrast to previous line-of-sight absorption techniques. This was done with novel blue diode lasers using the two-line atomic fluorescence (TLAF) technique based on indium seeded to the flame. Considerable technological development was necessary to improve and adapt the wavelength tuning characteristics of the blue diode lasers to suit this application. The general

aim is to apply this sensor to turbulent combustion environments but shorter term goals were to perform high-resolution spectroscopy on the seeded indium atoms, and to demonstrate spatially resolved temperature measurements in a laminar flame.

This dissertation is structured as follows. In Chapter 2, the development of a custom designed blue/violet extended-cavity diode laser (ECDL) device is presented in detail. Two such lasers were built and the characterisation of their spectral properties and wavelength tuning capabilities is described. Chapter 3 addresses the use of these ECDL systems to perform high-resolution spectroscopy of atomic indium in flames. Subsequently, Chapter 4 describes two-line atomic fluorescence temperature measurements, which were successfully performed in laminar flames. Some theoretical aspects of the TLAF technique are also discussed here with the goal of optimising the accuracy of the sensor. It was discovered that it is also possible to extract accurate temperature data from the line-shape of the LIF spectrum acquired using a *single* diode laser. This is a further novelty, which allows for an even more compact experimental set-up. The results of this alternative analysis are discussed in Chapter 5. A key objective of the present work was to investigate the possibility of substantially increasing the temporal resolution and repetition rate of TLAF thermometry to allow the study of rapid temperature fluctuations in dynamic combustion environments. A possible strategy to achieve this is reported in Chapter 6. Here the laser wavelengths are actively locked to $^{130}Te_2$ lines, and an optical chopper is used to switch rapidly between the two beams. This strategy has the advantage that the diode lasers are always at full power so the signal-to-noise ratio is maximised. Finally, in Chapter 7, a summary is presented of the conclusions that may be

drawn from this research, and possible future directions in this research area are highlighted.

Prior to this, though, the following section provides a summary of the relevant literature and background. Firstly, a very brief discussion of the principles of combustion is given, making clear that accurate temperature measurements are crucial to gaining a better understanding of the process. This is followed by a description of the advantages and shortcomings of existing techniques for temperature measurement involving high-power lasers. Diode lasers are increasingly being used in process instrumentation and measurement. Therefore, a brief description is given of the basic operation of diode lasers and of the different types of devices available. This leads on to an overview of some previous diode laser applications in gas-phase sensing, which are principally concerned with absorption spectroscopy in the near infra-red spectral region. The practice of making temperature measurements via absorption spectroscopy is described and the reasons why this is unsuitable to probe turbulent combustion (or *any* inhomogeneous environment) are highlighted through simple calculations. Some of the early uses of blue diode lasers are then outlined, with particular attention to applications in spectroscopy of metal atoms.

1.1 Combustion Processes

The flame results from an interaction between complex processes involving multiple chemical reactions and simultaneous transfer of heat and mass. Flames can be categorised according to whether the flow is turbulent or laminar, and whether or not the reactants are premixed; the simplest case is a premixed laminar flat flame. The flat-flame can be stablilised, for example on

a burner plate consisting of a porous plug (McKenna burner) or of a plate with a large number of capillary holes drilled into it (Mèker burner). By contrast, a cone-shaped premixed flame can be stabilised on a Bunsen burner. The flat-flame is commonly used in experimental studies since there are only gradients in one spatial dimension making it more amenable to modelling.

The premixed flame propagates counter to the direction of fluid flow by the back-diffusion of radicals formed in the reaction zone (especially H since it has a high diffusion coefficient), and by conduction of heat to the reactants (Warnatz et al. 1996). At steady-state, these fluxes are exactly balanced by the convective transport so that the reaction zone remains at a fixed location. The resulting profiles of temperature and major species mole fraction for a typical premixed flame are shown in Figure 1.1. This temperature and composition profile was modelled using the PREMIX code (Kee et al. 1985), which was implemented by Mr G. Hartung. The conductive heat transfer leads to a gradual rise in temperature in the 'pre-heat' zone: low temperature chemistry takes place in this region involving the pyrolysis of the fuel molecules. When the temperature and radical concentrations reach a certain level, highly exothermic chain reactions are initiated. In this 'reaction zone' there are extremely steep gradients in temperature and species mole fractions, as depicted in Figure 1.1. The exothermic reactions slow down a short distance downstream where most of the reactants have been consumed. In the post-combustion region, residual CO oxidises slowly to form CO_2.

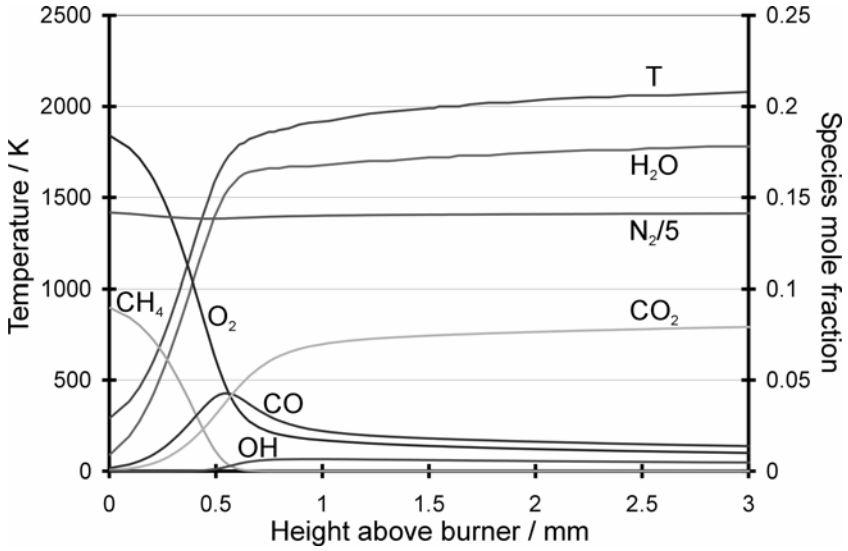

Figure 1.1. Profiles of temperature and major species mole fractions in a premixed flat flame of methane and air with equivalence ratio of ϕ = 1.0 (Calculated using the PREMIX code).

Note that the mole fraction of inert N_2 stays approximately constant throughout the stoichiometric methane-air flame because the global reaction involves the same number of moles of reactants as of products: this is an untypical situation.

There have been continuing developments in the modelling of laminar flames over a prolonged period of time (Warnatz et al. 1996; Westbrook et al. 2005). For example, the CHEMKIN mechanism (Kee et al. 1989) can be used together with the PREMIX code (Kee et al. 1985) for modelling of premixed one-dimensional laminar flames, as shown in Figure 1.1. Such models, however, do not give reliable predictions of the concentrations of minority components such as important pollutant species like NO and soot, whose rates of formation are highly temperature dependent. In studies of NO chemistry (Gasnot et al. 1999), or of sooting flames (Richter et al. 2005), it was

necessary to input the experimentally measured temperature distribution of the flame to the PREMIX code rather than simultaneously solving an energy balance equation. The accuracy of the model predictions therefore depend crucially on the quality of the temperature data. This is one of the reasons why laser diagnostic techniques have such a central role in the field of combustion research. A range of flame thermometry techniques will be described below and it will become apparent that many of these methods have certain disadvantages, both in terms of practicality and accuracy.

In contrast to the laminar flames described above, practical combustion processes for energy generation and transportation are invariably turbulent, and are often non-premixed (Warnatz et al. 1996). The turbulent flow-field promotes rapid mixing of fuel and air and thus maximising the efficiency. The simplest assumption that can be made about turbulent flames is that the fuel and air react to equilibrium as soon as they are mixed (Warnatz et al. 1996). The degree of mixing is described by the mixture fraction (ξ), which is based on the concentration of chemical elements, since they are neither created nor destroyed by reaction.

$$\xi = \frac{Z_i - Z_{i2}}{Z_{i1} - Z_{i2}} \tag{1.1}$$

Here, Z_i is the mass fraction of the element i, and the index '1' refers to the air and the index '2' to the fuel. The mixture fraction ξ thus takes values between 1 and 0 as mixing proceeds, and represents the mass fraction of fluid material that originated from the air. A single species conservation equation can then be written in terms of the mixture fraction (Warnatz et al. 1996).

$$\frac{\partial(\rho\xi)}{\partial t} + \nabla\cdot(\rho\boldsymbol{\upsilon}\xi) - \nabla\cdot(\rho D\cdot\nabla\xi) = 0 \qquad (1.2)$$

Here, ρ is the local density, D is the diffusion coefficient, and $\boldsymbol{\upsilon}$ is the velocity vector. This equation is saying that the change in the concentration, in an infinitesimal control volume, of material originating from the air stream is equal to the net flux into the control volume due to diffusion minus the net flux outwards due to convection.

Some further assumptions are often made including that the system is adiabatic, that temperature, density and species mass fractions are functions of ξ only, and the Lewis number (Le) is equal to unity:

$$Le = \frac{\lambda}{D\rho c_p} = 1.0 \qquad (1.3)$$

Here, λ is the thermal conductivity. This means that the same diffusion coefficient applies for energy and for mass. Despite these simplifying assumptions, the solution of the equations for turbulent mixing remains a formidable challenge, requiring the use of advanced computational strategies that will not be discussed here.

Due to the large number of assumptions being made, it is necessary to test the validity of the model by comparison to experimental data. One of the crucial parameters for model validation is the temperature distribution. The fluctuations in temperature at a point in a turbulent flame are, of course, stochastic in nature. Nevertheless, experimental results for the mean

temperature and magnitude of temperature fluctuations at different locations in the burner are amongst the parameters that can be compared to model predictions (Barlow et al. 2005).

Due to the rapid dynamics of turbulent flames, an essential characteristic of any measurement technique is to achieve high temporal and spatial resolution (Eckbreth 1996). The finest scale over which a temperature gradient can exist in a turbulent flow is the Batchelor lengthscale (λ_B) (Batchelor 1959):

$$\lambda_B = D^{1/2}\left(\frac{\nu}{\langle\varepsilon\rangle}\right)^{1/4} \tag{1.4}$$

Here, ν is the kinematic viscosity, D is the diffusivity, and $\langle\varepsilon\rangle$ is the mean rate of kinetic-energy dissipation, a measure of how turbulent the flame is. The highest frequency present in the flame can be described by a related parameter, the convective Batchelor frequency (f_B) (Wang et al. 2005):

$$f_B = \frac{U}{2\pi\lambda_B} \tag{1.5}$$

Here, U is the local mean velocity. The degree of turbulence of non-premixed jet-flames is characterised by the source Reynolds number Re_d:

$$\mathrm{Re}_d = \frac{U_0 d}{\nu_0} \tag{1.6}$$

Here, U_0 is the jet exit velocity, ν_0 is the kinematic viscosity of the fuel, and d is the diameter of the fuel nozzle. As an example, the Batchelor length-scale and frequency in a particular standard laboratory-scale non-premixed flame ('DLR_A', Re_d = 15,200 (Wang et al. 2005)) are in the range of 200 – 500 μm and 3 – 12 kHz respectively depending on the distance from the jet nozzle. These therefore give an indication of the spatial- and temporal-resolutions that are required for diagnostic techniques to resolve the fluctuations in such systems.

1. 2 Measurement of flame temperature

In this section, an overview of flame thermometry techniques is presented and their strengths and weaknesses are discussed. It will emerge that the laser diagnostics are the only techniques capable of achieving in situ measurements with both high temporal and spatial resolution, and without perturbing the flame (Eckbreth 1996). It will become clear that a desirable criterion for any new measurement tool would be to incorporate these advantages into a system that is much more compact, cheaper, and simpler to implement. A new technique with the potential for high repetition-rate measurements or for use in particle laden environments would also be attractive. It will become apparent here and in later Chapters that the blue diode laser-induced-fluorescence technique developed here possesses all of these favourable characteristics.

1.2.1 Thermocouples

In the past, flame temperature has been measured using thermocouples: a simple method with a number of limitations. The thermocouple is a solid

metal object inserted into the flame and as a result it may perturb flow patterns or catalyse certain reactions (Hayhurst and Kittelson 1977); radiative heat transfer to the surrounding gas must also be carefully taken into account, and the effects of conduction and convection of heat should be corrected for. In addition, the thermocouple takes a finite period of time to equilibrate with the surroundings, and there is a limitation on its physical dimensions, which results in temporal and spatial averaging.

1.2.2 Optical Techniques

By contrast, laser techniques, despite their technical complexity, offer numerous advantages. These are non-intrusive, *in-situ* techniques whose high temporal- and spatial-resolution are well-suited to probing turbulent environments. In contrast to physical probe techniques, there is no inherent upper limit on the temperature that can be measured. Non-laser optical techniques do exist, including pyrometry, line-reversal and chemiluminescence, but these are not widely used as they are line-of-sight methods and as a result spatial averaging introduces large errors in temperatures measured in inhomogeneous systems.

1.2.3 Rayleigh Scattering

One possible laser-based thermometry technique is Rayleigh scattering. It involves an elastic molecular interaction and therefore the scattered wavelength is equal to the incident wavelength. The signal is directly proportional to the number density of atoms or molecules in the probe volume, but a different proportionality constant, or Rayleigh cross-section, applies for each species. It is therefore a pressure measurement (assuming

that the mixture composition is known) but temperature can be inferred by employing an appropriate Equation of State, such as the Ideal Gas Law. Rayleigh temperature measurements can be performed either by assuming that the mean Rayleigh cross-section is approximately constant across the whole flame (Wang et al. 2005), or by making a simultaneous multi-species concentration measurement by Raman scattering. In the latter case, an iterative process is required to find the temperature since the Raman signal is a function of both temperature and composition. Mie Scattering causes significant interference with this technique and, as a consequence, Rayleigh scattering can only be used to probe very clean environments. Nevertheless, simultaneous Raman-Rayleigh measurements have been used to study turbulent non-premixed flames whose compositions were carefully chosen to avoid soot formation (Barlow et al. 2005; Geyer et al. 2005).

1.2.4 Raman Scattering

Spontaneous Raman Scattering is, by contrast an inelastic process, so the scattered light is frequency-shifted with respect to the incident wave by an amount that is characteristic of molecular vibrations and rotations. It can therefore be used for species specific concentration measurements. The Raman Scattering process involves excitation of a molecule (typically from the ground state) to a virtual energy level and subsequent decay to a ro-vibrational level lying above the ground state. If the emitted radiation is lower in frequency than the incident beam, it is known as Stokes shifted; the opposite being anti-Stokes shifted. A single laser can be used to excite all of the Raman transitions in a particular molecule. The resulting emission can be resolved with a spectrometer and used to determine multiple species

concentrations and temperature. Nevertheless, the signal strength is extremely weak (typically around 10^{14} less intense than the incident laser light (Eckbreth 1996)) which makes it impractical in many combustion environments where there is significant background radiation. The complexity and cost of the experimental set-up required for spontaneous Raman scattering has restricted its use to a small number of research laboratories.

1.2.5 Coherent anti-Stokes Raman scattering

Coherent anti-Stokes Raman Scattering (CARS) was developed in the 1970's by Taran and co-workers (Moya et al. 1975) and has been applied to various practical combustion situations to perform single-shot temperature measurements with high spatial and temporal resolution. The theory and practical considerations for the CARS technique are described in detail by Eckbreth (Eckbreth 1996). In the same way as for Raman scattering, the high cost of assembling the elaborate experimental set-up required has prevented the use of CARS from becoming widespread.

CARS overcame some of the disadvantages of the earlier temperature measurements such as spontaneous Raman scattering, which suffers from a low signal-to-noise ratio (SNR). Part of the reason for the improved SNR is that the CARS signal is generated as a coherent beam rather than being dispersed in all directions as in spontaneous Raman scattering. This means that the entire signal can be collected through a narrow slit, thereby reducing interference from incoherent background light. CARS is a non-linear optical process whose signal strength is approximately proportional to the third power of the excitation intensity. High power densities are required before

non-linear effects are observable and the first applications emerged with the development of suitable high-power lasers.

A simplified version of the CARS process is shown in Figure 1.2. The CARS signal is generated by the interaction of three incident beams, which are focussed in the measurement volume. Two of these, known as the pump beams are at frequency ω_1 and are typically the frequency-doubled output of a pulsed Nd:YAG laser. The other, known as the Stokes beam, has frequency ω_2 and the output from a Nd:YAG pumped dye laser is generally used. The two input waves drive molecular vibrations coherently in the species being probed because their frequency difference ($\omega_v = \omega_1 - \omega_2$) corresponds to a Raman active vibrational resonance. Another photon of frequency ω_1 scatters inelastically off the vibrating molecule with a gain in energy corresponding to ω_v. The signal beam is generated coherently at frequency $\omega_3 = \omega_1 + \omega_v$ and is blue shifted with respect to the pump beams. It is thus easily discriminated against the incident light.

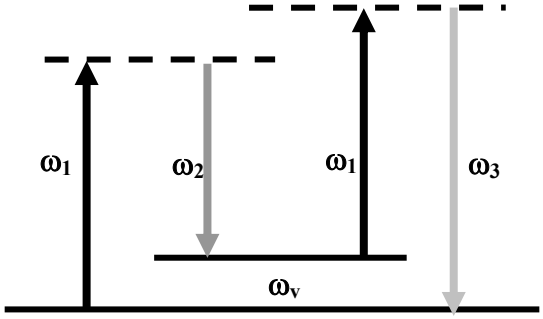

Figure 1.2 Schematic Energy Level Diagram of the CARS process

Vibrational N_2 CARS gives good temperature sensitivity across the full range of combustion temperatures and has been successfully used for thermometry in practical combustion devices including gas turbines (Eckbreth 1980),

internal combustion engines (Stenhouse et al. 1979) and coal furnaces (Aldén and Walin 1985). One difficultly that has restricted the use of CARS from becoming widespread is that it requires a very large amount of complex optics and a large spectrometer in addition to the Nd:YAG laser and dye laser, making it a very expensive technique. Furthermore, the alignment of the optics in order to achieve phase matching of the pump and Stokes beams and to direct the signal beam toward the spectrometer is not trivial and can be very time consuming. Its inherent complexity and non-linear signal generation process means that it is not at all suitable for use in on-line monitoring, for example, of an industrial process.

Other drawbacks of CARS are that, since the signal is generated by the interaction of three laser beams, it is not amenable for use in multi-point measurements or line-imaging. Shot-to-shot fluctuations in the spectral profile of the dye laser can introduce errors in measured temperature. Furthermore, the CARS technique suffers from interference in sooting flames caused by Swan band absorption by C_2 radicals formed by laser-induced decomposition of soot (Eckbreth and Hall 1979).

1.2.6 Two-line Laser Induced Fluorescence

Another class of flame temperature measurement is based on laser-induced fluorescence. A two-line laser induced fluorescence (LIF) technique is the basis for the novel diode-laser flame sensor developed during the present work. The approach probes the relative populations of two energy levels of an atomic or molecular species, which is assumed to be in thermal equilibrium with the surrounding flame. The temperature can then be inferred from the Boltzmann equation.

$$\frac{N_1}{N_0} = \frac{g_1}{g_0} \exp\left(\frac{\varepsilon_0 - \varepsilon_1}{kT}\right) \tag{1.7}$$

Here, for energy level i, ε_i is the energy relative to the ground state, N_i is the population and g_i is the degeneracy. The basis for a simple implementation of the two-line LIF technique is summarised in an energy level diagram in Figure 1.3:

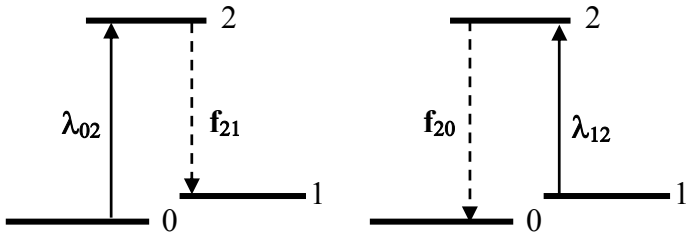

Figure 1.3 Two-line LIF energy level diagram

An atomic or molecular probe species should be selected that has an excited state (1) sufficiently close to the ground state (0) to be significantly populated at flame temperature. Two lasers with wavelengths λ_{02} and λ_{12} are used sequentially to excite the 0→2 and 1→2 transitions of the seeded atoms. The resulting fluorescence corresponding to each transition is proportional to the population in the respective lower states 0 and 1.

Taking the example of indium as the probe species, since it will be employed in the present research, the technique works as follows: a laser emitting near 410.2 nm is used to excite the $5^2P_{1/2} \rightarrow 6^2S_{1/2}$ transition. The excited indium will subsequently fluoresce both to the $5^2P_{1/2}$ level and to the $5^2P_{3/2}$ level (which lies about 2213 cm^{-1} (NIST 2006) above the $5^2P_{1/2}$ ground state).

Through the use of an appropriate filter in front of the detection system, only fluorescence corresponding to $6^2S_{1/2} \rightarrow 5^2P_{3/2}$ is observed. Another laser emitting near 451.1 nm probes the $5^2P_{3/2} \rightarrow 6^2S_{1/2}$ transition and resulting fluorescence corresponding to $6^2S_{1/2} \rightarrow 5^2P_{1/2}$ is observed by a second detector. The ratio of the fluorescence signals detected is related to the temperature by an equation that is derived from the Boltzmann approximation, as will be set out in greater detail in Chapter 4. The common upper state means that the effects of collisional quenching cancel out. The choice of indium as the seeding species is justified by the sensitivity of the relative population of the $5^2P_{1/2}$ and $5^2P_{3/2}$ states over the entire range of temperatures of interest in technical combustion.

Two-line atomic fluorescence (TLAF) thermometry has only been previously performed using high-power pumped dye lasers such as Argon ion laser pumped continuous-wave dye lasers (Dec and Keller 1986), and was later developed into a 2D imaging tool by using pulsed dye lasers (Kaminski et al. 1998). The present goal is to apply this method using much smaller, cheaper and more compact blue diode lasers. One key advantage of TLAF is the possibility to make measurements in the presence of strong particulate scattering using a non-resonance fluorescence detection scheme (Engström et al. 2000), and this may make blue diode laser TLAF suitable for measurements in sooting environments for which there is presently no alternative temperature measurement technique. The poor performance of other thermometry techniques in particle-laden flames has been described above. Another potential benefit of the blue diode laser TLAF scheme is the high data-acquisition rate obtainable, something that is impossible with

techniques such as CARS, which are restricted by the repetition-rate of the Nd:YAG laser of around 10 Hz.

Two-line temperature measurement techniques have also been implemented using native molecules in the flame such as the OH radical as the probe species (Cattolica 1981). This technique has been widely employed for temperature imaging with either OH (Lee et al. 1993) or NO (Seitzman et al. 1994) as the target molecule. The accuracy of such temperature measurements is limited because the influence of quenching does not cancel out as it does in two-line *atomic* fluorescence experiments: there is vibrational and rotational energy transfer within the excited state prior to the spontaneous emission. Greater accuracy can be achieved by multi-line imaging of fluorescence, which involves scanning the laser wavelength over many molecular transitions of OH (Atakan et al. 1997) or NO (Bessler and Schulz 2004) and fitting a theoretical spectrum to the data obtained for each pixel. Such laser scanning can only be done slowly so this method is only suitable for laminar flames, where low temporal resolution is acceptable. The OH LIF imaging requires the use of a frequency-doubled tunable Nd:YAG pumped dye laser, whereas the multi-line NO temperature imaging is typically done with a tunable Excimer laser. The blue diode laser TLAF technique being presented here offers similar accuracy for laminar flame measurements to these multi-line techniques, but is much more convenient to perform, and has the potential for high-temporal resolution measurements.

1.3 Diode Lasers

This section begins by giving a general overview of the principles behind the operation of diode lasers, before discussing a few selected examples from the

wide variety of applications of diode lasers to practical spectroscopy. Previous examples of the use of diode laser absorption spectroscopy to measure gas temperature are mentioned, and the inherent inapplicability of such thermometry to inhomogeneous systems is highlighted. Finally, attention is drawn to previous applications of blue diode lasers, which are the excitation sources used in the present project.

1.3.1 Diode laser structure

Diode lasers are compact, inexpensive, and durable; they also possess very high spectral purity and have favourable wavelength tuning properties. This has led them to be used in a diverse array of situations ranging from chemical process instrumentation to fundamental atomic physics experiments. A very brief description will be given of the basic characteristics of diode lasers and of some different types of devices that have been produced by modifications to the original design. Much more extensive information on this subject can be found elsewhere (Sands 2004).

Diode lasers are fabricated from semi-conductors. The semiconductor is a solid crystal in which the bonds between atoms are covalent, such as Si, Ge, or GaAs. In a solid, there are no sharp energy levels (like in gases, where the atoms are far apart) but instead the energy levels exist in a series of states of closely spaced energies known as ‘bands’. These bands arise because of the interaction of electrons with each other: the levels shift slightly to avoid electrons from different atoms overlapping in space, a manifestation of the Pauli Exclusion Principle. Electrons that are bound to atoms are described as residing in the ‘valence band’. Bonding electrons can be released by a small amount of energy, thereby being transferred to the ‘conduction band’. The

energy required to overcome the bond is known as the 'forbidden band gap', as illustrated in Figure 1.4.

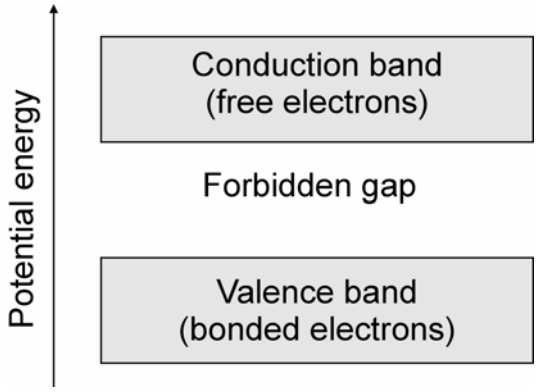

Figure 1.4. A general representation of the band structure in semiconductors. Adapted from Sands (Sands 2004).

Electrons do not get into the conduction band by energy from an electric field; instead a certain small fraction of the electrons reside in the conduction band due to thermal excitation. Electrical conduction involves a change of state either within the valence band or within the conduction band. Conduction within the conduction band can be interpreted as free electrons permeating through the crystal lattice; the current is proportional to the number of electrons in the conduction band. By contrast, conduction within the valence band corresponds to an electron jumping from one atom to another atom which is deficient in an electron. This can alternatively be thought of as the lack of electron, or a 'hole' being transported in the opposite direction to the electric current. In this case, the current depends on the number of holes; i.e. the number of empty states in the valence band. Electrons and holes are thus known as carriers; if there are more electrons than holes, the electron is the majority carrier – a so-called 'n-type semiconductor'; in the converse situation, the hole is the majority carrier – 'p-type seminconductor'. At

equilibrium, the product of the number of the electrons (n) with the number of holes (p) is defined as follows:

$$np = n_i^2 \tag{1.8}$$

Here, n_i is defined as the 'carrier density'. The number of electrons or holes can be changed by doping. This involves the introduction to the crystal of a dopant atom which has a different valency to the host, and may act as an electron donor (higher valency) or an electron acceptor (lower valency). For example, in the case of a silicon crystal (Group IV), phosphorus (Group V) would be a donor and boron (Group III) would be an acceptor.

The emission of light from a semi-conductor can result from recombination of an electron and a hole; i.e. an electron in the conduction band occupies an empty state in the valence band. In the reverse of this process, electrons in the valence band can be promoted to the conduction band due to thermal fluctuations, or through the absorption of a photon with energy equivalent to the band gap. An excess of carriers is needed for significant light emission to occur (i.e. $np \gg n_i^2$): this is a non-equilibrium situation, which promotes a high rate of recombination. This non-equilibrium state cannot exist in a pure semi-conductor material; it is instead achieved by means of a 'p-n junction', which allows charge to be injected into the semiconductor so that laser action can take place. An electrical current above a threshold value (I_{th}) is required to maintain the population inversion. Early diode lasers had very high threshold currents and thus had to be operated at cryogenic temperatures. During the development of diode lasers, various advances in material

properties allowed the threshold current to be reduced, thus permitting continuous-wave (cw) operation at ambient temperature. Typically, the p-n junction is fabricated by epitaxial growth of one semiconductor material on the surface of another to form a heterostructure laser. In practice, a double heterostructure is used consisting of a thin active region sandwiched between n-type and p-type layers. A diagram showing the basic structure is shown in Figure 1.4.

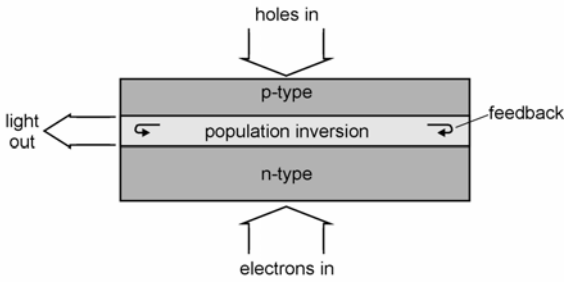

Figure 1.4. Schematic diagram of basic diode laser structure. Adapted from Sands (Sands 2004).

The diode laser has features that are analogous to other laser types. The laser action begins within the gain medium with the spontaneous emission of light. This light can be amplified by the process of stimulated emission in the active region, leading to the build up of coherent radiation. The ends of the active region act as parallel mirrors, providing optical feedback. These mirrors form a Fabry-Perot cavity so the possible wavelengths that can propagate are restricted to those allowing an integer number of half-wavelengths in the cavity. These wavelengths correspond to longitudinal modes, and are separated by the free-spectral range of the cavity:

$$\Delta\nu = \frac{c}{2nl} \tag{1.9}$$

Here, l is the cavity length and n is the refractive index of the diode material. One of the end mirrors is partially transmitting and allows a portion of the light to escape from the cavity as the output beam. The wavelength of the laser light depends on the size of the band gap in the semiconductor. Diode lasers can achieve gain over a range of frequencies; therefore, Fabry-Perot diode lasers typically emit laser light at a number of different frequencies, corresponding to several longitudinal modes. The gain curve can be shifted by altering the population dynamics of the p-n junction. This can be done by changing either the diode temperature or the injection current and leads to coarse tuning of the laser emission wavelength.

Advanced designs of diode lasers can allow single-mode emission. These include the vertical-cavity surface-emitting laser (VCSEL), and the distributed feedback laser (DFB). The VCSEL, as the name implies, has mirrors above and below the active region, rather than at the ends. This results in a much shorter cavity with a much higher free spectral range (according to Eqn. 1.9), causing only one mode to be active within the diode laser gain profile. The DFB laser, by contrast, incorporates a grating into the fabric of the diode which leads to the propagation of one particular mode. These specialist lasers also have favourable wavelength tuning properties. Their availability is, however, restricted to certain spectral regions: while DFB lasers can be fabricated to emit at any wavelength between 760 nm and 2.5 μm (Seufert et al. 2004), VCSELs are only available in certain narrow regions of the near infra-red region, and thus only standard Fabry-Perot diode lasers emit in the

visible spectral range. It is possible to obtain single-mode radiation from Fabry-Perot diode lasers by using external components to retro-reflect wavelength selective feedback into the diode chip. One common example of this is the extended-cavity diode laser (Ricci et al. 1995), which forms the subject of Chapter 2 and will not be discussed further here. The next section provides an overview of the spectroscopic applications of diode lasers.

1.3.2 Absorption Spectroscopy

The vast majority of previous applications of diode lasers in combustion diagnostics have involved tunable diode laser absorption spectroscopy (TDLAS). This is a path-integrated technique and is thus unsuitable for spatially resolved measurements. Nevertheless, it has been used to measure species concentrations in a great variety of situations ranging from industrial monitoring to biomedical diagnostics. The advantages of diode lasers mean that they not only constitute a research tool but also have been incorporated in to robust sensor devices for routine use.

A large proportion of the absorption spectroscopy measurements that have been performed were done with near infra-red (NIR) diode lasers operating in the 0.9-3 μm range. The widespread and inexpensive availability of devices emitting in this wavelength range resulted from their use in telecommunications equipment. In fact, molecular transitions in the NIR region are generally weak because they are from ro-vibrational overtone bands rather than fundamental bands. Therefore, long path length multipass absorption cells are often used in order to achieve greater levels of absorption (Herriott et al. 1964). An even greater sensitivity can be achieved by incorporating the gas sample within a resonant optical cavity, as is done in

cavity-ring-down spectroscopy (Romanini et al. 1997), and related techniques such as cavity enhanced absorption (CEA) (Engeln et al. 1998), and integrated cavity output spectroscopy (ICOS) (O'Keefe et al. 1999). Another way to increase the sensitivity of diode laser absorption measurements is by wavelength-modulation strategies, in which a signal corresponding to a derivative of the spectrum is recovered via a lock-in amplifier (Reid and Labrie 1981). Finally, balanced ratiometric detection, a technique involving the selection of two photodiodes with the same response characteristics, and the use of electronic noise suppression, also leads to substantial reduction in detection limits (Hobbs 1997). It should be noted, however, that none of these signal enhancing methods can overcome the fundamental shortcoming of absorption spectroscopy that is presented by its lack of spatial resolution.

Absorption spectroscopy is a simple technique in which a laser is chosen with a wavelength corresponding to a spectroscopic transition in one of the molecular species present. Some photons in the beam are absorbed by the molecules, exciting them to a higher energy state. The detected intensity at a given frequency, $I(\nu)$, is described by an exponential function due to molecular or atomic absorption as formulated in the Beer-Lambert Law:

$$\frac{I(\nu)}{I_0} = e^{-\sigma(\nu)NL} \tag{1.10}$$

Where I_0 is the intensity of the incident beam ($Wm^{-2}Hz^{-1}$), $\sigma(\nu)$ is the absorption-cross section (cm^2), N is the number density of the gas (cm^{-3}) and L is the path length (cm).

One important situation in which diode laser absorption sensors have been used extensively is in flame and engine diagnostics. Accurate measurements of species concentration in combustors and in exhaust streams are required for comparison with numerical simulation in the continual effort to increase efficiency and reduce emission of harmful pollutants. Such sensors were originally developed for use on laboratory systems, but diode laser absorption sensors are now being used for on-line sensing on the industrial scale. They are capable of much faster response times than traditional instruments that involve extractive sampling. Therefore, deviations from normal operating conditions are detected immediately and can be fed into a control response, thus maintaining optimum productivity. Nevertheless, these constitute line-of-sight measurements, so are typically restricted to use in exhaust streams and in one-dimensional flames.

A diode laser sensor system was developed (Mihalcea et al. 1998) to measure concentrations of NO, N_2O, CO, CO_2 and O_2 in a one-dimensional flame stabilised on a laboratory burner. The use of near infra-red TDLAS to make in situ measurements of species concentrations inside a 20-metre-long coal furnace has subsequently been demonstrated (Teichert et al. 2003). There are significant complications in this environment such as coal dust causing severe particulate scattering, beam steering due to temperature driven refractive-index fluctuations, and strong background radiation. A laser was scanned over two H_2O absorption peaks and the intensity ratio allowed a temperature to be inferred. The restrictions of this method of temperature measurement are discussed in the next section.

The method of seeding trace atoms into a combustion process as a probe species, as is described in the present work, has been done in a different

context (Schlosser et al. 2002). The authors used diode laser absorption spectroscopy to measure concentrations of alkali atoms, generated by thermal decomposition of various seeded alkali metal salt solutions (including LiCl, KCl and RbCl) in a rotary kiln. This led to a determination of the residence time distribution of flue gas, which is an important parameter in ensuring complete and clean combustion. The reason for the use of an atomic probe species was that the high oscillator strength of atoms leads to strong signals.

Combustion processes are not the only situation in which the measurement of gas concentrations has been performed using TDLAS. Applications of the technique in various environments are summarised in a review (Martin 2002) and some examples include process control, and atmospheric monitoring. Measurements of the CH_4 concentration were made *in-situ* in a chemical vapour deposition (CVD) reactor for coating glass with tin oxide and it was shown that the methane concentration is correlated to the film deposition rate (Holdsworth et al. 2001). In another application, tunable diode laser spectroscopy was used to build a hand-held methane sensor for the detection of gas leaks (van Well et al. 2005). In this case the detector was incorporated into the hand-held device and laser absorption was detected in the weak back-scattered light.

Many molecules have strong absorption lines in the mid-infrared (MIR) spectral region between 3-25 μm, corresponding to fundamental rotational and vibrational transitions. Lead-salt diode lasers emit in this spectral region but have the disadvantage of requiring cryogenic operating conditions typically maintained using liquid nitrogen. These have found application in biomedical diagnostics, such as in breath analysis. One example of this facilitates the detection of exhaled NO at ppb levels as a method of

diagnosing asthma (Roller et al. 2002). Similar technology has been used in searching for oil wells in the desert of Abu Dhabi by the detection of trace quantities of ethane in the atmosphere (Hirst et al. 2004). The more recent quantum cascade lasers (Faist et al. 1994) also emit in the MIR spectral region and are increasingly being used in absorption spectroscopy (Duxbury et al. 2005).

1.3.3 Temperature Measurement using TDLAS

Diode laser absorption spectroscopy can be used for temperature measurements only in the situation where the temperature is fairly homogeneous along the beam path. Clearly, this is not typically the case in flames so this technique has significant limitations. Such diode-laser absorption thermometry has been applied (Ma et al. 2002) in a very particular type of combustion system known as a pulse detonation engine (PDE) in which a quasi-one dimensional flame front propagates very rapidly down a narrow cylinder during detonation. There are thus no significant temperature gradients normal to the cylinder axis. A DFB laser was wavelength scanned to probe the Q-branch spectrum of ethylene at around 1.62 μm, and the temperature was found from the relative intensity of two absorption lines.

An attempt was made (Sanders et al. 2001) to address the situation of flows with non-uniform properties. This research exploits the possibility to scan VCSELs over a wide wavelength range to tune over sixteen separate transitions in molecular oxygen at around 760nm. Each of these transitions has a different temperature-dependence and it was possible to infer temperature distributions in the range 200K – 700K with a 30 ms time response. The authors note that other temperature ranges could be probed by

selecting different sets of transitions. They consider the absorption path to be composed of n uniform temperature segments and show by a mathematical derivation that these n temperatures can be found by probing the line-strength of n+1 absorption transitions. In addition to its poor level of accuracy, this technique suffers from the difficulty that although a temperature probability distribution is found, there is no information on actual temperatures at a specific location in the beam path. A spatial temperature profile can only be inferred from prior knowledge of the situation being probed.

Temperature measurements based on absorption, therefore, have some inherent disadvantages, which will be demonstrated here by showing the results of some simple calculations. The graphs shown below give a comparison of the actual mean temperature and the temperature that would be measured by line-of-sight absorption. These take account of two separate effects that bias the measurement: 1. the density is higher in cold regions so the average will be weighted towards colder temperatures; 2. the relative population of the two levels is a non-linear function of temperature, according to Eqn. 1.7, so the average ratio does not correspond to the average temperature. Atomic indium has been chosen as the probe species for this simulation, but it is emphasised that this problem exists regardless of the probe species.

Figure 1.5 shows the result of a line-of-sight temperature measurement in a situation in which the beam path contains two regions of equal length in which the mole fraction of seeded indium is homogeneous. One of the regions is at a constant temperature of 2000 K, and the measured temperature is calculated for a range of temperatures in the second region. In Figure 1.5,

the measured temperature is plotted together with the true mean of the temperatures of the two regions.

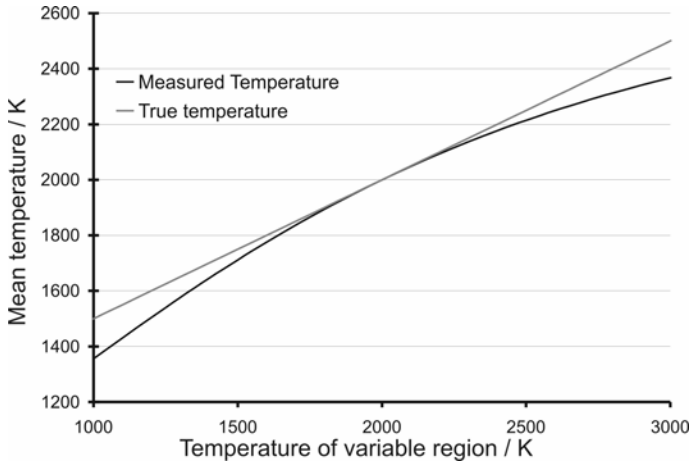

Figure 1.5. Simulation of temperature measured by absorption spectroscopy in the case of two regions of equal length and different temperature. One region is at 2000 K. The true average and measured temperature plotted against the temperature of the second region.

It is clear that the temperature is underestimated by greater amounts as the difference in temperature between the two regions increases; in this case, this is principally due to the effect of changing density with temperature. When the variable temperature region is at a temperature of 1000 K, the mean temperature along the entire beam path is 1500 K, whereas the measured temperature is 1355 K. This corresponds to an error of nearly 10 %.

A second simulation was done in which it was assumed that there is a Gaussian probability density function (PDF) in temperature, as may be the case in some engines. It should be noted, though, that the path-averaged technique gives no information about whether the PDF actually is Gaussian or not, so it is not possible to test the validity of such an assumption in a practical situation. The mean temperature was specified as 2000 K and the

measured temperature was calculated for a range of standard deviations. The plot in Figure 1.6 shows that as the standard deviation is increased, a systematic underestimate of temperature is again apparent due to the biasing of the measurement toward colder regions.

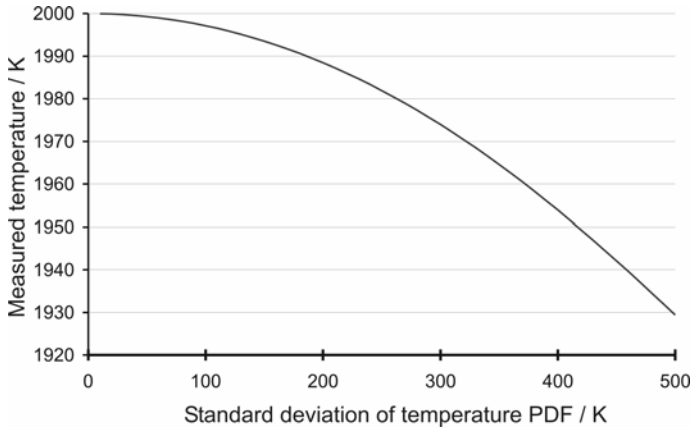

Figure 1.6. The measured temperature in a system where the temperature follows a Gaussian PDF centred around a mean of 2000 K.

It has therefore been shown that diode laser absorption spectroscopy leads to measured temperatures that do not represent the true average in the system, even when a probe species is selected so that the relative population of the two levels being probed is roughly linearly proportional to temperature in the range of interest. One further influence on absorption measurements is that the effects of flame chemistry mean that the mole fraction of the probe species would probably be quite different in regions of unequal temperature. This is certainly the case in flames, where there are large spatial variations in composition, as shown in Figure 1.1. This effect is difficult to quantify but could lead to substantial unaccountable errors in the measured temperature of inhomogeneous systems. In the case of turbulent flames, this effect would mean that the use of a reactant or product of combustion as the probe species

would certainly lead to a quite incorrect measurement, and it may be of little value to measure the mean temperature of a turbulent flame in any case. No previously existing diode laser technique allows the measurement of temperatures at a point in the flame, and it is the purpose of the present research to develop such a system.

1.3.4 Blue Diode Laser Spectroscopy

The fabrication of blue diode lasers was not possible until the late 1990's because of the difficulties in growing the required semi-conductor material GaN without imperfections (Nakamura 1998). Near infra-red diode lasers are grown from traditional well-characterised semi-conductor materials such as AlGaAs. Blue diode lasers were developed for use in DVD players, the shorter wavelength corresponding to a smaller diffraction-limited spot size and thus allowing higher density data storage (Narahara et al. 2000). Since they became commercially available in 1999 from Nichia Corporation, however, blue diode lasers, which are currently available in the spectral region 370-480 nm, have also been used for a number of spectroscopic applications both in atomic and molecular spectroscopy, and in biological experiments.

Of particular relevance to the present research, a blue extended-cavity diode laser emitting at 410 nm was used to study fluorescence of indium in an atomic beam (Leinen et al. 2000). Atoms in the $5^2P_{1/2}$ state were excited to the $6^2S_{1/2}$ state and fluorescence was detected in the $6^2S_{1/2} \rightarrow 5^2P_{3/2}$ transition through an interference filter centred at 450 nm. As a result of the narrow linewidth and the scanning capability of the ECDL, the authors could observe the hyperfine structure of the $5^2P_{1/2} \rightarrow 6^2S_{1/2}$ indium transition. Since the

experiments were done on an atomic beam, the spectrum consisted of four sharp peaks and no pressure or Doppler broadening was apparent. This allowed the authors to study one of the hyperfine peaks with high resolution and to distinguish the contributions by the two isotopes ^{115}In and ^{113}In (relative abundances 95.7% and 4.3% respectively), which cause the peak to have an asymmetric doublet structure.

Blue diode lasers have subsequently been used (Scheibner et al. 2002) to measure both the concentration and temperature of sputtered aluminium atoms in a hollow cathode discharge. Temperature is found from the absorption line-width by assuming that Doppler broadening is dominant, due to the low pressure atmosphere. Both the $S_{1/2} \rightarrow P_{1/2}$ and $S_{1/2} \rightarrow P_{3/2}$ absorption transitions at 394.4 nm and 396.15 nm respectively were probed. Other examples of use of blue diode lasers in atomic spectroscopy include the study of gallium atoms in hollow cathode discharge (Marago et al. 2003), and of potassium atoms in a low pressure heated vapour cell (Gustafsson et al. 2000).

Some molecular absorption experiments have also been performed using blue diode lasers. NO_2 has a broad absorption band between 350 nm and 500 nm and is an important species in combustion and atmospheric chemistry. Measurements of NO_2 concentration were made using a diode laser emitting at around 390nm and a detection limit of 0.7 ppmv was achieved (Liu et al. 2002). This very high sensitivity could be achieved because of the strong electronic transitions in the UV-visible spectral region. Even greater sensitivity NO_2 measurements have been made using cavity ring-down spectroscopy, which allowed a detection limit of 0.4 ppbv to be obtained (Mazurenka et al. 2003).

Other applications of blue diode lasers have been in the field of biological and biochemical applications. They have been used, for example as an excitation source for confocal microscopy imaging of living mammalian cells stained with fluorophores (Girkin and Ferguson 2000). Blue diode lasers have also been used in the detection of tagged amino acids by capillary electrophoresis LIF (Melanson and Lucy 2000). Another analytical tool in which blue diode lasers have been incorporated is fluorescence lifetime microscopy (Ryder et al. 2002) in which the decay-time of fluorophores provides information about their molecular environment. The techniques described in this thesis are therefore of relevance not only to indium spectroscopy and flame temperature measurement but have relevance to a much wider range of diagnostic applications.

1.4 References

Aldén, M. and S. Walin (1985). "CARS Experiments in a Full Scale (10m x 10m) Industrial Coal Furnace." Applied Optics **24**: 3434-3437.

Atakan, B., J. Heinze and U. E. Meier (1997). "OH laser-induced fluorescence at high pressures: Spectroscopic and two-dimensional measurements exciting the A-X (1,0) transition." Applied Physics B-Lasers and Optics **64**: 585-591.

Barlow, R. S., J. H. Frank, A. N. Karpetis and J.-Y. Chen (2005). "Piloted methane/air jet flames: Transport effects and aspects of scalar structure." Combustion and Flame **143**: 433-449.

Batchelor, G. K. (1959). "Small-scale variation of convected quantities like temperature in a turbulent fluid. Part 1. General discussion and the case of small conductivity." Journal of Fluid Mechanics **5**: 113-133.

Bessler, W. G. and C. Schulz (2004). "Quantitative multi-line NO-LIF temperature imaging." Applied Physics B-Lasers and Optics **78**: 519-533.

Cattolica, R. (1981). "OH Rotational Temperature from 2-Line Laser-Excited Fluorescence." Applied Optics **20**: 1156-1166.

Dec, J. E. and J. O. Keller (1986). "High-Speed Thermometry Using Two-Line Atomic Fluorescence." Proceedings of the Combustion Institute **21**: 1737-1745.

Duxbury, G., N. Langford, M. T. McCulloch and S. Wright (2005). "Quantum cascade semiconductor infrared and far-infrared lasers: from trace gas sensing to non-linear optics." Chemical Society Reviews **34**: 921-934.

Eckbreth, A. C. (1980). "CARS Thermometry in Practical Combustors." Combustion and Flame **39**: 133-137.

Eckbreth, A. C. (1996). Laser Diagnostics for Combustion Temperature and Species. Amsterdam, Gordon and Breach.

Eckbreth, A. C. and R. J. Hall (1979). "CARS Thermometry in a Sooting Flame." Combustion and Flame **36**: 87-98.

Engeln, R., G. Berden, R. Peeters and G. Meijer (1998). "Cavity enhanced absorption and cavity enhanced magnetic rotation spectroscopy." Review of Scientific Instruments **69**: 3763-3769.

Engström, J., J. Nygren, M. Aldén and C. F. Kaminski (2000). "Two-line atomic fluorescence as a temperature probe for highly sooting flames." Optics Letters **25**: 1469-1471.

Faist, J., F. Capasso, D. L. Sivco, C. Sirtori, A. L. Hutchinson and A. Y. Cho (1994). "Quantum Cascade Laser." Science **264**: 553-556.

Gasnot, L., P. Desgroux, J. F. Pauwels and L. R. Sochet (1999). "Detailed analysis of low-pressure premixed flames of CH_4 + O_2 + N_2: A study of prompt-NO." Combustion and Flame **117**: 291-306.

Geyer, D., A. Kempf, A. Dreizler and J. Janicka (2005). "Scalar dissipation rates in isothermal and reactive turbulent opposed-jets: 1-D-Raman/Rayleigh experiments supported by LES." Proceedings of the Combustion Institute **30**: 681-689.

Girkin, J. M. and A. I. Ferguson (2000). "Confocal microscopy using an InGaN violet laser diode at 406nm." Optics Express **7**: 336-341.

Gustafsson, U., J. Alnis and S. Svanberg (2000). "Atomic spectroscopy with violet laser diodes." American Journal of Physics **68**: 660-664.

Hayhurst, A. N. and D. B. Kittelson (1977). "Heat and Mass-Transfer Considerations in Use of Electrically Heated Thermocouples of Iridium Versus an Iridium-Rhodium Alloy in Atmospheric-Pressure Flames." Combustion and Flame **28**: 301-317.

Herriott, D. R., H. Kogelnik and R. Kompfner (1964). "Off-axis paths in spherical mirror resonators." Applied Optics **3**: 523-526.

Hirst, B., G. Gibson, S. Gillespie, I. Archibald, O. Podlaha, K. D. Skeldon, J. Courtial, S. Monk and M. Padgett (2004). "Oil and gas prospecting by ultra-sensitive optical gas detection with inverse gas dispersion modelling." Geophysical Research Letters **31**.

Hobbs, P. C. D. (1997). "Ultrasensitive laser measurements without tears." Applied Optics **36**: 903-920.

Holdsworth, R. J., P. A. Martin, D. Raisbeck, H. Rivero, H. E. Sanders, D. Sheel and M. E. Pemble (2001). "Time-resolved in-situ spectroscopic monitoring of the CVD of tin oxide onto a glass substrate." Chemical Vapor Deposition **7**: 39-43.

Kaminski, C. F., J. Engström and M. Aldén (1998). "Quasi-Instantaneous Two-Dimensional Temperature Measurements in a Spark Ignition Engine Using Two-Line Atomic Fluorescence." Proceedings of the Combustion Institute **27**: 85-93.

Kee, R. J., J. F. Grcar, M. D. Smooke and J. A. Miller (1985). A FORTRAN program for modelling steady laminar one-dimensional premixed flames, Sandia National Laboratories.

Kee, R. J., F. M. Rupley and J. A. Miller (1989). CHEMKIN-II: A Fortran Chemical Kinetics Package for the Analysis of Gas-Phase Chemical Kinetics, Sandia National Laboratories.

Kohse-Höinghaus, K., R. S. Barlow, M. Aldén and J. Wolfrum (2005). "Combustion at the focus: laser diagnostics and control." Proceedings of the Combustion Institute **30**: 89-123.

Lee, M. P., B. K. McMillin and R. K. Hanson (1993). "Temperature-Measurements in Gases by Use of Planar Laser-Induced Fluorescence Imaging of NO." Applied Optics **32**: 5379-5396.

Leinen, H., D. Glassner, H. Metcalf, R. Wynands, D. Haubrich and D. Meschede (2000). "GaN blue diode lasers: a spectroscopist's view." Applied Physics B-Lasers and Optics **70**: 567-571.

Liu, J. T. C., R. K. Hanson and J. B. Jeffries (2002). "High-sensitivity absorption diagnostic for NO_2 using a blue diode laser." Journal of Quantitative Spectroscopy & Radiative Transfer **72**: 655-664.

Ma, L., S. T. Sanders, J. B. Jeffries and R. K. Hanson (2002). "Monitoring and control of a pulse detonation engine using a diode-laser fuel concentration and temperature sensor." Proceedings Of The Combustion Institute **29**: 161-166.

Marago, O. M., B. Fazio, P. G. Gucciardi and E. Arimondo (2003). "Atomic gallium laser spectroscopy with violet/blue diode lasers." Applied Physics B-Lasers and Optics **77**: 809-815.

Martin, P. A. (2002). "Near-infrared diode laser spectroscopy in chemical process and environmental air monitoring." Chemical Society Reviews **31**: 201-210.

Mazurenka, M. I., B. L. Fawcett, J. M. F. Elks, D. E. Shallcross and A. J. Orr-Ewing (2003). "410-nm diode laser cavity ring-down spectroscopy for trace detection of NO_2." Chemical Physics Letters **367**: 1-9.

Melanson, J. E. and C. A. Lucy (2000). "Violet (405 nm) diode laser for laser induced fluorescence detection in capillary electrophoresis." Analyst **125**: 1049-1052.

Mihalcea, R. M., D. S. Baer and R. K. Hanson (1998). "A diode-laser absorption sensor system for combustion emission measurements." Measurement Science & Technology **9**: 327-338.

Moya, F. S., A. J. Duret and J. P. E. Taran (1975). "Gas Spectroscopy and Temperature Measurements by Coherent Raman Anti-Stokes Scattering " Optics Communications **13**: 169-174.

Nakamura, S. (1998). "The roles of structural imperfections in InGaN-Based blue light-emitting diodes and laser diodes." Science **281**: 956-961.

Narahara, T., S. Kobayashi, M. Hattori, Y. Shimpuku, G. J. van den Enden, J. Kahlman, M. van Dijk and R. van Woudenberg (2000). "Optical disc system for digital video recording." Japanese Journal of Applied Physics Part 1-Regular Papers Short Notes & Review Papers **39**: 912-919.

NIST (2006). NIST Atomic Spectra Database. http://physics.nist.gov/cgi-bin/AtData/lines_form

O'Keefe, A., J. J. Scherer and J. B. Paul (1999). "cw Integrated cavity output spectroscopy." Chemical Physics Letters **307**: 343-349.

Reid, J. and D. Labrie (1981). "2nd-Harmonic Detection with Tunable Diode-Lasers - Comparison of Experiment and Theory." Applied Physics B-Photophysics and Laser Chemistry **26**: 203-210.

Ricci, L., M. Weidemueller, T. Esslinger and A. Hemmerich (1995). "A compact grating-stabilized diode laser system for atomic physics." Optics Communications **117**: 541.

Richter, H., S. Granata, W. H. Green and J. B. Howard (2005). "Detailed modeling of PAH and soot formation in a laminar premixed benzene/oxygen/argon low-pressure flame." Proceedings of the Combustion Institute **30**: 1397-1405.

Roller, C., K. Namjou, J. D. Jeffers, M. Camp, A. Mock, P. J. McCann and J. Grego (2002). "Nitric oxide breath testing by tunable-diode laser absorption spectroscopy: application in monitoring respiratory inflammation." Applied Optics **41**: 6018-6029.

Romanini, D., A. A. Kachanov and F. Stoeckel (1997). "Diode laser cavity ring down spectroscopy." Chemical Physics Letters **270**: 538-545.

Ryder, A. G., T. J. Glynn, M. Przyjalgowski and B. Szczupak (2002). "A compact violet diode laser-based fluorescence lifetime microscope." Journal of Fluorescence **12**: 177-180.

Sanders, S. T., J. Wang, J. B. Jeffries and R. K. Hanson (2001). "Diode-laser absorption sensor for line-of-sight gas temperature distributions." Applied Optics **40**: 4404-4415.

Sands, D. (2004). Diode Lasers. Bristol, Institute of Physics Publishing.

Scheibner, H., S. Franke, S. Solyman, J. F. Behnke, C. Wilke and A. Dinklage (2002). "Laser absorption spectroscopy with a blue diode laser in an aluminum hollow cathode discharge." Review of Scientific Instruments **73**: 378-382.

Schlosser, E., J. Wolfrum, L. Hildebrandt, H. Seifert, B. Oser and V. Ebert (2002). "Diode laser based in situ detection of alkali atoms: development of a new method

for determination of residence-time distribution in combustion plants." Applied Physics B-Lasers And Optics **75**: 237-247.

Seitzman, J. M., R. K. Hanson, P. A. Debarber and C. F. Hess (1994). "Application of Quantitative 2-Line OH Planar Laser-Induced Fluorescence for Temporally Resolved Planar Thermometry in Reacting Flows." Applied Optics **33**: 4000-4012.

Seufert, J., M. Fischer, M. Legge, J. Koeth, R. Werner, M. Kamp and A. Forchel (2004). "DFB laser diodes in the wavelength range from 760 nm to 2.5 μm." Spectrochimica Acta Part a-Molecular and Biomolecular Spectroscopy **60**: 3243-3247.

Stenhouse, I. A., D. R. Williams, J. B. Cole and M. D. Swords (1979). "CARS measurements in an internal combustion engine." Applied Optics **18**: 3819-3825.

Teichert, H., T. Fernholz and V. Ebert (2003). "Simultaneous in situ measurement of CO, H_2O, and gas temperatures in a full-sized coal-fired power plant by near-infrared diode lasers." Applied Optics **42**: 2043-2051.

van Well, B., S. Murray, J. Hodgkinson, R. Pride, R. Strzoda, G. Gibson and M. Padgett (2005). "An open-path, hand-held laser system for the detection of methane gas." Journal of Optics a-Pure and Applied Optics **7**: S420-S424.

Wang, G.-H., N. T. Clemens and P. L. Varghese (2005). "Two-point, high-repetition-rate Rayleigh thermometry in flames: techniques to correct for apparent dissipation induced by noise." Applied Optics **44**: 6741-6751.

Warnatz, J., U. Maas and R. W. Dibble (1996). Combustion: physical and chemical fundamentals, modelling and simulation, experiments, pollutant formation. Berlin, Springer-Verlag.

Westbrook, C. K., Y. Mizobuchi, T. J. Poinsot, P. J. Smith and J. Warnatz (2005). "Computational combustion." Proceedings of the Combustion Institute **30**: 125-157.

Chapter 2

Blue extended-cavity diode lasers with improved wavelength scanning properties

This Chapter describes the development of novel laser devices emitting continuously tunable radiation suitable for high-resolution spectroscopy. They incorporate commercially available diode lasers, emitting in the blue/violet spectra region, and other standard components. The practice of using optical feedback to stabilise the output of Fabry-Perot diode lasers is not new and the 'extended-cavity' configuration has often been implemented in the past (Wieman and Hollberg 1991; MacAdam et al. 1992; Ricci et al. 1995). Nevertheless, by combining the qualities of previously reported extended-cavity designs, a novel concept has emerged leading to development of blue extended-cavity diode lasers systems whose mode-hop free tuning ranges substantially exceed those of commercially available ready-built laser systems.

We have seen in Chapter 1 that diode lasers are widely used in high-resolution spectroscopy and gas sensing, and that they have attractive properties such as being compact, cheap, and robust. The emission of diode lasers is usually

multi-mode, but, for high-resolution spectroscopy, single-mode continuously tunable radiation is needed. This can be obtained by the use of wavelength-selective feedback from an external component such as a grating. The development of a blue diode laser system with superior wavelength tuning properties (Hult et al. 2005b) was an important part of the present research and was essential to performing the high-resolution spectroscopy (Burns et al. 2004) and atomic-fluorescence temperature measurements (Hult et al. 2005a) described in later chapters.

The novel tuning scheme involves the use of a grating mount with multiple piezo-electric actuators, allowing the grating angle and cavity length to be adjusted independently. Whereas some ECDL designs involve the use of anti-reflection coating on the front facet of the diode, this costly procedure has been avoided here by simultaneous tuning of the diode laser injection current. The combination of these two techniques leads to the construction of a versatile, inexpensive, and easily optimised diode laser, which was the subject of a patent application. This innovative tuning scheme has been demonstrated for two GaN diode lasers with wavelengths of around 451 nm and 410 nm respectively, which were chosen to coincide with electronic transitions of atomic indium. Continuous tuning ranges of 110 GHz and 93 GHz have been achieved with the 451 nm laser and the 410 nm laser respectively.

This Chapter begins with an outline of the technique of using optical feedback to stabilise the emission of diode lasers. A detailed description is then given of the extended cavity diode laser design, and the required electrical tuning signals to achieve optimal mode-hop free tuning ranges are addressed. Finally, the results of experiments to characterise the spectral emission and tuning properties of the laser are presented.

2.1 Extended-cavity diode lasers

2.1.1 Laser Principles

In Chapter 1, we saw that diode lasers operate based on the emission of light by recombination of electrons and holes. This light is then amplified by the process of stimulated emission. This section gives an overview of the theory behind the gain profile and cavity mode structure of lasers.

The range of frequencies over which any laser can achieve gain is related to the line-profile of the amplifying transition in the active medium. As mentioned in Chapter 1, the Beer-Lambert relation describes the absorption of light by a sample which is at equilibrium:

$$\frac{I(\nu)}{I_0(\nu)} = \exp\left[-\sigma(\nu)NL\right] \tag{2.1}$$

Here, N is the number density of absorbing molecules, L is the absorption path length, and $\sigma(\nu)$ is the absorption cross-section. In a laser, however, where the population of the upper state (N_k) of the transition is high, the expression for the change in intensity of light during one round-trip in the optical cavity must also include a term for stimulated emission (Demtröder 2003):

$$G(\nu) = \frac{I(\nu)}{I_0(\nu)} = \exp\left[-2\alpha(\nu)L\right] \tag{2.2}$$

Here, $G(\nu)$ is the gain factor, $I_0(\nu)$ is the intensity of the incident beam, $I(\nu)$ is

the intensity of the transmitted beam, L is the length of the active medium, and the absorption coefficient ($\alpha(\nu)$) is defined as:

$$\alpha(\nu) = \sigma(\nu)\left(N_i - \frac{g_i}{g_k} N_k \right) \tag{2.3}$$

Here, N_i and N_k are the population densities in states i and k, g_i and g_k are the degeneracies of states i and k, and $\sigma(\nu)$ is the absorption cross section for the transition $E_i \rightarrow E_k$. In the case of a population inversion (i.e. $N_k > (g_k/g_i)N_i$), it can be seen that the $G(\nu)>1$ so the incident wave is amplified rather than attenuated. In a laser cavity other round trip losses exist that are unrelated to the active medium. These are described by the fractional loss coefficient ($\gamma(\nu)$), and include transmission losses through the cavity mirrors, The intensity after one round trip in the optical cavity is therefore described by the 'gain factor':

$$G(\nu) = \frac{I(\nu)}{I_0(\nu)} = \exp\left[-2\alpha(\nu)L - \gamma(\nu) \right] \tag{2.4}$$

The mirror transmission losses are strongly dependent on frequency due to the eigenfrequency spectrum of the cavity resonator, which is related to the Airy function (Demtröder 2003). Neglecting absorption losses, this is expressed as:

$$\frac{I_T(\nu)}{I_0(\nu)} = \frac{(1-R)^2}{(1-R)^2 + 4R\sin^2(\phi(\nu)/2)} \tag{2.5}$$

Here, $I_0(\nu)$ is the incident intensity, $I_T(\nu)$ is the transmitted intensity, R is the reflectivity of the cavity mirrors, and $\phi(\nu)$ is the phase difference between a wave incident on the first mirror and a wave that has travelled to the other mirror and back, which (neglecting phase changes due to reflection) is given by:

$$\phi = \frac{2\pi\nu}{\delta\nu} \tag{2.6}$$

Here, ν is the laser frequency, and $\delta\nu$ is the frequency spacing between the cavity modes, or 'free-spectral-range' (FSR). If the dispersion of the cavity material is neglected, then the FSR is given by:

$$\delta\nu = \frac{c}{2nd} \tag{2.7}$$

Here, n is the refractive index of the cavity material, and d is the cavity length. It can be seen from Eqn. 2.5 that there will be constructive interference if ν is equal to an integer multiple of the free-spectral-range ($\delta\nu$), so that ϕ is equal to an integer multiple of 2π and thus $I_T(\nu) = I_0(\nu)$. In practice, the maximum transmission is less than the incident intensity due to absorption of light by the mirrors. This description of interference fringes in a resonant optical cavity also applies to the Fabry-Perot etalon, a device whose

use is in characterising diode laser tuning properties and spectral purity is described later in this chapter.

The interplay between these laser cavity modes and the laser gain profile is illustrated schematically in Figure 2.1.

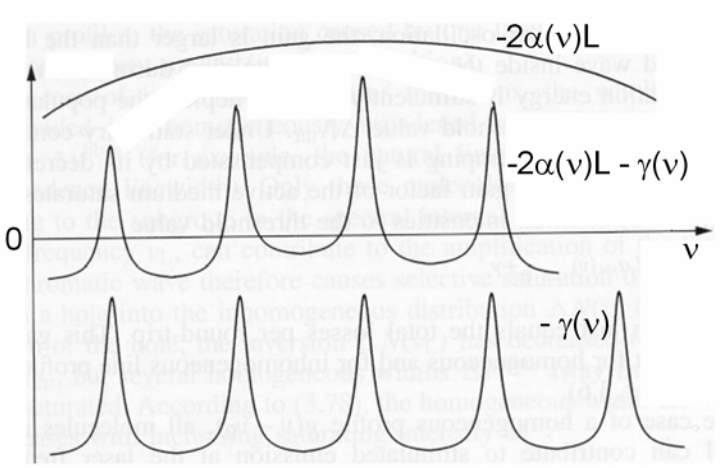

Figure 2.1. Transmission losses of a resonant cavity ($\gamma(\nu)$), the gain curve of the active medium ($-2L\alpha(\nu)$), and the net gain $\Delta\alpha(\nu)=-2L\alpha(\nu)-\gamma(\nu)$. The threshold for laser action is exceeded when $\Delta\alpha(\nu) > 0$. Each curve represents a term that is dimensionless. Adapted from Demtröder (Demtröder 2003)

Laser amplification will take place only at frequencies for which the net gain $-2L\alpha(\nu)-\gamma(\nu)$ is greater than zero. If the pump power (i.e. in the case of a diode laser the injection current) is increased gradually from zero, the population in the upper state of the transition (N_k) rises. When the pump power exceeds a certain threshold value, the net gain for frequencies corresponding to the peaks of the cavity modes exceeds zero, and laser action begins. The stimulated emission builds up until it is sufficient to deplete the population of the upper state (N_k) to a value whereby the net gain is $\Delta\alpha(\nu) = 0$, and the gain factor is $G(\nu) = 1$, thus reaching steady-state.

The linewidth of the laser is another important characteristic. The full-width at half maximum height (FWHM) of the transmission peaks of a passive optical cavity, in which the only losses result from transmission through the mirrors, is defined by:

$$\Delta\nu = \delta\nu \frac{1-R}{\pi\sqrt{R}} \tag{2.8}$$

In the case of a laser, however, the linewidth is typically narrower than the value given by Eqn. 2.8, due to the influence of the laser gain, and is equal to (Demtröder 2003):

$$\Delta\nu = \delta\nu \frac{1-G(\nu)}{\pi\sqrt{G(\nu)}} \tag{2.9}$$

In principle, this means that, for a gain factor of $G(\nu)$ =1, the linewidth would be expected to approach zero. This does not occur in reality due to a fundamental limitation imposed by phase fluctuations (Demtröder 2003). In reality, fluctuations in the effective cavity length (nd) due to noise mean that the laser line-width is normally much greater than this theoretical minimum.

The above discussion has been concerned with the behaviour of lasers in general but the same principles apply to diode lasers. Blue diode lasers can be classified as Fabry-Perot lasers, meaning that the laser cavity is formed by the end facets of the diode crystal, which act as mirrors. The output from Fabry-Perot diode lasers consists of several longitudinal modes, as shown in Figure

2.1. The spacing between longitudinal modes ($\delta\nu$) is governed by the following equation (Demtröder 2003):

$$\delta\nu = \frac{c}{2nd\left(1+\left(\nu/n\right)dn/d\nu\right)} \tag{2.10}$$

Here, n is the refractive index of the cavity material, d is the cavity length, ν is the laser frequency, and c is the speed of light in a vacuum. Note a more complicated expression is given here because the dispersion ($dn/d\nu$), a term that can normally be neglected, is unusually high for GaN (Tisch et al. 2001).

2.1.2 Littrow configuration ECDL

In high-resolution spectroscopy applications it is usually essential to have single-mode narrow line-width diode laser emission (Wieman and Hollberg 1991) that can be smoothly wavelength-tuned without discrete jumps in wavelength (known as mode-hops), or in laser intensity. The maximum mode-hop free tuning range that can be achieved is, therefore, a key parameter in diode laser spectroscopy.

Inherently single-mode devices such as distributed-feedback (DFB) lasers and vertical-cavity surface-emitting lasers (VCSEL) were mentioned in Chapter 1 where it was also noted that the availability of such devices is restricted to certain parts of the near infra-red spectral region. By contrast, Fabry-Perot diode lasers are available at a wide range of wavelengths and may be used to construct a narrow line-width, tunable single-mode laser source through optical feedback techniques (Wieman and Hollberg 1991). Figure 2.2 shows a simple implementation of this idea, which is known as the Littrow

configuration extended (or external) cavity diode laser (ECDL). Although the Littrow scheme is most widely used, other extended-cavity geometries, such as the Littman-Metcalf configuration (Littman and Metcalf 1978) have also been implemented (Harvey and Myatt 1991).

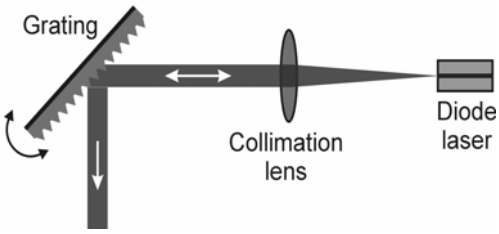

Figure 2.2 Littrow-configuration ECDL

The Littrow configuration ECDL involves the use of optical feedback from a grating positioned at an angle so that the minus-one diffraction order is retro-reflected into the diode (MacAdam et al. 1992; Ricci et al. 1995). The grating angle determines the feedback wavelength, and thus also the output wavelength of the ECDL, according to the grating equation:

$$d(\sin\theta_m - \sin\theta_i) = m\lambda \tag{2.11}$$

Here, d is the grating groove spacing, m is the diffraction order, λ is the laser wavelength, θ_i is the incident angle and θ_m is the angle of the m order diffraction fringe. For the retro-reflected beam, the condition $\theta_i = -\theta_m$ is fulfilled and $m = -1$, so Eqn. 2.11 can be simplified to:

$$2d\sin\theta = \lambda \tag{2.12}$$

The zero order diffraction from the grating forms the output beam. In addition to the internal Fabry-Perot cavity formed by the facets of the diode, there is also an extended cavity formed between the grating and the back facet of the diode.

This leads to the existence of extended-cavity modes in addition to the Fabry-Perot diode modes. These modes are represented schematically in Fig. 2.3 along with the grating feedback profile and the diode gain curve. The spectral profile of the grating feedback is narrower than the diode gain curve and its width (FWHM) can be approximated by considering the resolution of the grating (Boggs et al. 1998):

$$\Delta \nu_g = \frac{dc}{D\lambda} \cos\theta_i \qquad (2.13)$$

Here, D is the width of the diode laser beam. As an example, let us consider the blue ECDLs used during this project, whose approximate characteristics are summarised in Table 2.1.

	ECDL 1	**ECDL 2**
Wavelength λ	451 nm	410 nm
Beam diameter *D*	5 mm	5 mm
Grating angle θ_i	24.0º	21.7º
Grating lines per mm	1800	1800
Grating period *d*	556 nm	556 nm
Grating feedback width $\Delta\nu_g$	70 GHz	80 GHz
Extended cavity length	24 mm	25 mm
Extended cavity mode spacing	6 GHz	6 GHz
Diode cavity length (assumed)	0.7 mm	0.7 mm
GaN refractive index *n*	2.52	2.56
GaN dispersion dn/dv	9.8×10^{-16} Hz $^{-1}$	12.0×10^{-16} Hz $^{-1}$
Diode mode spacing (predicted)	45 pm	35 pm

Table 2.1. General characteristics of the extended-cavity diode lasers constructed during this research.

The width of the grating feedback profile was calculated from Eqn. 2.13. In estimating the extended-cavity mode spacing from Eqn. 2.7, it was assumed that the refractive index of air is n_{air}=1. It should be noted that the diode cavity length shown here is an assumed value from literature and has not been measured. The diode mode spacing was estimated from Eqn. 2.10, based on an assumed chip length of 0.7 mm (Nakamura et al. 1997), and using the values for the refractive index and dispersion of GaN from plots in the literature (Tisch et al. 2001).

The emission wavelength of the ECDL corresponds to the position at which a longitudinal mode of the extended cavity matches a Fabry-Perot diode laser mode that lies close to the peak of the grating wavelength feedback profile (Yan and Schawlow 1992).

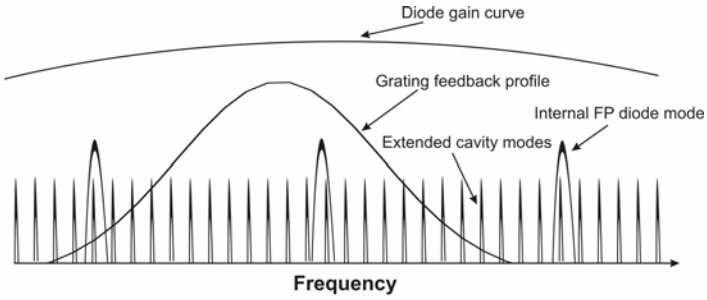

Figure 2.3 Schematic representation of mode competition in an ECDL.

A standard Fabry-Perot diode laser in Littrow configuration can be coarsely tuned over its gain bandwidth through rotation of the grating. However, such coarse tuning involves discrete jumps, which occur when the number of standing wave nodes in the laser cavity changes abruptly. To avoid this, the length of the extended cavity must be simultaneously adjusted (Favre et al. 1986). With reference to Figure 2.3, rotation of the grating causes the grating feedback curve to move to one side. An expression for the shift in the central wavelength of the grating feedback profile is obtained by differentiation of Eqn 2.12. For small changes in grating angle:

$$\Delta\lambda = 2d\cos\theta\ \Delta\theta \qquad (2.14)$$

Similarly, scanning the cavity length causes the comb of extended-cavity modes to shift in wavelength. The magnitude of this change can be

determined by considering the number of standing waves in the extended cavity:

$$N = \frac{\nu}{\delta\nu} = \frac{2nl_C}{\lambda} \tag{2.15}$$

Here, l_C is the extended-cavity length. By differentiation, we obtain (for small cavity length changes):

$$\Delta\lambda = \frac{\lambda}{l_C}\Delta l_C \tag{2.16}$$

The grating rotation and cavity length change must be performed in the correct proportion so that mode-hops are avoided.

The most common way of achieving the optimum ratio between grating angle and cavity length is to mount the grating on a lever arm in contact with a single piezoelectric crystal and to rotate it around a pivot-point (de Labachelerie and Passedat 1993; Trutna and Stokes 1993). Considerable effort has been spent on the theoretical prediction of where the optimal pivot-point should lie; see for example (Nilse et al. 1999). An alternative is to use a multiple-piezo actuator optical mount to achieve the same relation between grating rotation and translation during tuning (Mellis et al. 1988; Laurila et al. 2005). A key advantage of this approach is that the requirement for accurate mechanical positioning of the pivot point is replaced by a simple balancing of the electrical signals driving the piezo-actuators. Furthermore, this strategy avoids the need to construct a precision pivot-point grating mount: a standard

kinematic mount may be used instead. Since the extended-cavity length and the grating angle may be adjusted independently in the multiple-piezo scheme, it is also possible to optimise the initial overlap between the active extended-cavity mode and the grating feedback centre-wavelength at the beginning of the wavelength scan. Such an optimisation would be more difficult to achieve with the conventional pivot-arm design.

The issue of mode-competition from the internal Fabry-Perot cavity has commonly been addressed by applying a high-quality anti-reflection coating to the front facet (Boshier et al. 1991). By removing the reflectivity of the front facet, the internal cavity should, in theory, be eliminated, leaving only a single cavity formed between the grating and the back diode facet. In practice, however, it is still necessary to match the lengths of the extended cavity and the Fabry-Perot cavity in order to achieve a large tuning range, even with antireflection coated diodes (Hildebrandt et al. 2003). This appears to suggest that the residual reflectance is generally not low enough to suppress entirely the Fabry-Perot mode structure of the diode. Another disadvantage of the anti-reflection coating approach is that such treatment of the diode is a complex and expensive process, which risks damaging the device. As a result of this there is limited commercial availability of anti-reflection coated laser diodes.

It has been reported, however, that the need for anti-reflection coating can be avoided by modulating the laser diode injection current (Ricci et al. 1995). This causes temperature variations in the active region of the diode, which lead in turn to changes in both the length and refractive index of the diode cavity. It should be noted that the temperature change also causes a shift in the central wavelength of the diode gain curve (at a higher rate); since the gain curve is very broad, however, this effect is not normally of significance.

The shift in the wavelength of the diode mode is given by (Demtröder 2003):

$$\Delta\lambda = \frac{\partial\lambda}{\partial n}\frac{dn}{dT}\Delta T + \frac{\partial\lambda}{\partial l_d}\frac{dl_d}{dT}\Delta T = \lambda\left(\frac{1}{n}\frac{dn}{dT} + \frac{1}{L}\frac{dL}{dT}\right) \qquad (2.17)$$

The idea of the concept is to tune the laser diode injection current in synchronisation with the extended-cavity tuning, thus matching the wavelength shifts of the cavity modes. This then allows wide mode-hop free tuning ranges to be achieved using standard uncoated laser diodes, therefore resulting in low-cost ECDL systems.

2.2 Construction and testing of blue ECDLs

This section concerns the successful development and application of a new method, which combines the advantages of multiple-actuator tuning of a reflection-grating and synchronised injection current modulation, to achieve mode-hop free tuning of a Littrow-configuration ECDL. Standard GaN laser diodes without anti-reflection coating were used together with commercially available opto-mechanical mounts, and laser-control electronics to create a simple and cost-effective ECDL system. Two such ECDL systems were constructed, operating at wavelengths of around 410 nm and around 451 nm respectively. A number of ECDL systems operating in the violet spectral region, 390-420 nm, have previously been reported, achieving tuning ranges of 6-50 GHz (Conroy et al. 2000; Leinen et al. 2000; Hildebrandt et al. 2003). The two systems described here, however, have each achieved mode-hop free tuning ranges in excess of 90 GHz, which as far as the author is aware, represent the widest tuning ranges ever achieved for ECDL systems operating

in the blue or violet spectral region. This then opens up a wide variety of possible applications including the high-resolution spectroscopy and flame thermometry described in later chapters.

A detailed description of the novel ECDL design is given here, and various experiments to characterise the laser performance are outlined. A geometrical model is also presented, which describes how the piezo-actuator voltages and the diode-laser injection current must be varied relative to one another in order to obtain the correct proportion between the scanning of grating angle, of the extended cavity length, and of the diode Fabry-Perot cavity length, and thus to optimise the mode-hop free tuning range.

2.2.1 Experimental set-up

Two extended-cavity diode lasers (ECDL) systems were constructed during this research. The diode laser used in the first ECDL system was a multi-mode Fabry-Perot GaN device (Nichia) operating at around 451 nm, with a maximum output power of approximately 5 mW. The laser used in the second ECDL was also a Fabry-Perot GaN device (Nichia). At room temperature it operated at around 410 nm, with a maximum output power of around 30 mW. The reflectivities of the unmodified front facets of these commercial devices were not disclosed by the supplier. For devices similar to the 410 nm laser, a reflectivity of around 4% has been estimated (Hildebrandt 2004).

A schematic illustration of the design of the extended cavity is shown in Figure 2.4. The diode laser was housed in a thermo-electrically temperature-controlled mount (Thorlabs). An anti-reflection coated aspheric lens (focal length=4.5 mm, numerical aperture=0.55) was used to collimate the output

beam. A mount with a shallow screw-thread (Thorlabs, S1TM09) was used to finely adjust the distance of the collimating lens from the diode laser. A holographic grating (1800 lines-per-mm; Edmund Scientific) was mounted in a piezo-electric kinematic mount (Thorlabs, KC1-PZ), which was attached directly to the laser diode mount by three steel rods. The mount incorporated three piezo-electric actuators, thus allowing the grating angle and extended cavity length to be tuned independently. The grating was mounted at the angle calculated from Eqn. 2.12 and listed in Table 2.1. The zeroth order served as the laser output beam and was reflected by a small mirror mounted on the same plate as the grating, as shown in Figure 2.4. This ensured that the direction of the output beam remained constant even for large changes in the grating angle associated with coarse wavelength tuning (Hawthorn et al. 2001). The same thing could be achieved through the use of a transmission grating (Merimaa et al. 2000), but the transmission grating required is not a standard commercially-available component and has to be manufactured specially, thus complicating the set-up.

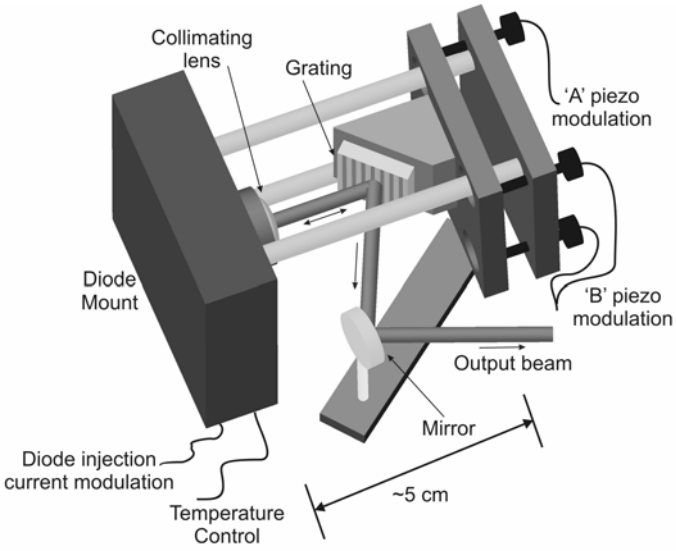

Figure 2.4 The extended cavity diode laser configuration

Fine adjustment to the grating alignment was performed to optimise feedback to the diode, following a method described in detail in the literature (MacAdam et al. 1992). This was done using a piece of white card with a small aperture. The card was held inside the extended cavity so that the diode laser beam passed through the aperture. The beam retro-reflected from the grating was then incident on the card, but the grating could be aligned (coarse adjustment with thumb-screws) so that this beam passed back through the aperture. This rough alignment was then improved upon by reducing the diode injection current to just above threshold and then very carefully adjusting the grating angle so that the intensity of the beam coupled out of the extended cavity was maximised. The better alignment of the cavity caused a reduction in the laser threshold current, so the injection current was again reduced to just above the new threshold value, and the fine optimisation of the grating angle was done again. This process was repeated several times until

no further reduction in the threshold current could be obtained. Naturally, the vertical angle adjustment was more critical, since there is a small range of horizontal grating angles at which the laser can operate.

The temperature and injection-current of the diode laser were controlled using low-noise drivers (Tektronix). A three-channel high-voltage supply (Thorlabs) was used to control the lengths of the three piezo-electric actuators in the kinematic mount. Wavelength scanning was achieved by tuning the piezo-actuators with two triangular waveforms, which were in phase and whose amplitudes could be accurately adjusted. One of these waveforms was used to modulate the piezo marked 'A' in Fig. 2.4, and the other was applied to both of the two piezos marked 'B', thus allowing simultaneous rotation and translation of the grating. No anti-reflection coating was applied to the front facet of the diode. Instead the effective length of the internal Fabry-Perot diode cavity was tuned synchronously by ramping the diode injection current with a third triangular waveform. The triangular waveform modulation signals were generated by use of a circuit containing three variable resistors, which divided the output signal from a single function generator. The variable resistors permitted an empirical optimisation of the ratios between the amplitudes of the tuning signals.

A glass plate was used to direct a part of the output beam towards a solid quartz Fabry-Perot etalon with a low finesse and a free spectral range of 3.1 GHz. The transmitted intensity pattern allowed the relative frequency change of the ECDL output during scans to be measured. In addition to this, the main part of the laser beam was directed into a scanning confocal Fabry-Perot etalon (FSR=7.5 GHz, F=30), which was used to monitor the spectral output of the ECDL to determine whether single-mode operation was maintained

during the scans. The power of the ECDL output beam was also continuously measured, by directing a reflection from a second glass plate onto a photo-diode.

A measurement of the laser line-width was made by tuning the wavelength so that the transmitted intensity through the confocal etalon was about 50% of the maximum, corresponding to the location of the steepest gradient on an interference fringe. As a result, any change in laser frequency would result in a change in the intensity of transmitted light, which was monitored with a photo-diode. The gradient of the slope, for a particular value of transmitted intensity, could be determined from a single mode scan, which was performed immediately prior to the line-width measurement.

In a separate experiment, a characterisation of the spectral output of the free-running Fabry-Perot diode lasers was performed using a 1.26-metre-long spectrometer with a 2400 lines-per-mm grating operating in first order, fitted with a back illuminated un-intensified CCD camera (Wright Instruments, 384 x 576 pixels) for signal detection. In each case, the responses of the diode to tuning of the injection current and of temperature were investigated.

2.2.2 Model to predict required tuning signals

A geometrical analysis can be made in order to estimate the required ratio between the extensions of the piezo-actuators in order to optimise the relative shifts of grating angle and extended cavity length, and thus to maximise the single-mode tuning range of the device. This derivation is based on determining the relative piezo-actuator extensions required to match the shift of the grating feedback profile with the shift of the extended-cavity modes according to Eqns. 2.14 and 2.16. The details of this derivation are presented

in Appendix A, in order to preserve the continuity of the main text. It should be noted though that the analysis of the optimum tuning signals was, nevertheless, an important part of the work of this project. This results in the following relationship:

$$\frac{\Delta A}{\Delta B} = 1 + \frac{l_1}{l_C \sqrt{\frac{4d^2}{\lambda^2} - 1} - l_2} \tag{2.18}$$

Here, ΔA and ΔB are the extensions of the respective piezo-actuators, d is the grating groove spacing, and λ is the laser wavelength. The relevant dimensions of the ECDL system are shown in Figure 2.5.

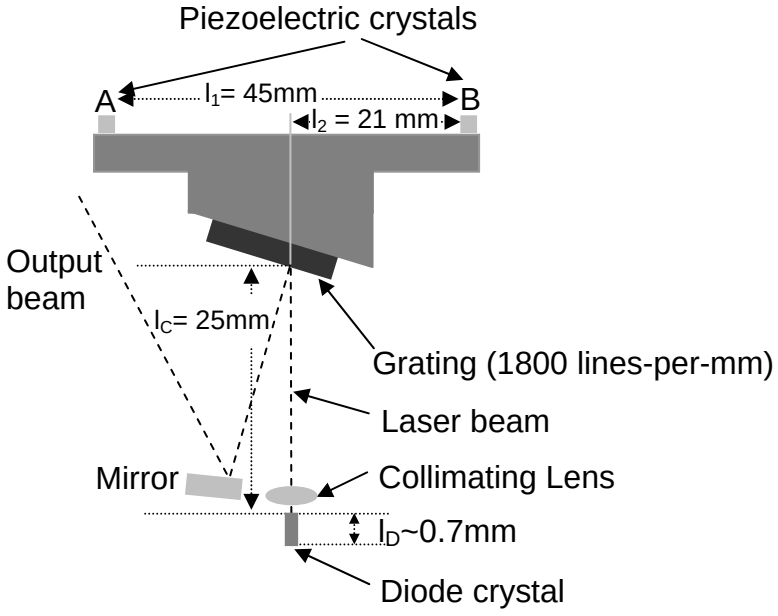

Figure 2.5 Littrow configuration extended cavity diode laser

Neglecting effects of non-linearity and hysteresis, the expansion of each piezo-actuator is assumed to be directly proportional to the voltage applied to the piezo-crystal ($\Delta A=\alpha\Delta V_A$; $\Delta B=\alpha\Delta V_B$). The same constant of proportionality (α) applies in the case of each of the three piezo-actuators. Therefore, the ratio between the voltages applied to the piezo-actuators, $\Delta V_A/\Delta V_B$, is identical to Eqn. 2.18. This means that in order to achieve a linear wavelength scan, two linear voltage ramps should be applied: the first to piezo-actuator '*A*', and the second to piezo-actuators '*B*', the ratio between the slopes of the two ramps being defined by Eqn. 2.18.

It has already been highlighted that the length of the diode laser Fabry-Perot cavity l_D must also be tuned in synchronisation with the translation and rotation of grating in order to preserve the number of longitudinal modes within this internal cavity. The length of the diode cavity l_D is adjusted by tuning the diode laser current I, which has the effect of modifying the local temperature of the diode junction. As an approximation, it will be assumed that there is a linear relationship between the effective diode chip length and the injection current. A parameter β expressing the change in wavelength with the diode laser injection current can be defined as $\Delta\lambda = \beta\Delta I$. This allows us to develop a simple equation relating the required modulation signal for tuning of the diode laser injection-current to the piezo-actuator modulation. The details of this derivation are also given in Appendix A. The resulting relationship can be used to determine the current tuning required to match the tuning of the Fabry-Perot diode to the extended cavity length change. It is applicable for *any* ratio between the modulation signals of piezo-actuators '*A*'

and '*B*', and not just the one specified by Eqn. 2.18. The ratio between the current modulation, ΔI, and piezo modulation, ΔV_B, is the following:

$$\frac{\Delta I}{\Delta V_B} = \frac{\alpha\lambda}{\beta l_C}\left(\frac{l_2}{l_1}\left(1 - \frac{\Delta V_A}{\Delta V_B}\right) - 1\right) \tag{2.19}$$

Mode-hop free wavelength scanning can therefore be achieved by tuning the diode-laser injection current using a triangular waveform synchronised to the piezo-actuator modulation signals. The ratio of the slope of the current ramp to that of the voltage ramp driving piezo-actuator '*B*' is given by Eqn. 2.19. This ratio turns out to be negative, for the experimental set-up described above, since the extension of the piezo-actuators pushes the grating towards the diode, thus shortening the extended cavity, whereas increasing the injection current causes the diode cavity to become longer. Therefore, the slope of the diode current modulation signal should have opposite sign to the piezo voltage slopes; a voltage inverter circuit was used to achieve this.

2.3 Results of blue diode laser characterisation

The results concerning the spectral properties of the free-running Fabry-Perot diode lasers are presented briefly, before giving a detailed account of the determination of the mode-hop free scanning ranges and line-widths of the two ECDLs that were built.

2.3.1 Spectral characterisation of free-running Fabry-Perot diode lasers

It is particularly interesting to consider the spectral emission of the free-running 451 nm Fabry-Perot diode laser since devices operating at this wavelength have only recently become available, and no report of their performance had previously been published in the literature. Figure 2.6 shows the spectral output from the 451 nm Fabry-Perot diode laser operating without extended-cavity feedback at different diode injection currents ranging from below threshold (45 mA) up to operating current (58 mA). The width of the individual laser modes in the plot is determined by the spectrometer resolution and does not represent the actual line-width of the laser. The spectrum shown in plot a) corresponds to an injection current of 45 mA, which was just below the threshold current at a diode operating temperature of 40° C. Below threshold, the device acts as a light emitting diode (LED) and a large number of longitudinal modes are observed in the spectral profile, with a mode spacing of around 58 pm. This is in fair agreement with the mode spacing of 45 pm (Table 2.1) that was calculated for an assumed diode chip length of 0.70 mm (Nakamura et al. 1997). At the threshold current of 46 mA (plot b) two dominant modes are observed, with a number of weaker side modes present. As the injection current is further increased (plots c-f) the positions of the strongest modes shift to higher wavelengths. Single mode lasing is observed only for certain specific combinations of current and temperature as shown, for example, in plot c). The observed multi-mode behaviour is one of the reasons why it is desirable to use the Fabry-Perot laser in an extended cavity configuration for high resolution spectroscopy

applications. Another advantage is that the range of coarse wavelength tuning, for a specific diode, can be extended by a few nm beyond what is possible by tuning temperature and current only. The mode spacing observed above threshold current in the present laser matches the regular Fabry-Perot spacing observed below threshold. This is in contrast to previous observations for some violet diode lasers operating in the 400-420 nm region, where mode spacings several times greater than those estimated from the Fabry-Perot cavity length were observed (Nakamura et al. 1997; Jiang and Lin 1999).

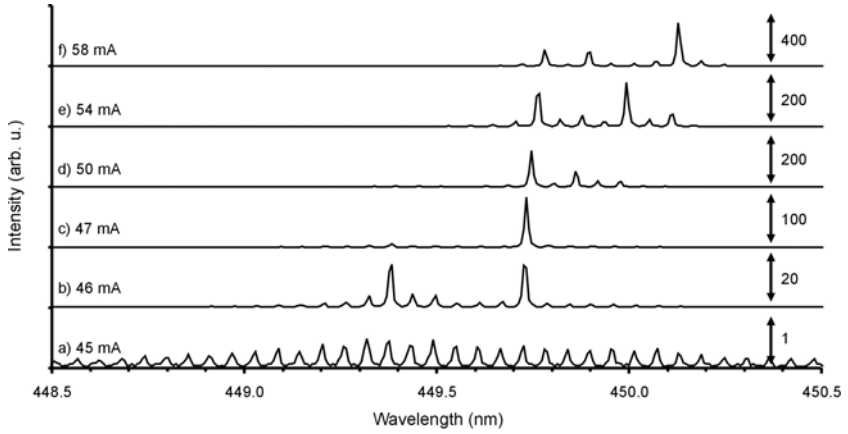

Figure 2.6 Spectral output from a Fabry-Perot diode laser, emitting at around 451 nm, as a function of diode injection current: a) corresponds to a current just below the laser threshold; b) is just above threshold current; plots c) to f) correspond to a range of injection currents from a little above threshold up to operating current. The relative intensity scale of each spectrum is indicated to the right.

A comparison of the spectral emission of the 410 nm diode laser, before mounting in the extended cavity, with that of the 451 nm diode laser is also worthwhile. In Figure 2.7, the spectral output of the free-running Fabry-Perot diode lasers is shown as a function of temperature and of injection current. The parameters (β) required for the evaluation of current tuning rates were extracted from the current-tuning plots.

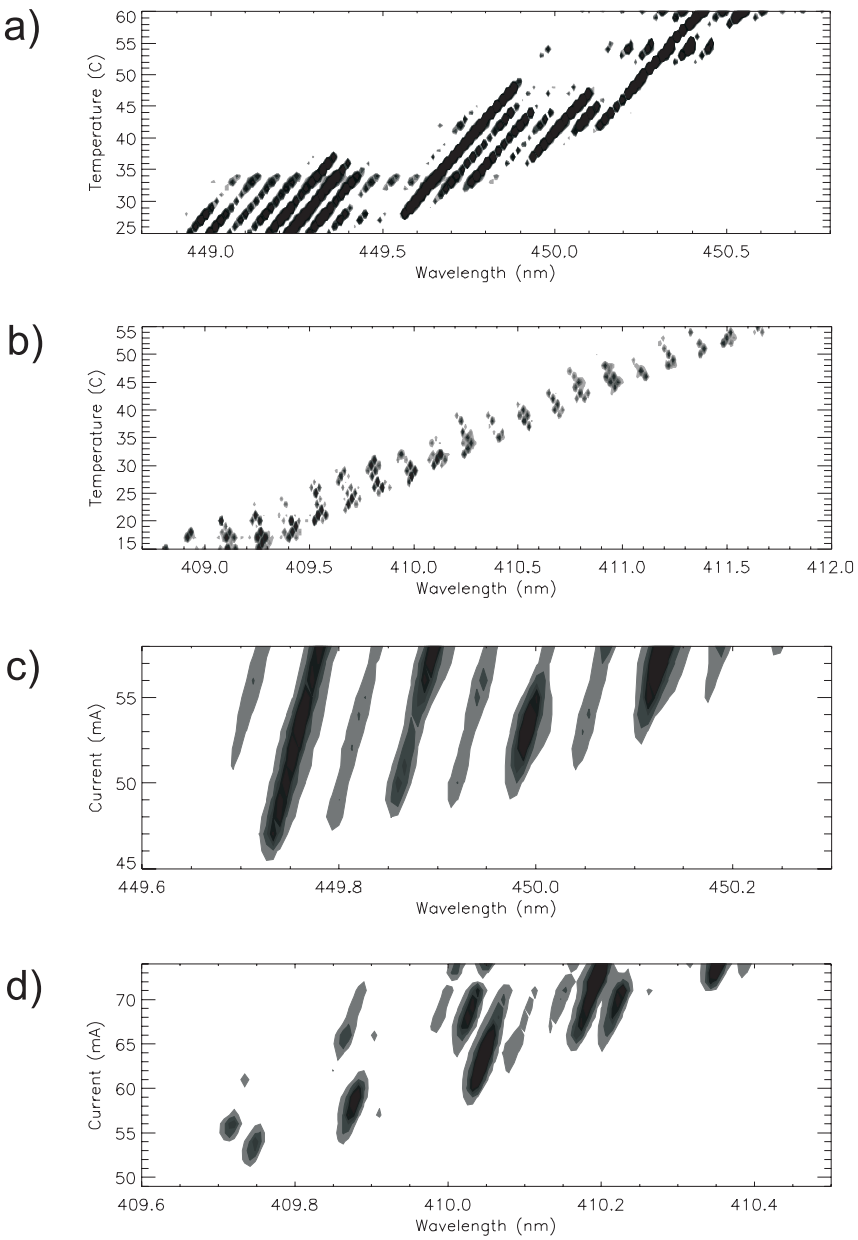

Figure 2.7 Spectral emission of the Fabry-Perot diode lasers as a function of a) temperature for the 451 nm laser, b) temperature for the 410 nm laser, c) current for the 451 nm laser, d) current for the 410 nm laser.

In the grey-scale plots shown in Figure 2.7, regions of darker shading correspond to higher intensities. Figure 2.7a) shows the spectral emission of the free-running 451 nm Fabry-Perot diode laser for diode temperatures ranging from 25 to 60 °C (the injection current was held constant during this experiment). From this plot it is apparent that, at most temperatures, between five and fifteen Fabry-Perot diode modes are active, whereas single mode emission is only achieved within a very narrow range of operating conditions. The individual modes appear to tune continuously with temperature over intervals of 10-20 °C. From the slope of the individual modes, a wavelength tuning rate of 16 pm/°C can be estimated. A shift of the gain curve to higher wavelengths with increasing temperatures is also apparent (around 40 pm/°C) since the overall mode pattern is shifting to the right.

In Figure 2.7b) the corresponding plot for the 410 nm Fabry-Perot laser is shown. There are several distinct differences compared to the behaviour of the 451 nm diode. For most temperatures there are only a few modes active, often separated by a multiple of the expected mode spacing. For a particular temperature there are normally between two and four groups of active modes, each consisting of one or two neighbouring modes. These groups are separated by gaps spanning two or three inactive modes. Individual modes tune to higher wavelengths with increasing temperature at a rate of around 15 pm/°C. Most modes tune for about 3 °C after first appearing, they then disappear and become inactive for about 3 °C before reappearing again and tuning for another 3 °C. The gaps in the centre of each mode tuning, thus lead to the spacing between the groups of modes observed in Figure 2.7b). From the overall slope of the mode pattern seen in this figure, the rate at which the gain curve changes with temperature was estimated to be around 60 pm/°C

which is thus higher than the tuning rate of the individual modes, as it was in the case of the 451 nm laser.

The effect of current tuning on the spectral output of the Fabry-Perot diode lasers is shown in Figure 2.7c) and d). With increasing injection current a larger number of modes become active and the positions of the individual modes also shift to higher wavelengths. As has been addressed above, the reason for this is that at higher injection currents, the local temperature of the diode junction is slightly elevated. The parameter for the rate of wavelength tuning with injection current can therefore be evaluated from the plots: β=4.3 pm/mA for the 451 nm laser; β=4.0 pm/mA for the 410 nm laser.

The spectral output of the free-running 410 nm diode laser at just below threshold current is similar to the one shown for the 451 nm diode laser in Figure 2.6a). In this case, the free-spectral-range is 38 pm, which is in good agreement with the value of 34 pm (Table 2.1), which was calculated for an assumed diode cavity length of 0.70 mm (Nakamura et al. 1997).

2.3.2 Wavelength scanning of blue extended cavity diode lasers

The results concerning the 451 nm ECDL will be discussed first and in greater detail, before subsequently addressing the 410 nm ECDL as a comparison. Figure 2.8a) shows a Fabry-Perot interferometer fringe pattern corresponding to a 110 GHz wide scan of the 451 nm ECDL. The scan was performed by simultaneous modulation of piezo-actuators *A* and *B*, and of the diode injection current *I*, as described previously. The scan was recorded in 250 ms, with the laser operating at 25° C. Two different Fabry-Perot interferometers (FSR=3.1 GHz and 7.5 GHz) were used to monitor the laser frequency during

the scan. The Fabry-Perot etalon transmission traces have been normalised by the simultaneously recorded laser output power, which is also shown.

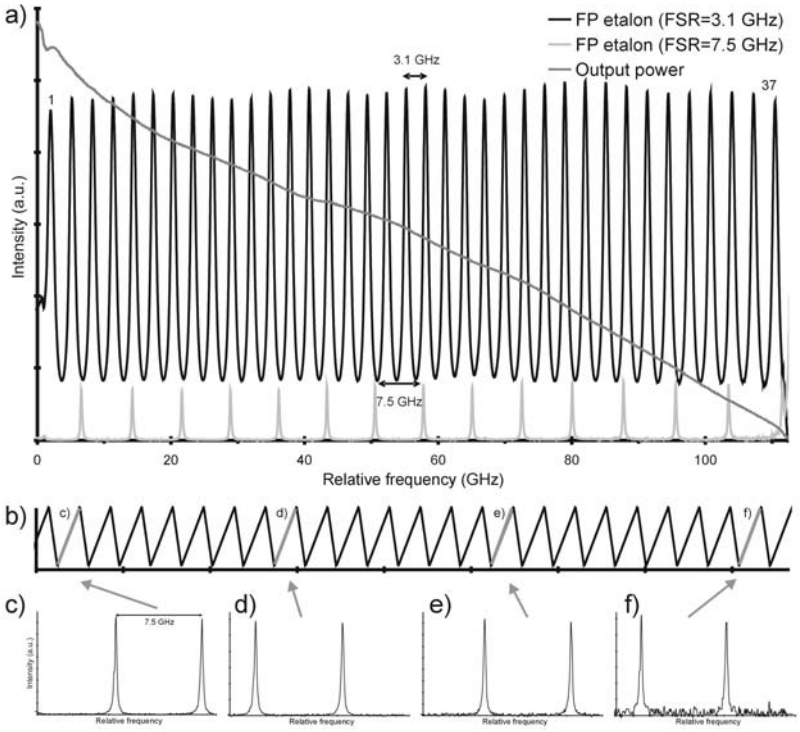

Figure 2.8 a) Transmitted fringe patterns through two different Fabry-Perot interferometers (FSR=3.1 GHz and 7.5 GHz) during a wavelength scan of the 451 nm ECDL. For the lower FSR etalon, 37 interference fringes are observed, corresponding to 110 GHz mode-hop free tuning. The laser output power is also shown. b) Mirror spacing of scanning Fabry-Perot interferometer (FSR=7.5 GHz) used to validate single-mode emission during ECDL scanning. c)-f) Scanning Fabry-Perot traces recorded at four different times during a single laser wavelength scan, the corresponding times are indicated in fig b).

During the scan shown in Figure 2.8a) the 7.5 GHz confocal etalon was used with a fixed mirror separation. A separate experiment was performed to check that the laser emission remained single-mode throughout the entire ECDL scan. The laser wavelength tuning was performed as before, at a rate of 4 Hz, but now the mirror spacing of the high-finesse confocal etalon was

modulated at a rate of 100 Hz, as shown in Figure 2.8b). The amplitude of the mirror displacement was adjusted to ensure that the same laser mode appeared at least twice during each scan. Four of the resulting Fabry-Perot etalon scans are shown in Figure 2.8c)-f), and in each of Figures 2.8c)-f), two narrow peaks of similar intensity are visible; the spacing of these two peaks is the same in each case. This therefore confirms that the laser was emitting on a single longitudinal mode at each of the positions of the laser wavelength scan. Although the results of only four of the twenty-five confocal etalon scans are shown as a representative sample, the others all show the same features and thus confirm the absence of side-modes from the ECDL emission over the entire 110 GHz wavelength scan.

It is worthwhile to compare this mode-hop free tuning range to those previously achieved for blue/violet diode lasers. Extended-cavity designs employing anti-reflection coated GaN diodes, pivot-point grating tuning, and injection-current tuning have achieved a continuous tuning range of around 50 GHz (Hildebrandt et al. 2003). Similar diodes without anti-reflection coating, used in combination with optimised pivot-point grating mounting and injection-current modulation have achieved continuous tuning ranges of 10-25 GHz (Leinen et al. 2000). Finally, uncoated diodes in combination with un-optimised pivot point grating mounting have typically achieved continuous tuning ranges below 10 GHz (Conroy et al. 2000; Gustafsson et al. 2000).

The output power of the laser is also shown in Fig. 2.8a), it decreases steadily during the 110 GHz long scan shown here, almost reaching zero at one end of the scan. Such a reduction in laser output-power during scanning is an inherent feature of the current tuning process and restricts the scanning range in all ECDL devices that rely on this principle. At one end of the injection-

current scan, the maximum recommended current is reached, whereas at the other end of the scan, the current falls below the threshold value required for laser action. In the present case the injection current was modulated around a mean value of 51.9 mA, resulting in an output power from the ECDL of around 0.9 mW at the centre of the scan. It is evident that the fractional decrease in laser power would be less significant for shorter wavelength scans.

For the 451 nm ECDL the extended-cavity and diode parameters (defined above, and shown in Figure 2.5) are summarised in Table 2.2.

l_1	45.0 mm
l_2	22.5 mm
l_C	24.0 mm
α	41 nm/V
β	4.25 pm/mA

Table 2.2. Important dimensions and tuning parameters for the 451 nm ECDL.

This leads to the following predicted ratios between the modulation voltages for optimised tuning (Eqns. 2.18 and 2.19): $\Delta V_A/\Delta V_B$=2.43, and $\Delta I/\Delta V_B$=-0.23. It was found that a wide range of ratios between ΔV_A and ΔV_B resulted in broad mode-hop free tuning ranges. The actual ratios used for the 110 GHz mode-hop free scan shown in Fig. 2.8 were: $\Delta V_A/\Delta V_B$=1.56 and $\Delta I/\Delta V_B$ = -0.27 mA/V. Mode-hop free tuning ranges exceeding 80 GHz were observed for $\Delta V_A/\Delta V_B$ ranging from 1.0 to 2.5. This indicates that tuning of the grating angle is of less importance in the present experiment; precise matching of the extended-cavity length tuning with the diode cavity length tuning is more critical. This appears to suggest that the overlap between the

active diode mode and the active extended cavity mode is of greater importance than the exact matching of the peak of the grating feedback profile to the cavity modes. A possible explanation for this may be that the front-facet reflectivity of the present diode laser is appreciable, and the spectral profile of the grating feedback is relatively wide compared to the extended-cavity mode spacing. It should be noted that the grating feedback profile is still sufficiently narrow though, to favour only one of the diode Fabry-Perot modes. It should be noted that more care would have to be taken to synchronise the grating tuning with the extended cavity length and current tuning when using either anti-reflection coated diodes or gratings providing a narrower feedback profile. This therefore represents a disadvantage of using anti-reflection coated diodes.

In contrast to the grating angle tuning, the exact matching of the diode current and extended-cavity length tuning was found to be critical to achieve even modest mode-hop free tuning ranges with the present ECDL. For the ratio $\Delta V_A/\Delta V_B$=1.56, used for the scan in Fig. 2.8a), Eqn. 2.19 predicts $\Delta I/\Delta V_B$ = -0.23, which is close to the experimentally observed ratio of -0.27. This close agreement was observed for a wide range of values of $\Delta V_A/\Delta V_B$. The scan shown in Fig. 2.8 was recorded at a laser scan rate of 4 Hz to allow a sufficient number of confocal Fabry-Perot etalon scans to be recorded during one wavelength sweep. The same tuning ranges, however, were achieved at laser scanning rates of up to 60 Hz, above which the maximum tuning range gradually decreases with increasing scanning frequency due to piezo-response non-linearities, to mechanical resonances, and to limited diode heat transfer.

2.3.3 Line-width measurement

As was described in Section 2.2.1, an upper estimate of the line-width of the extended cavity diode laser was determined by analysing the transmission through a Fabry-Perot etalon (FSR=7.5 GHz, F=30) when the laser was tuned to the slope of one of its transmission peaks. In this configuration, fluctuations in the laser frequency manifest themselves as fluctuations in the transmitted intensity. Figure 2.9a) shows the result of a laser scan over the etalon peak, which was recorded immediately prior to commencing the line-width measurement. The gradient of the etalon peak at a particular value of transmission (indicated in Figure 2.9a) can thus be used to convert the observed variations in transmission to variations in laser frequency, shown in Figure 2.9b). In Figure 2.9c) a histogram of instantaneous laser frequencies is shown; the width of the histogram provides an upper estimate of the laser line-width of 8 MHz, over a time period of 150 ms.

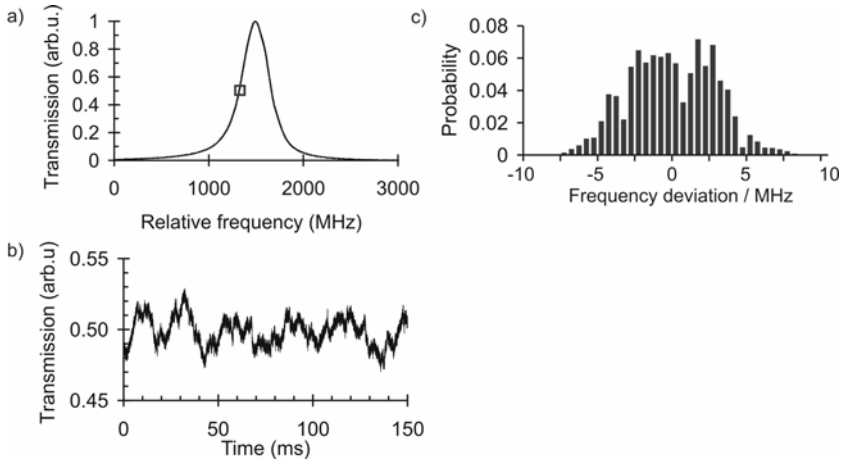

Figure 2.9 a) Fabry-Perot etalon transmission as a function of laser frequency; b) Variations in etalon transmission over time for a laser tuned to the location indicated by the grey box in a); c) Histogram of instantaneous laser frequencies corresponding to the transmission trace in b).

The technique relies on the assumption that the fundamental line-width (typically around 100 kHz for ECDLs (Wieman and Hollberg 1991)) of the source is negligible compared to the magnitude of rapid mechanically-induced frequency jitter. The measured line-width is the consequence of mechanical instabilities in the extended cavity and in the etalon used for analysis combined with fluctuations in laser intensity. Since the latter two effects are artefacts of the measurement, the actual line-width is likely to be lower than the value reported.

2.3.4 Comparison of results for 410 nm ECDL

A similar analysis was performed for a second GaN diode emitting at around 410 nm. In Fig. 2.10 an etalon transmission pattern is shown, corresponding to a mode-hop-free wavelength-scan of the 410 nm ECDL over a range of 93 GHz. The laser output power is also shown in Fig. 2.10: a reduction in intensity by around 45% was observed during this scan. The current was modulated around a mean value of 70 mA, resulting in an output power from the ECDL of around 2 mW. It was found that extensive mode-hop free tuning could be achieved with this laser for a wide range of ratios between ΔV_A and ΔV_B. For the scan shown in Fig. 2.10, the actual ratios were $\Delta V_A/\Delta V_B$=1.51 and $\Delta I/\Delta V_B$ = -0.21. This current to piezo-voltage modulation ratio therefore happens to match the value of -0.21 predicted using Eqn. 2.19, based on the 410 nm ECDL parameters listed in Table 2.3.

l_1	45.0 mm
l_2	20.5 mm
l_C	25.0 mm
α	41 nm/V
β	4.0 pm/mA

Table 2.3. Important dimensions and tuning parameters for the 410 nm ECDL.

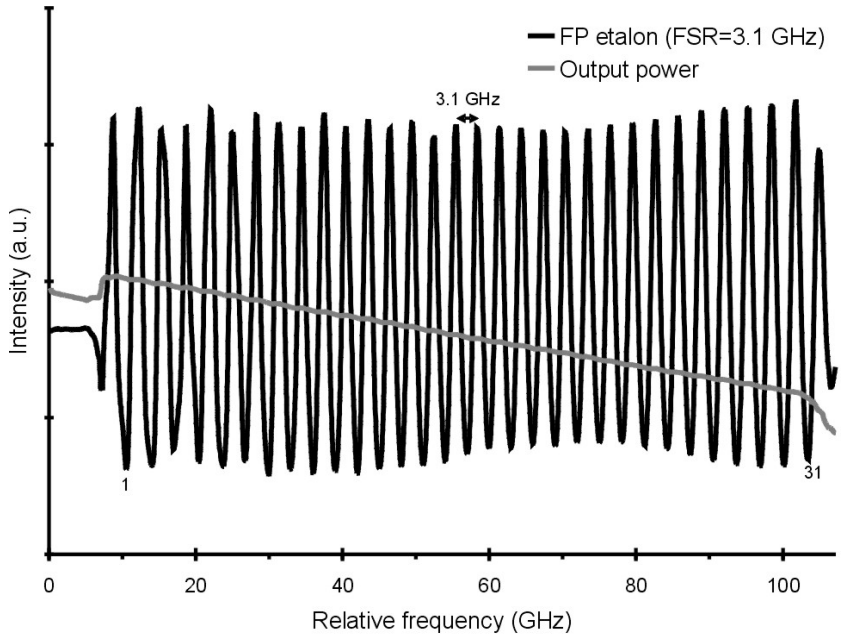

Fig. 2.10 Transmitted etalon fringe pattern recorded during a wavelength scan of the 410 nm extended-cavity diode laser. A low-finesse Fabry-Perot interferometer (FSR=3.1 GHz) was used. Thirty-one fringes can be distinguished, corresponding to a 93 GHz wide mode-hop free scan. The simultaneously recorded laser output power is also shown.

One of the advantages of the multiple piezo-actuator configuration, compared to the standard pivot-point configuration is the simplicity with which the extended-cavity length and the grating angle can be independently changed.

At the beginning of an experiment, while adjusting the modulation signal ratios to achieve a mode-hop free scan, the DC-offsets on the modulation signals for the piezo-actuators can be adjusted to optimise the overlap between the extended-cavity mode structure and the Fabry-Perot diode mode. Similarly, the diode temperature or injection-current, or the grating angle, can be used to optimise the initial overlap between the grating feedback profile and the Fabry-Perot diode mode (although in the present ECDL systems this optimisation was found to be less critical). Furthermore, small changes made to the relative slopes of the modulation signals could compensate for initial mis-matches between the extended-cavity modes, the diode cavity modes, and the grating feedback profile. The effects of small non-linearities or hysteresis of the actuators could also be compensated for by this procedure. It is believed that the combination of these effects is part of the explanation for the comparatively long tuning ranges achieved with the ECDL systems described here.

2.4 Conclusions

In this chapter, a novel design for extended-cavity diode lasers, based on the combination of multiple-piezo grating tuning and synchronous diode injection current modulation, has been presented. This design has allowed mode-hop free tuning ranges in excess of 90 GHz to be achieved with two ECDL systems operating at wavelengths of around 451 nm and 410 nm respectively. These tuning ranges are much greater than any that have been previously reported in the literature. The properties of these laser systems opens up a range of possible applications and their use in high-resolution spectroscopy and flame thermometry will be described in later chapters.

2.5 References

Boggs, B., C. Greiner, T. Wang, H. Lin and T. W. Mossberg (1998). "Simple high-coherence rapidly tunable external-cavity diode laser." Optics Letters **23**(24): 1906-1908.

Boshier, M. G., D. Berkeland, E. A. Hinds and V. Sandoghdar (1991). "External-Cavity Frequency-Stabilization of Visible and Infrared Semiconductor-Lasers for High-Resolution Spectroscopy." Optics Communications **85**(4): 355-359.

Burns, I. S., J. Hult and C. F. Kaminski (2004). "Spectroscopic use of a novel blue diode laser in a wavelength region around 450 nm." Applied Physics B-Lasers And Optics **79**(4): 491-495.

Conroy, R. S., J. J. Hewett, G. P. T. Lancaster, W. Sibbett, J. W. Allen and K. Dholakia (2000). "Characterisation of an extended cavity violet diode laser." Optics Communications **175**(1-3): 185-188.

de Labachelerie, M. and G. Passedat (1993). "Mode-Hop Suppression of Littrow Grating-Tuned Lasers." Applied Optics **32**(3): 269-274.

Demtröder, W. (2003). Laser Spectroscopy. Berlin, Springer-Verlag.

Favre, F., D. Le Guen, J. C. Simon and B. Landousies (1986). "External-Cavity Semiconductor Laser with 15 nm Continuous Tuning Range." Electronics Letters **22**.

Gustafsson, U., J. Alnis and S. Svanberg (2000). "Atomic spectroscopy with violet laser diodes." American Journal of Physics **68**(7): 660-664.

Harvey, K. C. and C. J. Myatt (1991). "External-Cavity Diode-Laser Using a Grazing-Incidence Diffraction Grating." Optics Letters **16**(12): 910-912.

Hawthorn, C. J., K. P. Weber and R. E. Scholten (2001). "Littrow configuration tunable external cavity diode laser with fixed direction output beam." Review of Scientific Instruments **72**(12): 4477-4479.

Hildebrandt, L. (2004). Personal Communication (reported to me by J. Hult).

Hildebrandt, L., R. Knispel, S. Stry, J. R. Sacher and F. Schael (2003). "Antireflection-coated blue GaN laser diodes in an external cavity and Doppler-free indium absorption spectroscopy." Applied Optics **42**(12): 2110-2118.

Hult, J., I. S. Burns and C. F. Kaminski (2005a). "Two-line atomic fluorescence flame thermometry using diode lasers." Proceedings Of The Combustion Institute **30**: 1535-1543.

Hult, J., I. S. Burns and C. F. Kaminski (2005b). "Wide-bandwidth mode-hop-free tuning of extended-cavity GaN diode lasers." Applied Optics **44**(18): 3675-3685.

Jiang, H. X. and J. Y. Lin (1999). "Mode spacing "anomaly" in InGaN blue lasers." Applied Physics Letters **74**: 1066-1068.

Laurila, T., R. Oikari and R. Hernberg (2005). "Tunable diode laser spectrocopy of copper, cadmium, and indium at 325 nm." Spectrochimica Acta, Part B: Atomic Spectroscopy **60**: 783-791.

Leinen, H., D. Glassner, H. Metcalf, R. Wynands, D. Haubrich and D. Meschede (2000). "GaN blue diode lasers: a spectroscopist's view." Applied Physics B-Lasers and Optics **70**(4): 567-571.

Littman, M. G. and H. J. Metcalf (1978). "Spectrally Narrow Pulsed Dye-Laser without Beam Expander." Applied Optics **17**(14): 2224-2227.

MacAdam, K. B., A. Steinbach and C. Wieman (1992). "A Narrow-Band Tunable Diode-Laser System with Grating Feedback, and a Saturated Absorption Spectrometer for Cs and Rb." American Journal of Physics **60**(12): 1098-1111.

Mellis, J., S. A. Alchalabi, K. H. Cameron, R. Wyatt, J. C. Regnault, W. J. Devlin and M. C. Brain (1988). "Miniature Packaged External-Cavity Semiconductor-Laser with 50 GHz Continuous Electrical Tuning Range." Electronics Letters **24**(16): 988-989.

Merimaa, M., H. Talvitie, P. Laakkonen, M. Kuittinen, I. Tittonen and E. Ikonen (2000). "Compact external-cavity diode laser with a novel transmission geometry." Optics Communications **174**(1-4): 175-180.

Nakamura, S., M. Senoh, S. Nagahama, N. Iwasa, T. Yamada, T. Matsushita, Y. Sugimoto and H. Kiyoku (1997). "Longitudinal mode spectra and ultrashort pulse generation of InGaN multiquantum well structure laser diodes." Applied Physics Letters **70**: 616-618.

Nilse, L., H. J. Davies and C. S. Adams (1999). "Synchronous tuning of extended cavity diode lasers: the case for an optimum pivot point." Applied Optics **38**(3): 548-553.

Ricci, L., M. Weidemueller, T. Esslinger, A. Hemmerich, C. Zimmermann, V. Vuletic, W. König and T. W. Hänsch (1995). "A compact grating-stabilized diode laser system for atomic physics." Optics Communications **117**(5/6): 541.

Tisch, U., B. Meyler, O. Katz, E. Finkman and J. Salzman (2001). "Dependence of the refrctive index of $Al_xGa_{1-x}N$ on temperature and composition at elevated temperatures." Journal of Applied Physics **89**: 2676-2685.

Trutna, W. R. and L. F. Stokes (1993). "Continuously Tuned External-Cavity Semiconductor-Laser." Journal of Lightwave Technology **11**(8): 1279-1286.

Wieman, C. E. and L. Hollberg (1991). "Using Diode-Lasers for Atomic Physics." Review of Scientific Instruments **62**(1): 1-20.

Yan, G. Y. and A. L. Schawlow (1992). "Measurement of Diode-Laser Characteristics Affecting Tunability with an External Grating." Journal of the Optical Society of America B-Optical Physics **9**(11): 2122-2127.

Chapter 3

High-resolution spectroscopy of atomic indium using extended-cavity blue/violet diode lasers

3.1 Introduction

This chapter describes a practical application of the blue/violet extended cavity diode lasers (ECDLs) whose design and spectral characterisation were addressed in Chapter 2. The applicability of these ECDL systems to high-resolution spectroscopy is demonstrated, thus providing further evidence of the spectral purity and stability of the custom-designed laser systems. Spectra of atomic indium, seeded in flames at trace levels, were recorded both in fluorescence and in absorption. This confirms the potential for indium to be used as a probe species for diode-laser measurements of flame temperature, which will be the subject of Chapters 4 and 5.

This work represents the first use of blue diode lasers in fluorescence spectroscopy of flames (Hult et al. 2004). There has been only one previous demonstration of diode-laser-induced fluorescence in flames (Peterson and Oh 1999) and that experiment was done with a frequency-doubled red diode

laser. Atomic indium is one of a number of species that have strong spectral lines in the blue/violet region; it has electronic transitions both at 410.2 nm and at 451.1 nm. High-spectral-resolution laser-induced fluorescence (LIF) spectroscopy has been performed in an atmospheric-pressure flame on both of these indium transitions (Burns et al. 2004; Hult et al. 2004), and the acquired data show excellent agreement with a model that takes into account the hyperfine-structure of the indium atom. Previous uses of blue-violet diode lasers to probe molecular and atomic spectra have been restricted to the wavelength region between 395 nm and 417 nm. By contrast, the research described here includes the first spectroscopic use of a new range of blue diode laser emitting in a higher wavelength region around 450 nm (Burns et al. 2004). In the past, it was necessary, for example to use a frequency doubled Ti:Saphire laser to generate wavelengths of around 450 nm (Rasbach et al. 2004).

The study of the spectral line-shape of the indium transitions, which is presented in this chapter, is of relevance to the subsequent implementation for flame temperature measurements: the influence of temperature and composition on the pressure-broadening of the indium lines cannot be reliably predicted from theory, therefore experimental measurements of these effects are vital. Other experimental aspects are addressed: firstly, a determination of the spatial resolution of the LIF measurement is made; secondly, LIF spectra were acquired at a range of laser powers to ensure that the experiments were being conducted within the linear excitation regime.

This Chapter begins by briefly outlining the physical basis for the spectra that are shown, and the experimental method is then described. The presentation and discussion of the results concentrates on the indium fluorescence spectra,

which are of principal interest, but absorbance spectra are also shown, thus allowing the absolute number density of seeded indium atoms to be estimated.

3.2 Spectroscopy background and theory

Atoms and molecules absorb or emit light as a result of a transition to a different energy state. The energy of the photon that is emitted (or absorbed) is equal to the energy that is lost (or gained) by the atom or molecule. The energy states in which a particular atom or molecule might exist are determined by quantum mechanics (Svanberg 2004). The set of possible energy states is not a continuum, but is instead a set of discrete levels. It follows that the atom or molecule can emit or absorb only light at certain particular frequencies, at which the energy of the photon ($E=h\nu$) corresponds to the separation in energy between two of the discrete states. It is for this reason that the interaction of light has been used so extensively in determining the structure of atoms and molecules (Herzberg 1950; Banwell 1994). The set of energy states of an atom is related to the electronic structure of the atom; i.e. to the eigenvalues corresponding to wavefunctions that are solutions of the Schrödinger equation (Eckbreth 1996). These wavefunctions describe the various possible configurations in which the electrons can be arranged around the nucleus. Transitions only occur between certain pairs of energy states according to selection rules, which are derived quantum-mechanically.

In the case of molecules, each of the electronic transitions has fine structure due to the effects of rotation and vibration. The discussion of molecular spectra will be taken further in Chapter 6, which reports on the spectroscopy of $^{130}Te_2$. Instead, let us now consider the electronic structure of the indium atom in more detail.

3.2.1 Atomic indium spectroscopy

This chapter concerns the spectroscopy of atomic indium so some information on its electronic structure is given here. A broader review of the general background of atomic spectroscopy can be found elsewhere (Eckbreth 1996). The electronic ground state configuration of atomic indium is $4d^{10}5s^{2}5p^{1}$, where s, p, and d relate to electronic angular momentum quantum numbers (l) of 0, 1 and 2 respectively. The ground state of indium is split into two closely spaced sub-levels, as shown in Figure 3.1, characterised by different total angular momentum quantum number (J). The total angular momentum results from the coupling of the total orbital angular momentum of the atom (L) with the spin quantum number (S) and J can take integer values between (L+S) and $|L\text{-}S|$. For the case of the ground state, J = 1/2, 3/2 so the spin-orbit split levels are $5^{2}P_{1/2}$ and $5^{2}P_{3/2}$, whereas the excited state shown in Figure 3.1 has only J = 1/2.

The nuclei of atoms also possess an angular momentum denoted by the quantum number I. Both natural isotopes of indium, ^{115}In and ^{113}In (relative abundances of 95.7% and 4.3% respectively), have nuclear angular momentum of I = 9/2 (Mills et al. 1988). The coupling of this nuclear angular momentum I to the total angular momentum of the atom J, to give F, the total angular momentum of the whole atom, leads to a further splitting of the energy levels, known as 'hyperfine-splitting'. However, this effect is substantially weaker than the spin-orbit coupling, leading to a much smaller splitting of the energy level. The F quantum number may vary by integer values between (J+I) and $|J\text{-}I|$. For the $5^{2}P_{1/2}$ and $6^{2}S_{1/2}$ states of indium, F = 4, 5 but for the $5^{2}P_{3/2}$ state, F = 3, 4, 5, 6. This leads to the energy level

diagram shown in Fig. 3.1, in which the hyperfine splittings have been taken from the literature (Deverall et al. 1953).

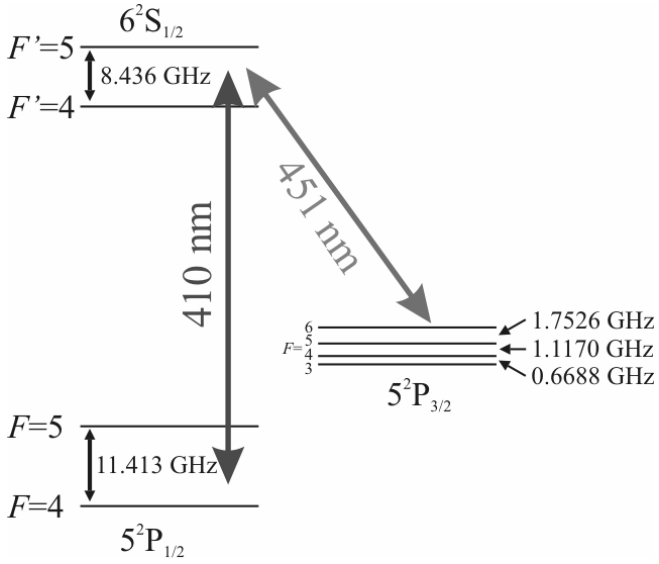

Figure 3.1. Detailed electronic energy structure of the indium atom.

Selection rules dictate that only certain transitions are allowed so that excitations can only occur for which $\Delta F = 0, \pm 1$. The result is that a high resolution spectrum of the $5^2P_{1/2} \rightarrow 6^2S_{1/2}$ transition near 410.2 nm consists of four peaks corresponding to the 4→4', 4→5', 5→4', 5→5' lines, where the prime symbol is used to denote the upper level of the transition. An excitation scan over the $5^2P_{3/2} \rightarrow 6^2S_{1/2}$ transition, near 451.1 nm, would lead to six peaks, corresponding to the 3→4', 4→4', 4→5', 5→4', 5→5' and 6→5' lines. This information is of importance in understanding the spectra that will be shown in the results section below, which were acquired at atmospheric pressure. The spectra we obtained are of sufficient resolution for the contributions of the individual hyperfine components to be apparent. The

following section will discuss another influence on the shape and structure of the acquired spectra: line-broadening.

3.2.2 Broadening of spectral lines

The line-shape of a transition refers to the spread of wavelengths of light that is emitted by an excited atom or molecule. For a number of reasons, the light that is emitted or absorbed is never purely monochromatic. A number of physical processes are responsible for the spectral broadening of the transition, and these therefore influence the shape of the spectral signature associated with each species. The first of these, natural broadening (Demtröder 2003), can be understood by the description of the excited atom as a damped oscillator. Since the amplitude of the oscillation decreases gradually, the frequency of the emitted radiation is not monochromatic as it would be for an undamped oscillator. The spectral profile of the emitted light is determined by taking the Fourier transform of the damped oscillation function, which results in a Lorentzian lineshape. Natural broadening is only significant when both temperature and pressure are very low, and will not be discussed here.

Another broadening mechanism, Doppler broadening, results from the motion of the atom or molecule as it interacts with the photon. If the atom is moving away from the photodetector then the emitted light will appear to be of longer wavelength, and vice versa. In a gaseous sample, the thermal motion of individual atoms and molecules leads to a Gaussian broadening of the transition line-shape (Eckbreth 1996) of the form:

$$g_D(\nu) = \frac{c}{\nu_0}\sqrt{\frac{m}{2\pi kT}}\exp\left[-4\ln 2\frac{(\nu-\nu_0)^2}{\Delta\nu_D^{\,2}}\right]. \qquad (3.1)$$

Here, c is the speed of light, ν_0 is the centre frequency of the transition, m is the molecular mass, k is the Boltzmann constant, T is the temperature, and $\Delta\nu_D$ is the full-width at half maximum height (FWHM) of the Doppler profile, which is defined as:

$$\Delta\nu_D = \frac{2\nu_0}{c}\sqrt{\frac{2\ln 2kT}{m}}\,. \qquad (3.2)$$

It follows that, for a particular atom or molecule, the Doppler width is a function only of temperature.

The linewidth of atomic and molecular transitions is also influenced by pressure broadening, and is the result of collisions between the molecules. When pressure broadening is dominant, the transition has a Lorentzian line-shape (Eckbreth 1996), of the form:

$$g_L(\nu) = \frac{\Delta\nu_L}{2\pi}\frac{1}{(\nu-\nu_0)^2 + \left(\frac{\Delta\nu_L}{2}\right)^2}. \qquad (3.3)$$

Here, $\Delta\nu_L$ is the Lorentzian line-width. The relationship of the Lorentzian line-width to parameters such as temperature is rather complex, and is not easily determined from theory. The Lorentzian width tends to be inversely

proportional to the temperature raised to an exponent (η), i.e. $\Delta\nu_L \sim T^{-\eta}$; simple assumptions lead to a value of $\eta \cong 0.7$; this issue is addressed in greater detail in Chapter 5. The influence of the collisions between atoms or molecules depends on the overlap between their energy levels, thus the line-shape may be dependent on composition. Certain species have particular broadening partners whose influence is much more significant than that of other species. Molecular collisions are also responsible for a shift of the centre frequency of the line, in addition to broadening. The magnitude of the line-shift is often directly proportional to the Lorentzian width for a particular species and broadening partner (Eberz et al. 1984). As a consequence of these factors, it is impossible confidently to predict the shape of pressure-broadened spectra without high spectral-resolution experimental data. The results shown for atomic indium in this Chapter are of interest in this context.

Under certain conditions, either one or other of these two broadening mechanisms can be considered dominant and the other neglected. For atoms and molecules at flame conditions, however, the Doppler width and Lorentzian width are often of similar magnitude so this approximation is not valid. A more general description is of the spectral lineshape is given by the convolution of the Doppler and Lorentz functions in Eqns. 3.1 and 3.3. It can be shown that this leads to a line-shape described by the following equation, which is known as a Voigt profile (Eckbreth 1996).

$$g(\nu) = \frac{2}{\Delta\nu_D}\sqrt{\frac{\ln 2}{\pi}}\left(\frac{a}{\pi}\int_{-\infty}^{\infty}\frac{e^{-y^2}}{a^2+(x-y)^2}dy\right). \qquad (3.4)$$

Here, the variables *a* and *x* are defined as:

$$x = 2\sqrt{\ln 2}\,\frac{(\nu - \nu_0)}{\Delta\nu_D}. \tag{3.5}$$

$$a = \sqrt{\ln 2}\,\frac{\Delta\nu_L}{\Delta\nu_D} \tag{3.6}$$

The '*a*' term is a parameter which gives information about the relative importance of the Doppler and Lorentzian components of the shape. If a<<1, then the profile is well-approximated by a Doppler shape; otherwise, if a>>2, the shape is similar to a Lorentzian profile (Eckbreth 1996).

3.3 Experimental method

Experiments were performed with both of the extended cavity diode lasers (ECDL) that were described in Chapter 2. The diode laser emitting near 410.2 nm was used to excite the indium atoms via the $5^2P_{1/2} \rightarrow 6^2S_{1/2}$ transition; in a second experiment, the 451.1 nm diode laser was used to excite the $5P_{3/2} \rightarrow 6^2S_{1/2}$ transition. High-resolution spectra of these transitions were obtained both in fluorescence and in absorption.

The equipment set-up is shown in Figure 3.2; the method followed was the same in the case of each of the two ECDLs. Tuning of the ECDL wavelength was performed exactly as described in Chapter 2; the tuning signal was a triangular waveform with a frequency of 20 Hz. Part of the laser beam was reflected by a glass plate toward a solid quartz etalon (FSR=3.02), which was used to ensure that the scan was mode-hop free. The spacings between the

transmission peaks of the etalon trace also made it possible, during the post-processing, to correct for slight non-linearities in the wavelength scanning rate. A second glass plate was used to direct a reflection of the laser beam towards a photodiode, which was used to measure the relative laser intensity. A laser-power meter (OPHIR, PD200) was used to calibrate this intensity measurement before the laser scanning was commenced. The laser beam was focussed (f=300 mm) to a point on the central axis of a stable Mèker burner. A third photo-diode was used to measure the power of the laser beam after it had passed through a flame. This allowed laser absorption spectra to be obtained. Laser-induced fluorescence was imaged ($f^{\#}$ = 2.4), through a pin-hole (d = 500 μm); 2f imaging was performed so the spatial resolution is defined by a cylinder of length 500 μm, and of diameter equal to the beam-waist of the focussed laser beam (evaluated below). A photomultiplier tube (Hamamatsu; R3788) was used to detect fluorescence in the $5^2P_{3/2} \rightarrow 6^2S_{1/2}$ transition by use of a band-pass interference filter (CVI; $\Delta\lambda$ = 3 nm) centred on 451.1 nm. For excitation with the 451.1 nm ECDL, this means that the excitation and detection were performed at the same wavelength (i.e. resonance fluorescence was conducted). Nevertheless, the background intensity level was low since the level of particulate material in the flames being studied was insignificant. The photomultiplier tube was mounted on a set of translation stages permitting fine adjustment in three perpendicular directions. It was aligned with no gas-flow through the burner by detecting light scattered from a piece of card, mounted on the burner plate so that the laser beam was incident on it. The signal from the photomultiplier tube was pre-amplified (Gain = 10^5; bandwidth = 20 kHz); all of the signals were digitised using an oscilloscope and transferred to a PC via a GPIB interface.

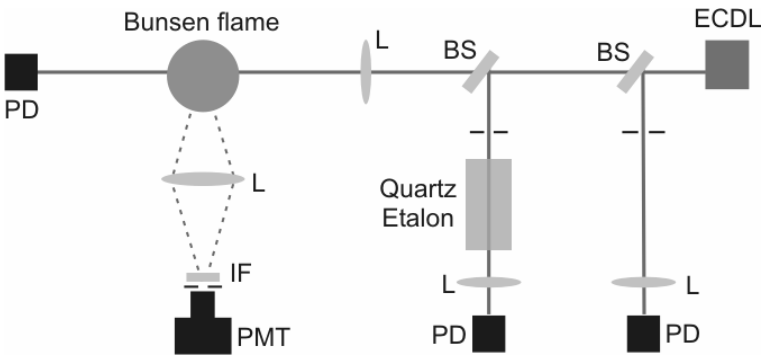

Figure 3.2. The experimental set-up for the simultaneous acquisition of fluorescence and absorption spectra of atomic indium. (L: lens; IF: interference filter centred around 451 nm; PMT: photomultiplier tube; PD: photodiode; BS: beam splitter; ECDL: extended-cavity diode laser)

Since no wavemeter was available during this project, the ECDLs were tuned to resonance by looking for the fluorescence signal. The method followed was identical for both lasers: a single-mode wavelength scan was initiated; then coarse wavelength tuning was performed by adjusting the thumb screw on the kinematic mount (Thorlabs, KC1-PZ) holding the grating (see Figure 2.4); at intervals during this coarse tuning, it was necessary to re-adjust the electronic signals for laser tuning to maintain single-mode scanning. The device only operates as an extended cavity laser over a finite range of grating angles because, for it to do so, there must be sufficient overlap between the wavelength of the optical feedback from the grating and the diode gain curve (see Figure 2.3). The kinematic mount allowed the grating angle to be adjusted throughout this useful range. At one of these angles, a fluorescence signal was observed on the oscilloscope as a feature that was raised from the flat background level. Thereafter, careful adjustment of the electrical signals driving the piezo-actuators in the grating mount was performed with the intention of achieving a mode-hop free scan covering the entire indium

transition. In order that the indium transition should be in the centre of the laser scan, the laser wavelength was finely adjusted either by small changes to the diode laser temperature, or to the grating angle via piezo-actuator 'A' (see Figure 2.4). The effect of this was slightly to alter the maximum and minimum wavelengths of the laser scan, while maintaining a similar scanning range. Fine adjustment of the offsets on the piezo-actuator driving signals was required from time to time during the experiment in order to compensate for thermal expansion of the extended cavity. It is thought that this effect was exacerbated by the presence of burner (and in the case of the experiments reported in Chapter 6, also a small furnace) which considerably increased the ambient temperature in the laboratory.

The burner that was used for these experiments was designed and commissioned by Mr G. Hartung, and was used with his kind permission. The burner consisted of a brass plate with a large number of capillary holes drilled into it (diameter = 500 μm; spacing = 250 μm). A flat flame of premixed methane and air was stabilised on this device; the reaction zone was situated approximately 1 mm above the surface of the burner plate. Experiments were performed in the post-combustion region. The flow was divided into a central flame seeded with indium atoms (diameter= 40 mm), which was surrounded by an unseeded co-annular flame (diameter= 60 mm) of the same composition. The seeding was performed by passing a part of the air stream for the inner flame through a nebuliser, prior to pre-mixing. The nebuliser contained an aqueous solution of $InCl_3$ (concentration ~ 0.05 M). This led to the presence of small solid crystals of $InCl_3$ in the unburnt gases, which decomposed in the pre-heat zone of the flame to liberate neutral indium atoms. This meant that, in the seeded region, there was no radial gradient in

temperature or in the concentration of indium atoms (James and Sugden 1955). This is significant since a line-of-sight absorption measurement will be used to determine the number density of indium atoms in the flame; due to the homogeneity of the flame, this result of this average measurement is equal to the local concentration at the measurement volume for the laser-induced fluorescence signal. Calibration measurements of temperature in this burner were performed by Mr G. Hartung, using the techniques of Na-line, at a range of equivalence ratios and at a range of heights above the burner (HAB). A description of the Na-line reversal technique is available in the literature (Alkemade 1982). These reference measurements were useful, for example, in calculating the expected Doppler broadening. The spectra that will be shown in this Chapter were recorded at a height of 12 mm above the burner plate and the equivalence ratio of the flame was $\phi = 1.0$.

Two supplementary experiments were also performed. The first was done to ensure that the LIF experiments were being done within the linear excitation regime. A range of neutral density filters was used to vary the excitation power of the 451.1 nm diode laser, and fluorescence spectra were recorded in each case. This allowed the relationship between excitation power and fluorescence intensity to be determined. Secondly, the spatial resolution of the LIF experiment was estimated by translating a razor-blade across the laser beam at the focal position. This was done both in the horizontal direction and in the vertical direction, and thus allows the beam-waist and spatial-profile at the focus to be determined.

3.4 Results and discussion

3.4.1 Indium LIF spectra

The single-mode tuning range of the ECDL systems allowed scanning of the laser wavelength over the entire width of both indium transitions, as shown in Figures 3.3 and 3.4. The spectra have been normalised by the simultaneously recorded laser power. The laser power that was used for this normalisation was compensated to take account of absorption of the laser beam before reaching the measurement volume on the central axis of the burner; this could be done because the flame was homogeneous.

The spectra that are shown here were recorded at a height of 12 mm above the burner plate in a flame with equivalence ratio of $\phi = 1.0$. Shown in Figure 3.3 are an average spectrum of 128 single scan spectra, a single-scan spectrum obtained in 50 ms, and a theoretical fit to the averaged spectrum. The simultaneously recorded etalon fringe pattern was used to establish a linear frequency scale for the scan. The $5^2P_{1/2} \rightarrow 6^2S_{1/2}$ transition at 410 nm consists of four hyperfine components, the positions and strengths of which are also indicated in Figure 3.3.

A theoretical spectrum representing the sum of four Voigt profiles, which correspond to the four hyperfine lines of the transition, was fitted to the averaged experimental spectrum using a non-linear least squares routine; the four individual Voigt profiles are also shown in Figure 3.3. A total of four parameters were varied during the fitting procedure: the position of the first hyperfine line; the intensity of the first hyperfine line; the pressure broadening coefficient; and the background intensity. A Doppler broadening coefficient of 2.29 GHz was calculated (Eqn. 3.2) for the temperature of 2200 K, which

resulted from the Na-line reversal reference measurements mentioned above, and was specified in the fit. The hyperfine peak separations (Deverall et al. 1953) and the relative intensities (1.0, 0.67, 0.37, 1.0) of the hyperfine lines (Leinen et al. 2000) were also specified in the fitting routine. The background intensity resulted predominantly from flame chemiluminescence, the contribution of scattered laser light being much less significant.

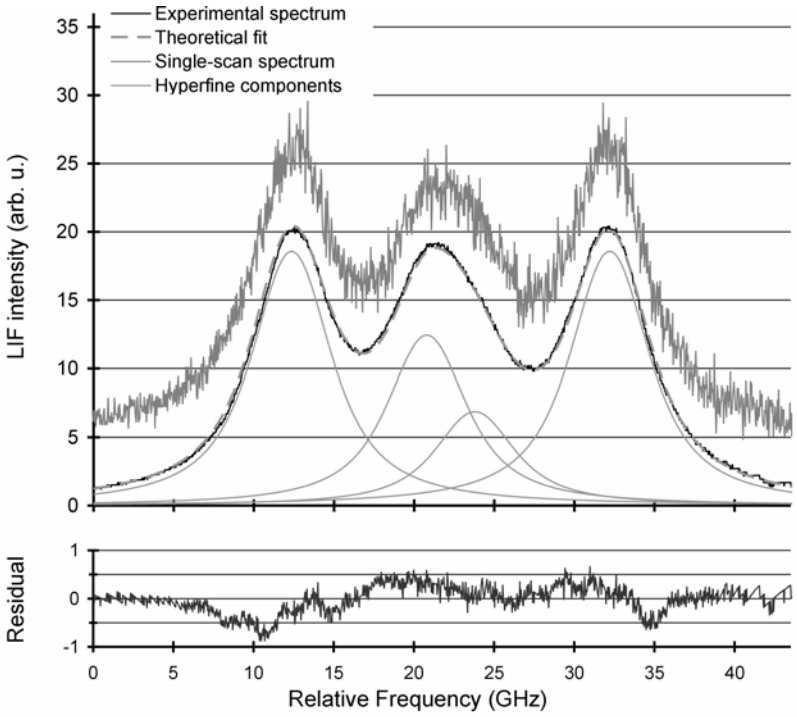

Figure 3.3. Indium fluorescence spectrum of the $5^2P_{1/2} \rightarrow 6^2S_{1/2}$ transition near 410.2 nm. An averaged spectrum is shown along with a theoretical fit of the sum of four Voigt profiles. The Voigt profiles are also shown and represent the individual hyperfine components. A single-scan spectrum is shown offset from the base-line for clarity. The residual between the averaged spectrum and the theoretical fit is shown on separate axes.

The spectrum is subject to significant collisional broadening at atmospheric pressure. As a result, the four hyperfine peaks appear merged together. The fitted Voigt profiles yield a pressure broadening component of around 4.99

GHz. This results in an '*a*' parameter (defined by Eqn. 3.6) of 1.82. This means that the individual hyperfine components of the spectrum would not be well-approximated either by pure Gaussian functions or by pure Lorentzian functions. The use of the more complicated Voigt function is thus essential to describe the spectral shape of indium correctly at flame conditions. Note that the total width of the $5^2P_{1/2} \rightarrow 6^2S_{1/2}$ transition is observed to be around 25 GHz, which is considerably wider than what has previously been assumed by other researchers (2 GHz (Dec and Keller 1986)), who apparently neglected to take account either of the fact that there are multiple hyperfine components, or of the existence of pressure broadening in addition to Doppler broadening.

Figure 3.4 shows the corresponding LIF excitation spectrum of the $5^2P_{3/2} \rightarrow 6^2S_{1/2}$ transition of atomic indium at 451.1 nm. This consists of six closely spaced hyperfine transitions, as indicated. A theoretical fit of six Voigt profiles was made to the average of 128 individual normalised spectra and is also shown in Figure 3.4. The same curve fitting procedure was followed as in the case of the $5^2P_{1/2} \rightarrow 6^2S_{1/2}$ transition at around 410.2 nm, discussed above. In this case, a Doppler broadening coefficient of 2.08 GHz was calculated from Eqn. 3.2 for a temperature of 2200 K, and was specified in the fit. The relative intensities of the hyperfine peaks have been estimated (Burns et al. 2004) to be (in order of increasing frequency): 0.34, 0.51, 0.54, 1.0, 0.51, 0.18. These were also specified in the fitting procedure, as were the relative peak positions (Deverall et al. 1953). Again, it can be seen from Figure 3.4 that the theoretical fit is in excellent agreement with the experimental data. A pressure broadening coefficient of 4.78 GHz was measured here, which is slightly smaller than for the $5^2P_{1/2} \rightarrow 6^2S_{1/2}$ transition. A similar discrepancy between the estimated Lorentzian widths for the two

transitions was observed at a range of flame conditions. In fact, this is consistent with previous findings for other group III metals (Cheron et al. 1977), in which the transition from the upper spin-orbit split level of the ground state also showed slightly lower collisional broadening. Note that background levels in the fit were close to zero even for this resonance fluorescence spectrum.

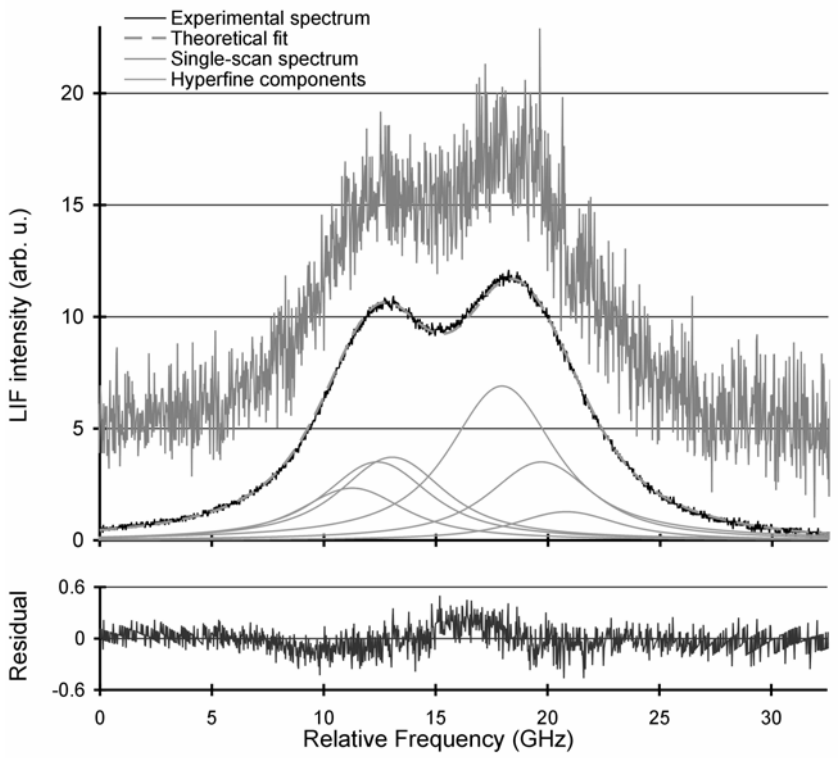

Figure 3.4. Indium fluorescence spectrum of the $5^2P_{3/2} \rightarrow 6^2S_{1/2}$ transition near 451.1 nm. An averaged spectrum is shown along with a theoretical fit of the sum of six Voigt profiles. The Voigt profiles are also shown and represent the individual hyperfine components. A single-scan spectrum is shown offset from the base-line for clarity. The residual between the averaged spectrum and the theoretical fit is shown on separate axes.

3.4.2 Indium Absorbance Spectra

During these experiments, the level of indium seeding was such that there was non-negligible absorption of the laser beam as it passed through the flame. It has been stated above that this effect had to be taken account of when normalising the fluorescence spectra. As already noted in Chapter 1, the absorbance is linearly proportional to the absorption cross-section.

$$Absorbance = \log_{10}\left(\frac{I_0}{I}\right) = \log_{10}\left(e^{N_1\sigma_{12}L}\right) \tag{3.7}$$

Here, I_0 is the incident laser power, I is the transmitted laser power, N_1 is the number density of atoms in the ground state of the transition, L is the absorption path-length, and σ_{12} is the absorption cross-section for the transition from a lower state '1' to an upper state '2'. The shape of the absorbance spectrum is therefore not a function of the concentration of the absorber. The LIF spectra are also linearly proportional to the absorption cross-section, assuming the saturation laser irradiance is not exceeded (see below). Therefore, the absorbance and fluorescence spectra are expected to have the same shape.

Shown in Figure 3.5 is an absorbance spectrum of the $5^2P_{1/2}\rightarrow 6^2S_{1/2}$ transition, which was recorded simultaneously to the LIF spectrum shown in Figure 3.3. The raw spectra were noisy since the absorbance represents a measurement of the change in the laser power by a small fraction of its total value.

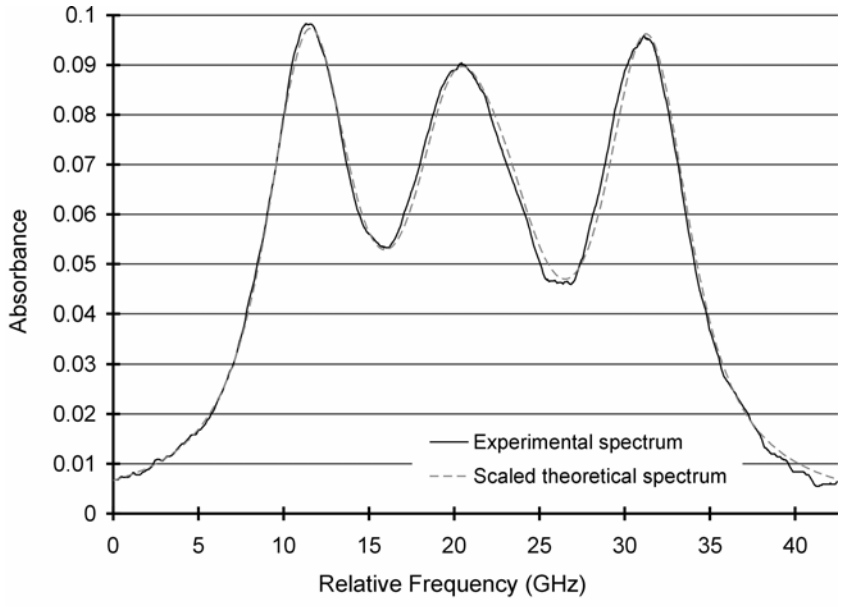

Figure 3.5. Absorbance spectrum of the $5^2P_{1/2} \rightarrow 6^2S_{1/2}$ transition of atomic indium near 410.2 nm. A fitted theoretical spectrum is also shown.

To compensate for this noise, the absorbance spectra were smoothed during post-processing by replacing the value at each data-point with the boxcar-type average (boxcar width=25 pixels ~ 0.75 GHz) of the surrounding data-points. The theoretical spectrum, shown in Figure 3.5 together with the experimental spectrum, has the same shape as the one shown in Figure 3.3, and was fitted to the absorbance data with an intensity scaling factor as the only free parameter. This was done because the LIF spectrum had a much better signal-to-noise ratio, and thus provides a better estimate of the Lorentzian width, and the position of the first hyperfine peak.

The absorbance also allows the total number density of indium atoms in the seeded region of the flame to be determined. The integral of the absorbance spectrum can be expressed as:

$$\begin{aligned}\int_{-\infty}^{\infty}\log_{10}\left(\frac{I_0}{I}\right)d\nu &= \int_{-\infty}^{\infty}\log_{10}\left(e^{N_1\sigma_{12}L}\right)d\nu \\ &= 0.4343N_1L\int_{-\infty}^{\infty}\sigma_{12}d\nu \\ &= 0.4343N_1L\tilde{\sigma}_{12} \\ &= 0.4343N_1L\tilde{\sigma}_0 f_{12}\end{aligned} \tag{3.8}$$

Here, $\tilde{\sigma}_{12}$ is defined as the frequency-integrated absorption cross-section, and can be expressed as the product of the oscillator strength (f_{12}) and $\tilde{\sigma}_0$, where $\tilde{\sigma}_0$ is a constant with the value $\tilde{\sigma}_0$=2.654 x 10^{-6} m^2s^{-1} (Axner et al. 2004). The oscillator strength is a scalar multiple of the Einstein coefficient for spontaneous emission (A_{21}) (Axner et al. 2004):

$$f_{12} = f_{ref}\left(\frac{g_2}{g_1}\right)\left(\frac{\lambda_{12}}{\lambda_{ref}}\right)^2\left(\frac{A_{12}}{A_{ref}}\right) \tag{3.9}$$

Here, the constants take the following values (Axner et al. 2004): A_{ref} = 1.367 x 10^7 s^{-1}; f_{ref} = 0.05740; λ_{ref} = 529.177 nm. The value of the Einstein coefficient for the $5^2P_{1/2}\rightarrow 6^2S_{1/2}$ transition in indium at 410.2 nm is A_{21} = 0.56 x 10^8 s^{-1} (NIST 2006). From Figure 3.1, it is apparent that the degeneracies for both levels of this transition are $g_1 = g_2 = 2$. Therefore, by application of Eqn. 3.9, the oscillator strength of the transition is found to be f_{12} = 0.141. By integrating the area under the theoretical spectrum shown in Figure 3.5 (this was done over a larger range of frequencies than the one shown in the figure), it was thus possible to determine that the number density of indium atoms in the $5^2P_{1/2}$ state in the flame (path-length, L=40 mm) was

3.6×10^{17} m^{-3}, or 108 ppbv. Since the signal-to-noise ratio for the absorbance spectra was low, it is estimated that the accuracy of this measurement may be on the order of ±10 %.

A similar absorption spectrum was acquired for the $5^2P_{3/2} \rightarrow 6^2S_{1/2}$ transition at 451.1 nm, and is shown in Figure 3.6. The data were processed in the same way as has been described for the 410.2 nm transition; as before, the theoretical spectrum is the result of the fit to the corresponding LIF spectrum (shown in Fig 3.4), and has been normalised to have the same maximum value as the smoothed absorbance data. This transition has a spontaneous emission coefficient of $A = 1.02 \times 10^8$ s^{-1} (NIST 2006), which leads to an oscillator strength of 0.1556. The number density of indium atoms in the $5^2P_{3/2}$ state was thus estimated to be 1.7×10^{17} m^{-3} or 52 ppbv. Therefore, the total concentration of seeded indium atoms in the flame, at 12 mm above the burner plate, is estimated to have been 160 ppbv, since only the two ground states probed are significantly populated at the flame temperature. Due to the high oscillator strength of atomic species, this tiny seeding density is sufficient to generate strong LIF signals even with low-power diode laser excitation sources.

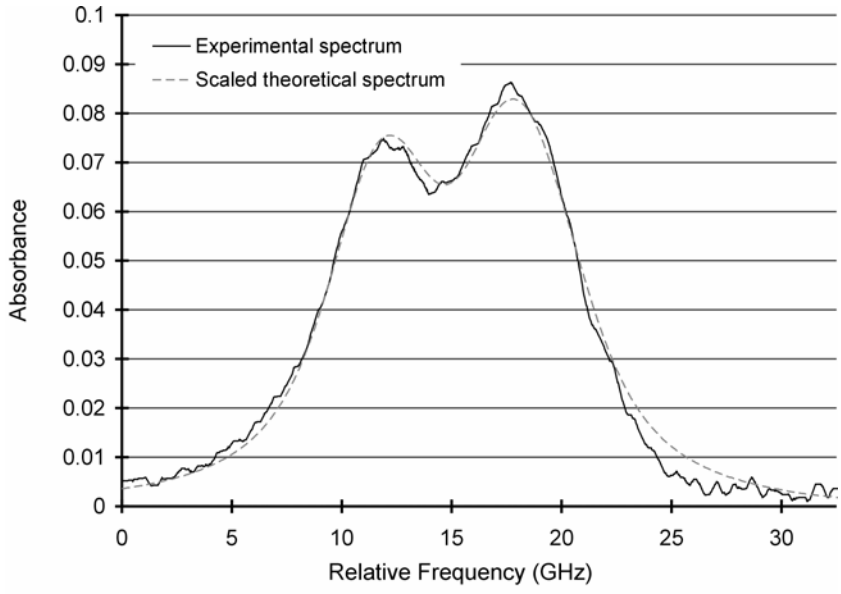

Figure 3.6. Absorbance spectrum of the $5^2P_{3/2} \rightarrow 6^2S_{1/2}$ transition of atomic indium near 451.1 nm. A fitted theoretical spectrum is also shown.

3.4.3 Spatial resolution determination

Attention has already been drawn to the great advantage that diode laser LIF measurements possess by comparison to absorption techniques in terms of spatial resolution. Figure 3.7 shows the results of an experiment to determine the spatial resolution of the LIF spectra shown above by measuring the spatial profile of the laser beam. The experiment involved translating a razor blade across the 410 nm laser beam at the focal position and measuring the intensity of the beam as an increasing fraction is blocked by the blade. The spatial irradiance was calculated by taking the derivative of the power measurement with respect to blade position. This was done in both the horizontal and vertical directions, and the results are shown in Figure 3.7.

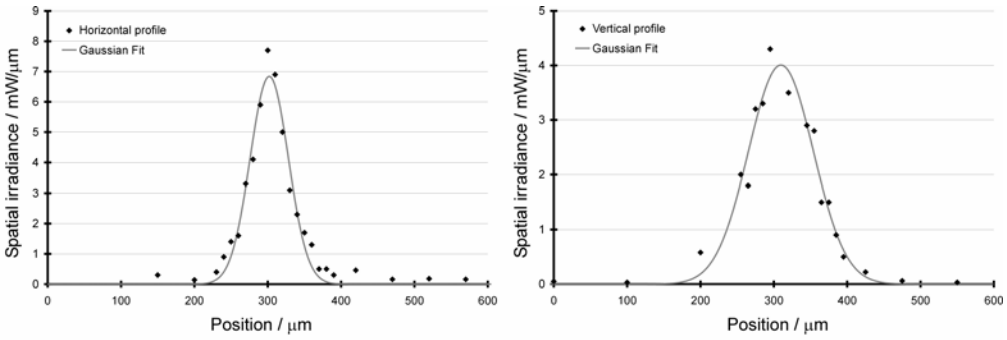

Figure 3.7. Spatial beam profile of the 410 nm laser beam at the focal position in both the horizontal and vertical directions. Fitted Gaussian profiles are also shown, the reasonable quality of the fit showing that the TEM_{00} transverse-mode is dominant.

A Gaussian profile was fitted to both of the spatial profiles and gives reasonable agreement in each case. This indicates that the TEM_{00} transverse mode is dominant over higher order transverse modes (Hecht 1987). The beam waist in each direction was approximated to be equal to the full-width-at-half-maximum-height (FWHM) of the fitted Gaussian. It was found that the beam waist in the horizontal direction (61 μm) was much lower than in the vertical direction (104 μm). The reason for this is that prior to being focussed, the laser beam profile is elliptical, with a width of approximately 2.5 mm and a height of around 5 mm. This is a consequence of the fact that the emission from the diode chip has greater divergence in one direction than the other. The diameter (d) of the diffraction-limited focal-spot of a Gaussian beam is given by (Demtröder 2003):

$$d = \frac{4 f \lambda}{D \pi} \tag{3.10}$$

Here, f is the focal length of the lens and D is the diameter of the laser beam at the lens. Therefore diffraction-limited spot diameters of d=31 μm in the horizontal direction, and d=62 μm in the vertical direction, can be estimated. In applications where it is critical to have a good spatial beam profile, such as frequency-doubling and sum-frequency mixing applications, an anamorphic prism pair (Zimmermann et al. 1995), or a cylindrical telescope, can be used to correct for this ellipticity, but this step was not considered to be necessary during the experiments reported here.

3.4.4 Linearity check

A check was made to ensure that the fluorescence signals (such as those shown in Figures 3.3 and 3.4) were directly proportional to the laser intensity. This experiment was performed by probing the $5^2P_{3/2} \rightarrow 6^2S_{1/2}$ transition of indium with the 451 nm ECDL. At high laser irradiance, this linear relationship breaks down due to depopulation of the lower level of the transition, which is known as saturation (Daily 1997). In Figure 3.8, the LIF signal strength is shown as a function of laser intensity.

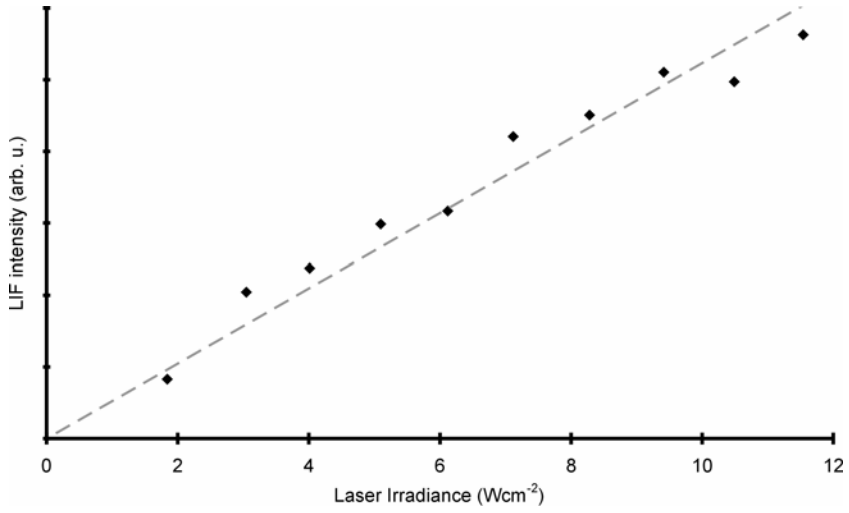

Figure 3.8. Fluorescence intensity in the $5^2P_{3/2} \rightarrow 6^2S_{1/2}$ transition of atomic indium near 451.1 nm as a function of laser irradiance.

A linear trend is apparent from this plot, so it is clear that no the laser irradiance was too low to cause saturation. In fact, previous studies using pulsed dye laser excitation sources have shown that the saturation irradiance for indium atoms in an atmospheric pressure flame is substantially greater than that used here (Engstrom 2001). This means that more powerful blue diode lasers, which are now available from Nichia, could be used in future studies to increase the signal-to-noise ratio, while remaining in the linear excitation regime.

3.5 Conclusions

The results described here represent a ground-breaking demonstration of directly excited diode laser induced fluorescence in flames. It has been shown that strong fluorescence signals may be obtained even with these low power excitation sources. Diode lasers have previously almost no role in the investigation of flames by laser induced fluorescence. The signal levels and

spectral resolution obtained demonstrate the excellent diagnostic potential of these light sources, which are used for flame thermometry in Chapters 4 and 5.

3.6 References

Alkemade, C. T. J., Hollander, Tj., Snelleman, W., Zeegers, P.J.Th. (1982). Metal Vapours in Flames. Oxford, Pergamon Press.

Axner, O., J. Gustafsson, N. Omenetto and J. D. Winefordner (2004). "Line strengths, *A*-factors and absorption cross-sections for fine structure lines in multiplets and hyperfine structure components in lines in atomic spectrometry -- a users guide." Spectrochimica Acta, Part B: Atomic Spectroscopy **59**: 1-39.

Banwell, C. N., McCash, E.M. (1994). Fundamentals of Molecular Spectroscopy. London, McGraw-Hill.

Burns, I. S., J. Hult and C. F. Kaminski (2004). "Spectroscopic use of a novel blue diode laser in a wavelength region around 450 nm." Applied Physics B-Lasers And Optics **79**: 491-495.

Cheron, B., R. Scheps and A. Gallagher (1977). "Noble-Gas Broadening of $6^2P_{1/2}$-$7^2S_{1/2}$ (377.6 nm) $6^2P_{3/2}$-$7^2S_{1/2}$ (535 nm) Thallium Lines." Physical Review A **15**: 651-660.

Daily, J. W. (1997). "Laser Induced Fluorescence Spectroscopy in Flames." Progress in Energy and Combustion Science **23**: 133-199.

Dec, J. E. and J. O. Keller (1986). "High-Speed Thermometry Using Two-Line Atomic Fluorescence." Proceedings of the Combustion Institute **21**: 1737-1745.

Demtröder, W. (2003). Laser Spectroscopy. Berlin, Springer-Verlag.

Deverall, G. V., K. W. Meissner and G. J. Zissis (1953). "Hyperfine Structures of the Resonance Lines of Indium (In^{115})." Physical Review **91**: 297-299.

Eberz, J., G. Huber, T. Kuhl and G. Ulm (1984). "Pressure Broadening and Pressure Shift of the 410-Nm Indium Line Perturbed by Foreign Gases." Journal of Physics B-Atomic Molecular and Optical Physics **17**: 3075-3082.

Eckbreth, A. C. (1996). Laser Diagnostics for Combustion Temperature and Species. Amsterdam, Gordon and Breach.

Engstrom, J. (2001). Development of a 2D Temperature Measurement Technique for Combustion Diagnostics using 2-line Atomic Fluorescence Lund Institute of Technology. PhD Thesis

Hecht, E. (1987). Optics. Reading, Massachusetts, USA, Addison-Welsley.

Herzberg, G. (1950). Molecular Spectra and Molecular Structure. New York, Van Nostrand Reinhold.

Hult, J., I. S. Burns and C. F. Kaminski (2004). "Measurements of the indium hyperfine structure in an atmospheric-pressure flame by use of diode-laser-induced fluorescence." Optics Letters **29**: 827-829.

James, C. G. and T. M. Sugden (1955). "Photometric investigations of alkali metals in hydrogen flame gases: 1. A general survey of the use of resonance radiation in the measurement of atomic concentrations " Proceedings of the Royal Society of London, Series A: Mathematical and Physical Sciences **227**: 312-329.

Leinen, H., D. Glassner, H. Metcalf, R. Wynands, D. Haubrich and D. Meschede (2000). "GaN blue diode lasers: a spectroscopist's view." Applied Physics B-Lasers and Optics **70**: 567-571.

Mills, I., T. Cvitas, K. Homann, N. Kallay and K. Kuchitsu (1988). Quantities, Units and Symbols in Physical Chemistry. Oxford, UK, Blackwell Scientific Publications.

NIST (2006). NIST Atomic Spectra Database.
http://physics.nist.gov/cgi-bin/AtData/lines_form

Peterson, K. A. and D. B. Oh (1999). "High-sensitivity detection of CH radicals in flames by use of a diode-laser-based near-ultraviolet light source." Optics Letters **24**: 667-669.

Rasbach, U., J. Wang, R. dela Torre, V. Leung, B. Kloter, D. Meschede, T. Varzhapetyan and D. Sarkisyan (2004). "One- and two-color laser spectroscopy of indium vapor in an all-sapphire cell." Physical Review A **70**.

Svanberg, S. (2004). Atomic and Molecular Spectroscopy. Berlin, Springer-Verlag.

Zimmermann, C., V. Vuletic, A. Hemmerich and T. W. Hänsch (1995). "All solid state laser source for tunable blue and ultraviolet radiation." Applied Physics Letters **66**: 2318-2320.

Chapter 4

Two-line atomic fluorescence (TLAF) temperature measurements in laminar flames with blue diode lasers

4.1 Introduction

In this section, a novel flame thermometry scheme based on diode-laser-induced fluorescence is described. This represents the first demonstration of spatially-resolved temperature measurement in flames using diode lasers. The low line-width and favourable tuning of the extended-cavity diode lasers allows high-fidelity fluorescence spectra to be recorded, which in turn leads to accurate thermometry. The technique involves probing two transitions in atomic indium, which is seeded to the flame in trace quantities: the ratio of the resulting fluorescence signals is related to the temperature. The new diode-laser-induced fluorescence method described here is not only more practical than previous flame thermometry approaches, but also offers the potential for enhanced accuracy and increased measurement repetition-rate.

Various alternative laser diagnostics for flame temperature measurement were described in Chapter 1 and their relative merits were discussed; one of the

methods introduced was two-line atomic fluorescence (TLAF). The TLAF technique was first implemented using flash-lamp excitation sources (Omenetto et al. 1972) and was later implemented using Ar^+ laser pumped continuous wave dye lasers (Joklik and Daily 1982; Dec and Keller 1986). Further development of the technique allowed it to be applied to two-dimensional imaging studies in internal-combustion engines (Kaminski et al. 1998) and in sooting flames (Engstrom et al. 2000). Attention was drawn in Chapter 1 to the fact that diode laser absorption thermometry is a path-averaged technique suitable only in homogeneous environments, and it was noted that all previous spatially-resolved flame temperature measurements have involved bulky and expensive high-power lasers. The first implementation of TLAF thermometry with blue diode laser sources is described here. The atomic fluorescence thermometry method has been brought into a new domain by the construction of a robust sensor whose compactness and low cost make it amenable to widespread use.

This Chapter begins by developing the equation relating the fluorescence signals to temperature through consideration of the population dynamics in a three-level atomic energy system, which is representative of species suitable for TLAF thermometry. This leads on to an analysis to decide which atom has the energy level separation that will give optimum temperature sensitivity. Temperature measurements by two-line atomic fluorescence have been performed in a premixed laminar Bunsen flame. The Chapter concludes with a discussion of the extent of errors that could result from absorption of the laser beam in the flame, and an evaluation of the increasing influence of shot-noise for faster measurements which will be performed in the future.

4.2 TLAF Theory

The atomic probe species used in TLAF thermometry should have a suitable three-level energy structure, in which the lower two levels have a separation in energy that causes their relative population to be a sensitive function of temperature. The upper level should be sufficiently separated from the other two so that its thermal population is negligible at flame temperature; therefore essentially all of the atoms reside in one of the two lower states. A number of excitation and detection schemes are possible: a fairly comprehensive list of these has been set-out previously (Zizak et al. 1984) and two of these variants, which will be discussed further here, are illustrated in Figure 4.1.

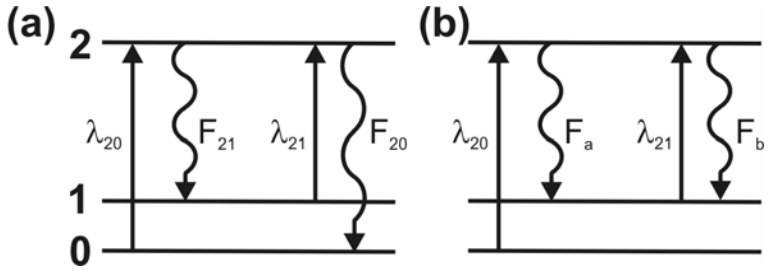

Figure 4.1 a) Conventional TLAF scheme; b) Modified TLAF scheme used in this study.

The more commonly employed TLAF scheme, in which two separate detectors are used (Haraguchi et al. 1977; Dec and Keller 1986) , is shown in Figure 4.1a. The two transitions are probed sequentially: first a laser with wavelength λ_{20} is used to excite the 0→2 transition. A detector with a band-pass filter is used to measure the fluorescence intensity F_{21} in the 2→1 transition. Subsequently, a laser at wavelength λ_{21} excites the 1→2 transition and a second detector, with a different filter, measures fluorescence F_{20} in the 2→0 transition.

An alternative configuration has been implemented during the present work (Figure 4.1b): a single detector is used to collect fluorescence in the 2→1 transition for both excitation wavelengths. This simplifies the experimental set-up and removes a potential source of systematic error due to different detector efficiencies and filter transmissions. In the case of the two detector approach, a further problem would be the difficulty in ensuring that the two photomultipliers are imaging exactly the same measurement volume.

The relationship between the two fluorescence signals and the flame temperature is developed here for both of these two possible approaches. Similar derivations have been presented previously (Alkemade 1970; Dec and Keller 1986). The population dynamics are summarised in Figure 4.2.

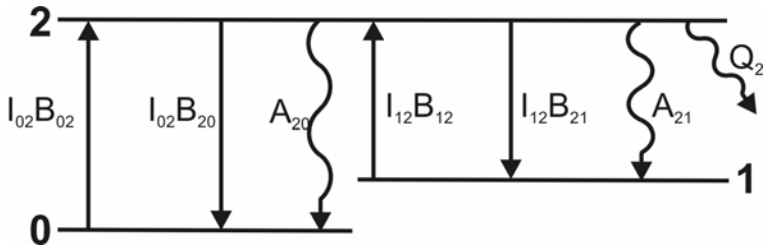

Figure 4.2. The population dynamics of a three-level electronic energy level system in an atom such as indium. Here, N_i is the number density of atoms residing in state i, A_{ji} is the transition probability for spontaneous emission, B_{ji} and B_{ij} are respectively the coefficients for stimulated emission and stimulated absorption, I_{ij} is the laser irradiance at the wavelength corresponding to transition $i \rightarrow j$, and Q_2 is the total rate of de-excitation from the upper state by collisional quenching or other non-radiative losses. The terms beside the arrows all have units of s^{-1}.

Note that the rates of thermal excitation to the upper state are considered to be negligible at flame temperature, and the rate of collisional redistribution between levels 0 and 1 is assumed to be high so that the populations are in equilibrium. When the transition $i \rightarrow 2$ is being excited (the symbol 'i' is used to denote either state 0 or state 1, depending on which transition is being

probed), a population balance can be used to express the rate of change in the population of the upper level. In steady-state, the following condition applies:

$$\frac{dN_2}{dt} = N_i I_{i2} B_{i2} - N_2 \left(I_{i2} B_{2i} + A_{20} + A_{21} + Q_2 \right) = 0 \tag{4.1}$$

The terms in this equation have been defined in Figure 4.1. Stimulated emission is negligible, due to the low population of the upper state, leading to:

$$N_2 = \frac{N_i I_{i2} B_{i2}}{A_{20} + A_{21} + Q_2} \tag{4.2}$$

The power of the fluorescence signal incident on the detector is given by:

$$F_{2j} = \left(\varepsilon_2 - \varepsilon_j \right) A_{2j} N_2 V \frac{\Omega}{4\pi} \tag{4.3}$$

Here, ε_2 - ε_i is the energy difference in J between the respective states, V is the volume of the measurement region, and Ω is the collection solid angle in steradians (i.e. $\Omega/4\pi$ represents the fraction of the total fluorescence that is collected by the optical set-up). The relationship between the coefficients for spontaneous emission and for stimulated excitation is (Demtröder 2003):

$$\frac{A_{nm}}{B_{mn}} = \frac{g_m}{g_n} \frac{8\pi h}{\lambda_{nm}^{\ 3}} \tag{4.4}$$

This allows the ratio of the fluorescence signals to be expressed as:

$$\frac{F_{20}}{F_{21}} = \frac{\left(\varepsilon_2 - \varepsilon_0\right) N_1 I_{12} A_{20} B_{12}}{\left(\varepsilon_2 - \varepsilon_1\right) N_0 I_{02} B_{02} A_{21}} \tag{4.5}$$

The size of the measurement volume, and the collection solid angle, are the same for each of the two excitation wavelengths so these terms cancel out. Note that the quenching coefficients also cancel out at this stage. This is an important advantage of TLAF over other thermometry techniques since the quenching coefficient is a function of composition and may be unknown. By substitution of Eqn. 4.4, this simplifies to:

$$\frac{F_{20}}{F_{21}} = \frac{N_1 g_0 I_{12} \lambda_{21}{}^4}{N_0 g_1 I_{02} \lambda_{20}{}^4} \tag{4.6}$$

From the Boltzmann equation (Eqn. 1.7), the temperature can be expressed as:

$$T = \frac{\Delta\varepsilon / k}{\ln\left(\frac{N_0 g_1}{N_1 g_0}\right)} \tag{4.7}$$

Here, the energy separation $\Delta\varepsilon$ is equal to ε_1- ε_0. By substitution of Eqn. 4.6, the final equation for temperature is:

$$T = \frac{\Delta\varepsilon / k}{\ln\left(\frac{F_{21}/I_{02}}{F_{20}/I_{12}}\right) + 4\ln\left(\frac{\lambda_{21}}{\lambda_{20}}\right) + C} \tag{4.8}$$

Here, C is introduced as an empirical calibration constant to take account of differences in the detector efficiencies and transmission characteristics of filters, and systematic errors in the laser power measurement.

A slightly different expression for temperature is required in the case of the single detector scheme shown in Figure 4.1b. Taking the ratio of the fluorescence signals:

$$\frac{F_a}{F_b} = \frac{N_0 I_{02} B_{02}}{N_1 I_{12} B_{12}} = \frac{g_1 N_0 I_{02} A_{20} \lambda_{20}^{\ 3}}{g_0 N_1 I_{12} A_{21} \lambda_{21}^{\ 3}} \tag{4.9}$$

By substitution into the Boltzmann expression, this yields:

$$T = \frac{\Delta\varepsilon / k}{\ln\left(\frac{F_a/I_{02}}{F_b/I_{12}}\right) + 3\ln\left(\frac{\lambda_{21}}{\lambda_{20}}\right) + \ln\left(\frac{A_{21}}{A_{20}}\right) + C} \tag{4.10}$$

In this scheme the empirical constant C only includes small corrections, for example for the calibration of the laser power detector efficiencies at λ_{20} and λ_{21}, which can be measured. Since the excitation/detection scheme is no longer symmetrical, the spontaneous emission coefficients, A_{20} and A_{21}, now appear in the expression for T. Since resonance fluorescence is observed for F_b, it should be noted that this technique is applicable only in open flames

with low particulate loading. The one-detector scheme could, however, be used to determine the calibration constant for the two-detector scheme, which could in turn be implemented in sooting flames.

As described in Chapter 3, the line-widths (< 8 MHz) of the diode laser excitation sources used are negligible compared to the transition widths of the transitions of atomic indium at flame conditions. This means that the terms F_a/I_{02} etc. can be accurately determined by evaluating the integral line-strength of the normalised fluorescence spectra.

In previous TLAF studies where broadband dye lasers were used as excitation sources, the lineshapes of the atomic transitions were not resolved (Dec and Keller 1986). Instead, it was assumed that the laser linewidth was much broader than the probed atomic transitions so that the spectral irradiance would be roughly constant over the entire transition. This assumption may not necessarily be valid since dye lasers with line widths of around 40 GHz were used (Dec and Keller 1986), and the widths of the indium transitions at 410.2 nm and 451.1 nm were shown in Chapter 3 to be around 25 GHz and 13 GHz, respectively, at flame conditions. Unknown spectral overlap between the dye laser profile and the atomic transitions could lead to inaccurate temperature measurements. In principle, this could be compensated for through the C coefficient, but fluctuations or drifts in the dye laser spectral profile would lead to unaccountable errors.

The above discussion has been general and not restricted to a particular atom, and the reasons for choosing a particular probe species will now be outlined. Possible candidates are Group III metals including gallium, indium, and thallium (Omenetto et al. 1972). The sensitivity of the measurement is derived from the sensitivity of the relative population to temperature. The

sensitivity of the technique is a function of the rate of change of $\frac{F_b/I_{12}}{F_a/I_{02}}$ with temperature which can be expressed as:

$$\begin{aligned}\frac{d\left(\frac{F_b/I_{12}}{F_a/I_{02}}\right)}{dT} &= \frac{d\left(\frac{g_0 N_1 A_{20}\lambda_{21}{}^3}{g_1 N_0 A_{21}\lambda_{20}{}^3}\right)}{dT} \\ &= \frac{A_{20}\lambda_{21}{}^3}{A_{21}\lambda_{20}{}^3}\frac{d\left(\exp\left(\frac{-\Delta\varepsilon}{kT}\right)\right)}{dT} \\ &= \frac{A_{20}\lambda_{21}{}^3}{A_{21}\lambda_{20}{}^3}\frac{\Delta\varepsilon}{kT^2}\exp\left(\frac{-\Delta\varepsilon}{kT}\right)\end{aligned} \tag{4.11}$$

This function has been evaluated over a range of temperatures for several Group III metals possessing a suitable three-level energy structure, including gallium, indium, and thallium. The relevant properties (NIST 2006) of the candidate species are listed in Table 4.1.

Element	level 1	level 2	level 3	$\Delta\varepsilon$	g_0	g_1	A_{20}	A_{21}	λ_{20}	λ_{21}
Gallium	$4^2P_{1/2}$	$4^2P_{3/2}$	$5^2S_{1/2}$	826	2	4	0.49	0.92	403.3	417.2
Indium	$5^2P_{1/2}$	$5^2P_{3/2}$	$6^2S_{1/2}$	2213	2	4	0.56	1.02	410.2	451.1
Thallium	$6^2P_{1/2}$	$6^2P_{3/2}$	$7^2S_{1/2}$	7793	2	2	0.63	0.71	377.6	535.0

Table 4.1. Properties of some Group III elements suitable for TLAF thermometry. Included are: the energy levels of the three-level system; the separation between the two lower levels (cm^{-1}); the degeneracies of the lower two levels; the spontaneous emission coefficients (10^8 s^{-1}); and the transition wavelength (nm).

The data from Table 4.1 were used to evaluate the function shown in Eqn. 4.11 for the three candidate species over a range of temperatures; the results are shown in Figure 4.3.

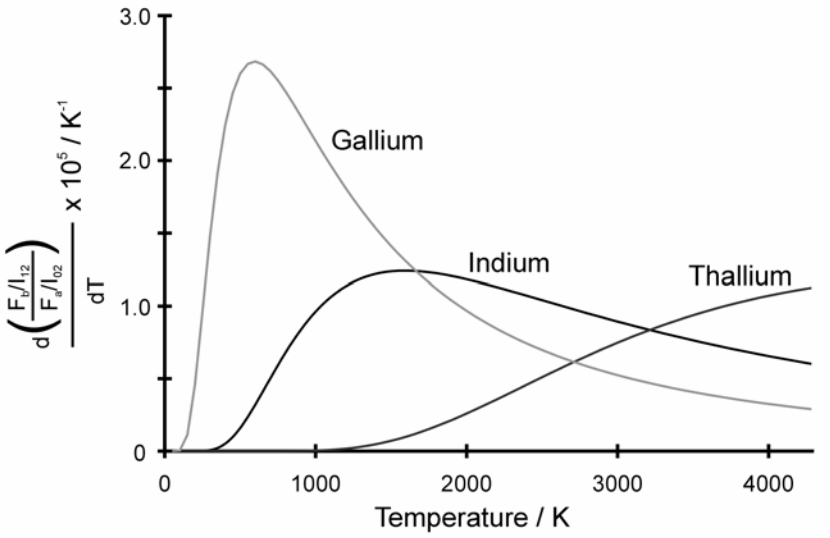

Figure 4.3. Sensitivity of fluorescence signal ratio to temperature for three possible probe species.

It is clear from the plot that the temperature of optimum sensitivity increases for elements with larger separation between the two lower energy states. Indium appears to give better sensitivity in the range of typical combustion temperatures between 1700 K – 2500 K so is likely to be preferable. It is necessary to consider the fact that, in principle, the derivative shown in Figure 4.3 could be high even for low fluorescence signal levels F_a and F_b, leading to large errors due to shot-noise. The transition probabilities are comparable for all the species listed in Table 4.1, but the low thermal population of the upper state of thallium means that the signal F_b would be relatively weak at flame temperature. The precise quantification of the expected LIF signals would, according to Eqns. 4.2 and 4.3, require knowledge of the quenching cross-

sections, which are not well-established for all of the species being considered.

Another factor in this decision relates to the chemical reactions of the probe species in the flame. When seeding the flame using a nebuliser the salt particles are volatilised by the high temperature at the flame front, so neutral atoms are present only in the post-flame region (Alkemade 1969). The concentration of seeded indium atoms decreases downstream of the flame-front due to the formation of the InOH. The rates of reaction of some metal atoms in flames have been investigated previously (Bulewicz and Sugden 1958) by a technique based on detection of thermally excited emission from the flame; it was found that gallium was more reactive than indium, while thallium was relatively inert. A stable probe species is desirable so that measurements can be made far from the flame front. One further important criterion, related to the chemical properties of the candidate species, is that thallium is extremely toxic to humans if inhaled, whereas indium and gallium are relatively non-toxic.

Blue diode lasers are available at wavelengths corresponding to the transitions listed in Table 4.1 for gallium, and were used to perform absorption spectroscopy of Ga atoms in a hollow-cathode lamp (Marago et al. 2003). No suitable diode laser source is available for the higher-wavelength transition of thallium at 535 nm. The indium transitions at 410.2 nm (Leinen et al. 2000; Hildebrandt et al. 2003; Hult et al. 2004) and at 451.1 nm (Burns et al. 2004) have also been probed using blue diode lasers.

Due to the combination of these reasons, indium was chosen as the probe species for use during this project. It has also been used in most previous TLAF studies (Joklik and Daily 1982; Dec and Keller 1986; Kaminski et al.

1998), although the first demonstrations of TLAF using flash-lamp excitation sources involved probing seeded thallium (Omenetto et al. 1972).

4.3 Experimental method for diode laser TLAF thermometry

Temperature measurements were performed in two different laminar flames of premixed methane and air. The first was an axis-symmetric Bunsen flame stabilised on a burner tube of diameter 10 mm and with equivalence ratio slightly greater than one. The second was the Mèker burner described in Chapter 3. In both cases, seeding of indium to the flame was performed using a nebulizer as outlined previously. The laser scanning and signal detection was done in precisely the same way as described in the Chapter 3, except that the laser beams had to be overlapped using a dichroic mirror before the focussing lens, as shown in Figure 4.4. In the case of the Mèker burner, a 500 μm diameter pin-hole was used as before, whereas for the measurements in the Bunsen flame, a smaller 150 mm pin-hole was employed, resulting in a probe volume of around $0.1\times0.1\times0.15$ mm^3. The laser power in the measurement volume was in the order of 0.5 mW for both beams.

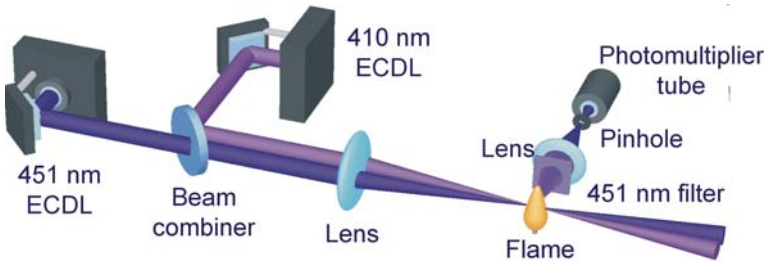

Figure 4.4. Optical set-up for two-line atomic fluorescence temperature measurements (the beams have been offset for clarity but are in reality well-overlapped).

The spectra were normalised by the simultaneously recorded laser power, and averages of 200 spectra were used for the evaluation of temperatures. Theoretical spectra were fitted to the averaged spectra using a non-linear least squares fitting routine, as described in Chapter 3. The fitting process was slightly different to the one used in Chapter 3: in the present case, the expected Doppler broadening was calculated for a temperature of 2000 K for all the measurements and specified in the fit. This avoided the need for *a priori* temperature information in the evaluation process. Since the Doppler broadening is much smaller than the pressure broadening, this would not introduce substantial errors. The fitted spectra were integrated to yield F_a/I_{02} and F_b/I_{12}, which were then used to evaluate temperatures according to Eqn. 4.10. The integration was performed over a range of frequencies extending beyond the limits of the experimental data (see Figures 3.3 and 3.4) so that the far wings of the spectra were included. No empirical calibration constant was employed. Measurements were performed in the Bunsen flame at a range of vertical positions on the central axis, and at a range of positions on a horizontal line extending outward from the central axis and passing through the flame front.

4.4 Results of temperature measurements in a laminar flame

Figure 4.5 shows vertical profiles of the 410 nm and 451 nm fluorescence signals along the central vertical axis of the flame, which were recorded by translating the burner with respect to the laser beam. At heights between 15.5 and 16 mm, significant increases in the indium LIF signals are observed, as the neutral indium atoms are generated close to the flame front by

volatilisation of the seeded $InCl_3$ salt particles. The fluorescence signals then decrease gradually with increasing height, due to the formation of indium hydroxide. The error bars shown correspond to the standard deviation of the integrated fluorescence powers obtained from single scans.

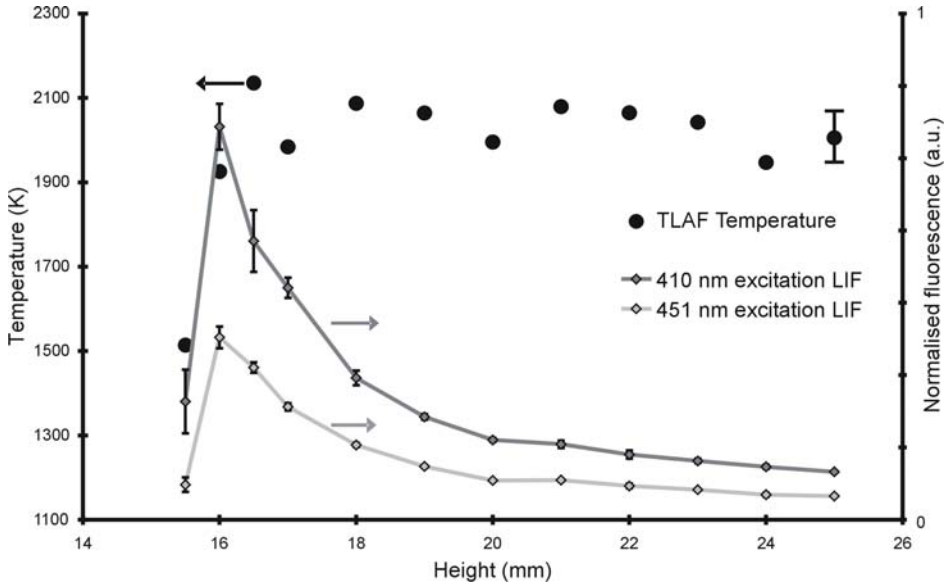

Fig 4.5 Temperature and laser induced fluorescence (LIF) signals along a vertical axis through the centre of a laminar Bunsen flame.

Observed signal variations are thought to stem from dynamic changes in indium concentration. This is substantiated by the fact that error bars are largest near the tip of the flame where the indium concentration is most strongly affected by minute flame flicker.

The temperature profile, also shown in Figure 4.5, was evaluated directly from averaged fluorescence powers using Eqn. 4.10. The excellent spatial resolution demonstrates the superiority of TLAF over conventional line-of-sight absorption techniques to perform temperature measurement in spatially inhomogeneous combustion environments. A steep rise in temperature is seen

near the flame front, with the temperature staying nearly constant in the post-flame region, in agreement with previous studies of CH_4/air Bunsen flames (Bennett et al. 1999). Temperatures in the post combustion region are seen to fluctuate slightly from one measurement point to the next (around 2.5%). This scatter is a consequence of minor drifts in local indium concentration and small flame movements due to currents of ambient air and flow speed variations, in addition to any measurement errors.

The largest systematic error in the temperature measurement arises from the laser power meter (OPHIR, PD200) used to calibrate the intensity measurements. The power meter consists of a photodiode that has been calibrated at 488 nm. The reading on the power meter is equal to the laser power multiplied by a factor that is read from a spectral response curve, supplied by the manufacturer. The error in estimating the ratio of the spectral responses at the two wavelengths is conservatively estimated to be 10%, which leads to an error (∂T) in the measured temperature that can be evaluated by taking the partial derivative of Eqn. 4.10 (Haraguchi et al. 1977):

$$\partial \ln\left(\frac{I_{12}}{I_{02}}\right) = -\frac{\Delta\varepsilon}{kT^2}\partial T \tag{4.12}$$

$$\frac{\partial T}{T} = -\frac{kT}{\Delta\varepsilon}\partial\left(\frac{I_{12}}{I_{02}}\right)\frac{I_{02}}{I_{12}} \tag{4.13}$$

This therefore translates into a systematic uncertainty of about 6%, or 120 K at 2000 K. Further systematic errors stem from the uncertainty in reported A coefficients of the two indium transitions, uncertainties in the frequency

calibration of laser scans, detector non-linearities and background flame emission, but these are all much less significant in the present case. The error bar shown at h=25 mm reflects the estimated total systematic uncertainty.

In Figure 4.6 a horizontal TLAF temperature profile is shown, obtained at a height of 10 mm above the burner. The zero position on the x-axis is underneath the flame-cone, on the centre-line of the axis-symmetric Bunsen flame. By displacing the burner horizontally, a set of temperature measurements at a range of radial location was obtained. Again a steep increase of the indium fluorescence signal is observed as the flame front is crossed, although the drop in signal is not as drastic as in the corresponding vertical profile in Figure 4.3. The temperature increase at the flame front is readily apparent; the maximum temperature is slightly lower along this profile compared to the maximum temperature of the vertical profile through the upper part of the flame, which is in agreement with previous findings (Bennett et al. 1999).

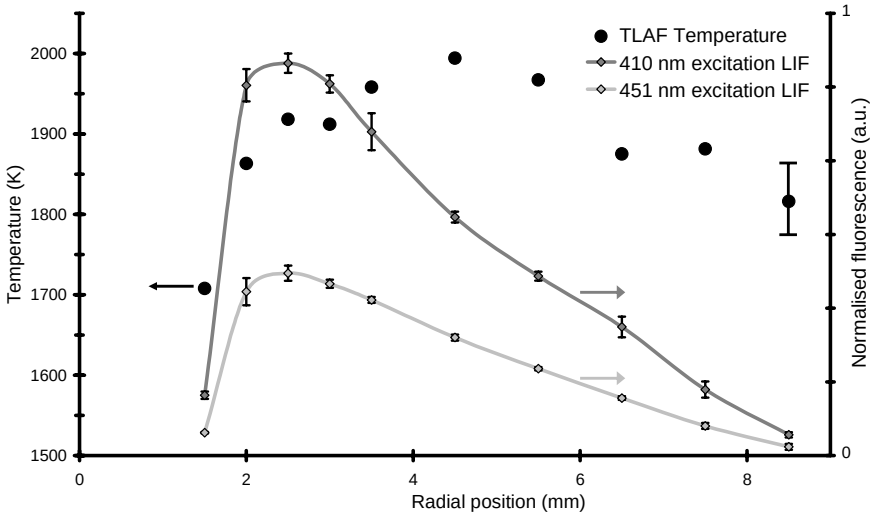

Figure 4.6. Temperature and TLAF signals along a horizontal axis through the centre of a laminar Bunsen flame.

An attempt was made to perform similar TLAF temperature measurements in the Mèker burner described in Chapter 3. This burner gives a very stable one-dimensional flame and has been characterised by reference temperature measurements performed by Mr G. Hartung, using the techniques of CARS and Na-line reversal. In principle, it should be directly possible to use the integrated area of the spectra shown in Chapter 3 to evaluate temperature. As it turns out, some of the resulting temperatures were significantly different to the values expected from the reference measurements. It is strongly suspected that this was the result of drifts in the seeded indium concentration since there was an interval of about a minute between the acquisition of the 410.2 nm and 451.1 nm spectra. This notion is substantiated by the fact that the temperatures calculated from the absorption signals show fair agreement with the TLAF temperatures: slow drifts in the seeding concentration between the two laser excitations would be expected to bias both these techniques in the same way. Such a problem will be avoided in future measurements by reducing the time between the two excitations.

This issue draws attention back to the non-negligible absorption of the laser beam that was reported in Chapter 3 in the case of the Mèker burner. While it is possible to compensate thoroughly for this in homogeneous environments, no such normalisation would be possible in dynamic combustion systems. It is desirable to evaluate the maximum tolerable absorption for such systems so that the highest possible seeding level may be employed, thus giving optimum LIF signals. To simplify the analysis, let us consider the case, to be discussed in Chapter 6, in which the laser beams are locked in wavelength near to the peaks of the respective transitions. A fast optical modulator could then be used to switch between the beams, thus avoiding the need to perform

wavelength tuning at high rates. The ratio between the fluorescence signals could then be related to the temperature by means of an empirical calibration constant. Any error in the ratio between the intensities of the two beams, due to absorption, would manifest itself as an error in the measured temperature via Eqn. 4.13. The fractional absorption of each beam depends on the number density but also on the 'apparent temperature'* of the gas mixture that the beam travels through before reaching the measurement volume.

For a range of values of fractional absorption of the 410.2 nm laser, the absorbance was calculated by means of Eqn. 3.7. This was then used to calculate the absorbance for the 451.1 nm laser via:

$$Absorbance_{12} = Absorbance_{02} \frac{N_1}{N_0} \frac{\tilde{\sigma}_{12}}{\tilde{\sigma}_{02}} \frac{A_{Ref\text{-}13}}{H_{Ref\text{-}13}} \frac{H_{Ref\text{-}23}}{A_{Ref\text{-}23}} \qquad (4.14)$$

Here, reference spectra (the ones shown in Figures 3.5 and 3.6) have been used for each transition to find the ratio between peak absorbance ($H_{Ref\text{-}ij}$) and integrated absorbance ($A_{Ref\text{-}ij}$). The weak temperature dependence of this ratio has been ignored in this analysis. The frequency integrated absorption cross-section, $\tilde{\sigma}_{ij}$, has been defined in Chapter 3. The population ratio N_1/N_2 was evaluated at a range of temperatures using the Boltzmann equation.

The absorption of the 451.1 nm beam then allows the error in the intensity ratio to be evaluated:

* The difference between the apparent and real temperature in two-line laser absorption thermometry of non-homogeneous systems has been described in Chapter 1.

$$\left(\frac{I_{02}}{I_{12}}\right)_{Error} = \left(\frac{1-Absorption_{02}}{1-Absorption_{12}}\right) - 1 \qquad (4.15)$$

This can, in turn, be used to evaluate the temperature error using the partial derivative in Eqn. 4.13. The results of this analysis are shown in Figure 4.7 for an assumed absorption of 10% for the 410.2 nm laser.

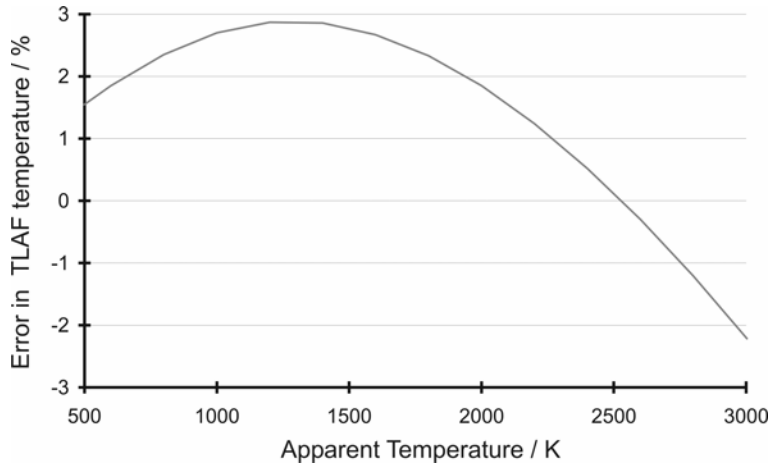

Figure 4.7. The error in measured TLAF temperature in the case of 10% absorption of the 410.2 nm laser beam by indium in the flame. The apparent temperature refers to what would be estimated by a two-line indium absorption measurement.

It is thus demonstrated that even for a fairly strong attenuation of 10 % in the laser intensity, the resulting error in temperature would be less than 3% for any apparent temperature below 3000 K. This could be a useful means of maximising the LIF signal intensity for future high temporal resolution measurements.

4.5 Potential for application in dynamic environments

It will be remembered that one of the projected applications of the diode laser temperature sensor being developed here is to make measurements in turbulent flames, where the fast dynamics of the system require a temporal resolution on the order of at least 10 kHz. It is consequently essential to make an estimate as to whether the proposed technique might reasonably be expected to achieve this. As the measurement time is reduced, the dominant source of noise in the fluorescence spectrum will be shot noise, resulting from the probabilistic nature of the photocathode emission process and of the photon arrival statistics at the detector. The resulting signal-to-noise ratio (SNR) is defined as (Eckbreth 1996):

$$SNR = \frac{F_{2j}}{\sigma_{F_{2j}}} = \sqrt{\eta N_F \tau} \qquad (4.16)$$

Here, $\sigma_{F_{2j}}$ is the root-mean-square fluctuation in the fluorescence signal, η is the quantum efficiency of the photomultiplier tube (i.e. the fraction of the incident photons that would cause the emission of an electron from the photocathode), N_F is the rate of arrival of photons at the detector, and τ is the measurement time.

The spectra shown in Chapter 3 that were recorded in the Mèker burner will be used as the basis for this analysis. The fluorescence signal was recorded during the experiment as a voltage, but the properties of the photomultiplier tube (Hamamatsu, R3877) and the pre-amplifier (Hamamatsu, C7319), summarised in Table 4.2, can be used to calculate the collected radiant power.

Photomultiplier:	
Voltage supply	906 V
Cathode Radiant Power	4.58×10^5 A/W
Quantum Efficiency (η)	0.3
Preamplifier:	
Gain	10^5 V/A
Bandwidth	20 kHz

Table 4.2. Characteristics of the LIF signal detection system.

An analysis has been made based on the raw data shown in Figures 3.3 and 3.4. In the case of the 410.1 nm laser, the peak fluorescence signal was 8V at a laser power of 1 mW. Using the values shown in Table 4.2, we calculate that this corresponds to an optical power of 0.58 nW or 1.2×10^9 photons/s incident on the detector. The peak laser absorption for this particular 410.2 nm spectrum was 10%, so this corresponds to the maximum permissible seeding level as mentioned in the preceding section. Naturally, this maximum seeding concentration applies only to measurements for which the beam has travelled through 20 mm of the seeded region before reaching the measurement volume as was the case for measurements of the central vertical axis of the Mèker burner. It would thus be possible to use higher concentrations of indium atoms in narrower test objects, or when making measurements near to the periphery of wide objects. As mentioned in Chapter 3, the spatial resolution defined by the pin-hole used for the spectra taken in the Mèker burner was 500 μm. Similarly, the peak signal for the 451.1 nm laser was approximately 3V at a laser power of 0.9 mW, corresponding to 0.22 nW or 0.49×10^9 photons per second.

Let us suppose that the rapid measurement is to be done in the way described in the discussion on laser absorption, and that the laser wavelengths can be locked at the peaks of the respective indium transitions. A required temporal resolution of 10 kHz (measurement time 100 μs) will be assumed; an interval should be included, during which both lasers are blocked, so that the background radiation intensity may be measured. The signal acquisition time for each laser may therefore be around τ = 30 μs. By use of Eqn 4.16, the shot noise is thus estimated to be:

$$\frac{F_a}{\sigma_{F_a}} = 100 \qquad \frac{F_b}{\sigma_{F_b}} = 65 \tag{4.17}$$

These values can be converted into an error in the measured temperature by again taking the partial derivative of Eqn. 4.10:

$$\frac{\partial T}{T} = -\frac{kT}{\Delta\varepsilon}\frac{\partial F_a}{F_a} \qquad \frac{\partial T}{T} = \frac{kT}{\Delta\varepsilon}\frac{\partial F_b}{F_b} \tag{4.18}$$

The magnitudes of these errors can be added in the following way by assuming that they are random and uncorrelated:

$$\frac{\sigma_T}{T} = \frac{kT}{\Delta\varepsilon}\left[\left(\frac{\sigma_{F_a}}{F_a}\right)^2 + \left(\frac{\sigma_{F_b}}{F_b}\right)^2\right]^{1/2} \tag{4.19}$$

This leads to an estimated temperature precision of 1.5%. It is thus shown that LIF thermometry with high temporal resolution (10 kHz) and high spatial resolution (500 μm) is possible with the blue diode lasers used during this project. This leads to substantial possibility for further development of the TLAF thermometry technique that was discussed and demonstrated in this Chapter. Subsequently, Chapter 6 will describe a strategy to achieve high speed TLAF thermometry by developing a simple method for laser locking to molecular resonance lines.

4.6 References

Alkemade, C. T. J. (1969). Fundamental aspects of decomposition, atomization, and excitation of the sample in the flame. Flame Emission & Atomic Absorption Spectrometry, Vol 1. J. A. Dean and T. C. Rains. New York, Marcel Dekker.

Alkemade, C. T. J. (1970). "A theoretical discussion on some aspects of atomic fluorescence spectroscopy in flames." Pure and Applied Chemistry **23**: 79-98.

Bennett, B. A. V., J. Fielding, R. J. Mauro, M. B. Long and M. D. Smooke (1999). "A comparison of the structures of lean and rich axisymmetric laminar Bunsen flames: application of local rectangular refinement solution-adaptive gridding." Combustion Theory and Modelling **3**: 657-687.

Bulewicz, E. M. and T. M. Sugden (1958). "Determination of the dissociation constants and heats of formation of molecules by flame photometry. Part 4 - The stability of GaOH, InOH, TlH." Transactions of the Faraday Society **426**: 830-837.

Burns, I. S., J. Hult and C. F. Kaminski (2004). "Spectroscopic use of a novel blue diode laser in a wavelength region around 450 nm." Applied Physics B-Lasers And Optics **79**: 491-495.

Dec, J. E. and J. O. Keller (1986). "High-Speed Thermometry Using Two-Line Atomic Fluorescence." Proceedings of the Combustion Institute **21**: 1737-1745.

Demtröder, W. (2003). Laser Spectroscopy. Berlin, Springer-Verlag.

Eckbreth, A. C. (1996). Laser Diagnostics for Combustion Temperature and Species. Amsterdam, Gordon and Breach.

Engstrom, J., J. Nygren, M. Alden and C. F. Kaminski (2000). "Two-line atomic fluorescence as a temperature probe for highly sooting flames." Optics Letters **25**: 1469-1471.

Haraguchi, H., B. Smith, S. Weeks, D. J. Johnson and J. D. Winefordner (1977). "Measurement of Small Volume Flame Temperatures by 2-Line Atomic Fluorescence Method." Applied Spectroscopy **31**: 156-163.

Hildebrandt, L., R. Knispel, S. Stry, J. R. Sacher and F. Schael (2003). "Antireflection-coated blue GaN laser diodes in an external cavity and Doppler-free indium absorption spectroscopy." Applied Optics **42**: 2110-2118.

Hult, J., I. S. Burns and C. F. Kaminski (2004). "Measurements of the indium hyperfine structure in an atmospheric-pressure flame by use of diode-laser-induced fluorescence." Optics Letters **29**: 827-829.

Joklik, R. G. and J. W. Daily (1982). "2-Line Atomic Fluorescence Temperature-Measurement in Flames - an Experimental-Study." Applied Optics **21**: 4158-4162.

Kaminski, C. F., J. Engström and M. Aldén (1998). "Quasi-Instantaneous Two-Dimensional Temperature Measurements in a Spark Ignition Engine Using Two-Line Atomic Fluorescence." Proceedings of the Combustion Institute **27**: 85-93.

Leinen, H., D. Glassner, H. Metcalf, R. Wynands, D. Haubrich and D. Meschede (2000). "GaN blue diode lasers: a spectroscopist's view." Applied Physics B-Lasers and Optics **70**: 567-571.

Marago, O. M., B. Fazio, P. G. Gucciardi and E. Arimondo (2003). "Atomic gallium laser spectroscopy with violet/blue diode lasers." Applied Physics B-Lasers and Optics **77**: 809-815.

NIST (2006). NIST Atomic Spectra Database.
http://physics.nist.gov/cgi-bin/AtData/lines_form

Omenetto, N., P. Benetti and G. Rossi (1972). "Flame Temperature Measurements by Means of Atomic Fluorescence Spectrometry." Spectrochimica Acta Part B-Atomic Spectroscopy **B 27**: 453-&.

Zizak, G., N. Omenetto and J. D. Winefordner (1984). "Laser-excited atomic fluorescence techniques for temperature measurements in flames: a summary." Optical Engineering **23**: 749-755.

Chapter 5

A thermometry technique based on atomic line-shapes using diode laser LIF in flames

5.1 Introduction

This Chapter reports on the development of a novel flame thermometry technique using a single extended-cavity diode laser (ECDL). The temperature is deduced from the fluorescence line-shapes of seeded indium atoms. The technique, which we call OLAF (one-line atomic fluorescence), is simple to implement, and has excellent spatial resolution. Temperatures are deduced from the $5^2P_{1/2} \rightarrow 6^2S_{1/2}$ transition of atomic indium, the line-shape of which was discovered to be highly sensitive to temperature changes at typical flame conditions. A rigorous validation was carried out in a stable one-dimensional flame with comparisons to accurate reference measurements and numerical simulations.

The importance of spatially-resolved temperature measurements to the study of combustion is widely acknowledged and was discussed in Chapter 1, where the numerous benefits of using laser diagnostics to perform such

measurements were also presented. It was pointed out that the complexity and cost of the equipment required to perform such thermometry techniques, based on solid-state lasers and dye lasers, restricts their use to dedicated laboratory environments. One of the trends that was highlighted in Chapter 1 was increasing use of diode laser sensors to perform measurements in combustion systems, both for research purposes and for on-line monitoring (Allen 1998). Such sensors have the advantages of being compact, inexpensive and robust. The application of such sensors, however, has been almost exclusively restricted to path-integrated absorption measurements, offering little or no information on spatial gradients. Thermometry is possible by wavelength scanning a near infra-red diode laser over a carefully selected pair of temperature sensitive absorption lines of a species such as H_2O (Arroyo and Hanson 1993; Zhou et al. 2005), O_2 (Sanders et al. 2001), or OH (Aizawa 2001). This and related techniques are appropriate for the study of systems in which the temperature is homogeneous along the beam path but, as described in Chapter 1, in environments where there are significant temperature inhomogeneities, this type of measurement does not predict the correct average temperature, because the absorbance is a non-linear function of temperature. In most flames and combustors, however, there are substantial temperature gradients, and a diode-laser-based diagnostic that is capable of spatially resolved measurements would therefore be of significant value.

A diode laser technique based on two-line atomic fluorescence (TLAF) of seeded indium was described in Chapter 4 and high-spatial-resolution temperature measurements were demonstrated (Hult et al. 2005a). Due to the high oscillator strengths of atoms, strong fluorescence signals were obtained

even when probed with low power diode laser excitation sources. Despite the potential and advantages of this approach, one disadvantage is that two laser sources are required. A single-laser approach would simplify the measurement still further.

During this research, it was discovered, however, that the indium fluorescence line-shapes appeared to be sensitively dependent on temperature. The $5^2P_{1/2} \rightarrow 6^2S_{1/2}$ transition at around 410.2 nm has especially good sensitivity as a result of the separation of the hyperfine components; the reason for this will be discussed in more detail in Section 5.2 below. This could therefore be used to develop a technique for spatially resolved temperature measurements requiring only a single diode laser. Instead of probing the relative intensity of two transitions, it involves probing only one transition, and obtaining temperature information from the spectral line-shape. The acronym 'OLAF' (one-line atomic fluorescence) is coined for this new approach, to distinguish it from the conventional TLAF technique.

It should be noted that line-shape-based temperature measurements have been used in the past in *low pressure* environments because, under these conditions, collisional broadening is negligible and the transition width is determined solely by Doppler broadening, whose temperature dependence is described by a simple relationship. For example, Scheibner et al. (Scheibner et al. 2002) used the line-width of absorption spectra of aluminium atoms, acquired using a blue extended cavity diode laser, to determine the temperature in a hollow-cathode lamp, as a function of discharge current. Similar experiments have been performed on hollow cathode lamps of gallium (Marago et al. 2003), and of copper (Laurila et al. 2005). Temperature measurements have also been made in a low pressure DC-arc

plasma jet reactor, used for diamond chemical vapour deposition by monitoring the Doppler broadened line-shape of acetylene (Wills et al. 2003); this was done by using a near infra-red ECDL to perform cavity-ring down spectroscopy.

At the conditions of an atmospheric pressure flame, however, the situation is more complicated because the line-shape is a convolution of the Doppler profile with a Lorentzian profile, which results from collisional broadening. The Lorentzian width ($\Delta\nu_L$) has a complex dependence on temperature, and is also a function of chemical composition, which in typical combustion situations may not be known. The sensitivity of $\Delta\nu_L$ to temperature and flame composition is explored in this chapter, and this new contribution leads to the possibility of a substantially simpler thermometry technique.

Path-averaged flame thermometry based on line-shape analysis has been attempted previously by Sanders et al (Sanders et al. 2002a; Sanders et al. 2002b), who seeded caesium atoms to a pulse-detonation engine. They derived an empirical value for an exponential coefficient relating the width of the Lorentzian part of the absorbance line-profile ($\Delta\nu_L$) to temperature, and thus obtained good agreement with the reference measurements of the temporal evolution of temperature in the engine. However, $\Delta\nu_L$ is also dependent on the mole-fractions of colliding species (which may vary spatially and temporally). In estimating the relationship between $\Delta\nu_L$ and temperature, it is consequently important to avoid making a calibration which inadvertently takes into account the effects of the different gas compositions that may exist. In the case of the work by Sanders et al (Sanders et al. 2002a; Sanders et al. 2002b), this point may have been overlooked. They propose a seemingly unreasonable value for the exponential coefficient for the

relationship of $\Delta\nu_L$ with T; this coefficient seems implicitly to take account of widely varying H_2O concentrations (change in mole fraction from 0.25 to 0.45) between the different measurement points; the H_2O concentrations in their pulse-detonation engine became particularly elevated because the oxidant was pure O_2. It is known that H_2O can be anomalous as a broadening partner due, in part, to short-lived hydrogen bonding with the probed atom (Nefedov et al. 1999). In the work of Sanders et al. (Sanders et al. 2002a; Sanders et al. 2002b), the relationship between H_2O concentration and temperature in the particular combustion device and at the particular conditions of reactant composition etc, was thus 'baked into' the empirical coefficient. The validity of this empirical relationship between $\Delta\nu_L$ with T was not tested under another set of experimental conditions.

By contrast, for the LIF technique that is proposed here, the dependence of $\Delta\nu_L$ on T and on species concentration is explored explicitly using model assumptions that are physically reasonable for the flame conditions that are probed. The experiments presented here involve combustion in air; therefore, there is a high mole fraction of N_2 at all locations, and the variation in species mole fractions between different spatial locations is less significant.

This chapter begins by briefly outlining the relevant theory of collisional line-broadening, and by drawing attention to the particular advantage of indium as a probe species. This is followed by a description of the experimental set-up required to perform OLAF. Finally, results from measurements performed in a laminar reference flame are presented and the accuracy of the technique is assessed by comparison to CARS, to Na-line reversal, and to numerical simulation performed for identical conditions by another author. The results

are discussed before concluding with an overview of the future prospects for the technique.

5.2 Theory of line-broadening thermometry

The broadening of spectral lines has already been addressed in Chapter 3, but will be examined in greater detail here by considering the functional dependence of $\Delta\nu_L$ on temperature and on species concentration. As we have seen already (Eqn. 3.1), one broadening mechanism is known as Doppler broadening, and the Doppler width can be easily calculated for a particular species at a given temperature (Eqn. 3.2). At atmospheric-pressure flame conditions, a further broadening resulting from collisional (or pressure) broadening, is of comparable magnitude. The spectral shape of the pressure broadening contribution to the line-shape can be approximated by a Lorentzian function, as we have seen from Eqn 3.3. It was also explained in Chapter 3 that the composite spectral shape that results from these effects is described by the convolution of the Doppler and Lorentzian functions, which results in the Voigt profile:

$$g(\nu) = \frac{2}{\Delta\nu_D}\sqrt{\frac{\ln 2}{\pi}}\left(\frac{a}{\pi}\int_{-\infty}^{\infty}\frac{e^{-y^2}}{a^2+(x-y)^2}dy\right). \tag{5.1}$$

Here, the variables a and x are defined as:

$$x = 2\sqrt{\ln 2}\,\frac{(\nu-\nu_0)}{\Delta\nu_D}. \tag{5.2}$$

$$a = \sqrt{\ln 2}\,\frac{\Delta\nu_L}{\Delta\nu_D} \tag{5.3}$$

It was shown in Chapter 3 that for broadening of indium atoms at flame conditions, the Doppler width and Lorentzian width are of comparable magnitude (e.g. for the 410.2 nm transition, $\Delta\nu_L \cong 5.0$ GHz; $\Delta\nu_D \cong 2.3$ GHz) and the Voigt profile provided a good fit to the experimental data. We must therefore consider both Doppler broadening and collisional broadening in attempting to relate the spectral shape to temperature.

As noted above, the functional relationship between $\Delta\nu_L$ and T is fairly complicated. Nevertheless, an approximate analysis can be made on the basis of certain assumptions. Since, at flame conditions, natural broadening (which was described in Chapter 3) is negligible compared to collisional broadening, the total Lorentzian width can be expressed as the sum of that resulting from adiabatic collisions ($\Delta\nu_{L''}$) and that resulting from non-adiabatic collisions ($\Delta\nu_{L'}$) (Nefedov et al. 1999). The distinction between these is that non-adiabatic collisions result in a change in the energy state of the atom, whereas adiabatic collisions do not. The magnitude of $\Delta\nu_{L'}$ for atoms cannot easily be estimated from theory, but, at flame conditions, is typically an order of magnitude smaller than $\Delta\nu_{L''}$ (Nefedov et al. 1999); therefore, in this analysis, the former will be neglected. A further assumption that can be made is the impact broadening approximation (Sobelman et al. 1981), by which it is supposed that the duration of collisions between the atom and the broadening partner is insignificant by comparison to the time between collisions. This assumption is valid at the conditions being probed here, and only breaks down at much higher pressure. The radiation that occurs during collisions can thus

be neglected, and the collisions can be regarded as instantaneous. It follows that the only consequence of the collisions is in a phase shift to the emitted radiation. The magnitude of this phase shift depends on the interaction potential between the probed atom and perturbing molecule, which can be approximated by the first term of the van der Waals function (Nefedov et al. 1999):

$$V_{vdw}(R)=\frac{C_6}{R^6} \tag{5.4}$$

From these assumptions, it can be shown (Sobelman et al. 1981) that the Lorentzian width is described by:

$$\Delta v_L \propto \Delta C_6^{\frac{2}{5}} u^{\frac{3}{5}} N . \tag{5.5}$$

Here, N is the total number density, C_6 is related to the van der Waals interaction potential, and u is the relative mean velocity between the probed atoms and perturbing molecules,

$$u=\sqrt{\frac{8RT}{\pi \mu}} . \tag{5.6}$$

Here, μ is the reduced mass. Nefedov et al (Nefedov et al. 1999) describe a method for estimating the C_6 interaction potential, from which it is apparent that this term is not a function of temperature. If we assume ideal gas

behaviour, then $N \propto T^{-1}$, from which it follows that: $\Delta v_L \propto T^{-0.7}$, and this is the relationship that will be used throughout this chapter. It should be noted that $\Delta\nu_L$ is a function of composition, through its dependence on u and on ΔC_6. Nevertheless, since the flames in this study are composed mainly of N_2, this dependence will be neglected; the validity of this assumption will be discussed in a later section.

Another aspect of theoretical background that it is worthwhile to consider is the reason for selecting indium as the tracer species. In order to reveal the rationale behind this choice, it is instructive to consider the variation in the spectral shape of the indium $5^2P_{1/2} \rightarrow 6^2S_{1/2}$ transition (near 410.2 nm) as a function of temperature. The transition consists of four hyperfine components, the middle two of which lie close to each other, resulting, at flame conditions, in a structure with three separate peaks. Examples of theoretical spectra are shown in Figure 5.1: each one represents the sum of four Voigt profiles. The positions and relative intensities of the hyperfine components of the transition are also shown (Hult et al. 2005a). In Figure 5.1, a base case spectrum has been plotted with Lorentzian width equal to that measured at 2200 K in a stoichiometric flame of methane and air (corresponding to the temperature obtained from a reference measurement, as will be described in a later section); the Doppler width was calculated for the same temperature. Another spectrum is also shown, corresponding to a temperature of 1850 K; in this case, $\Delta\nu_L$ and $\Delta\nu_D$ were calculated from the relationships shown above. The spectra have each been normalised to a maximum value of 1.0 arbitrary units. Note that in the latter case, the depths of the troughs in the spectrum are less profound.

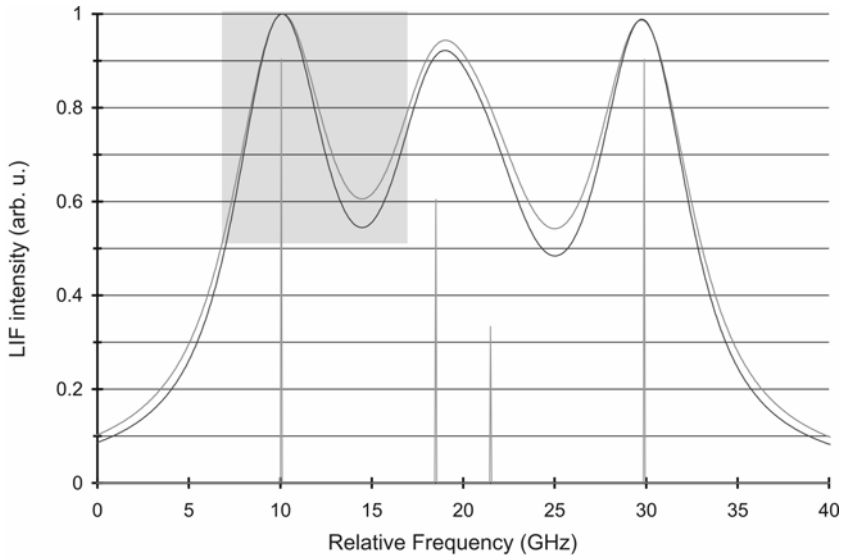

Figure 5.1 Simulated indium spectra corresponding to temperatures of 1850 K (shallower troughs) and of 2200K. The positions of the hyperfine lines are indicated.

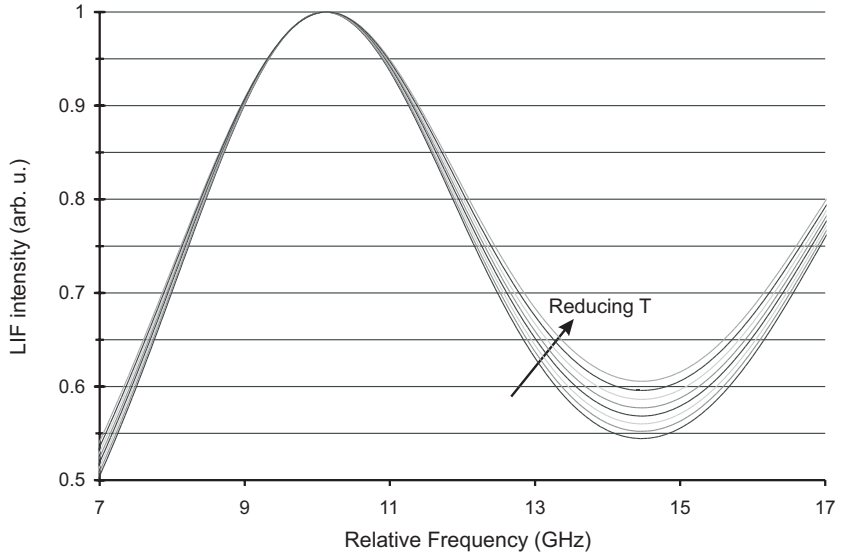

Figure 5.2 The shaded region of Figure 5.1, shown on an expanded scale, and additional spectra are shown at 50 K intervals, ranging from 1850 K to 2200 K.

An expanded view of the shaded region in Figure 5.1 is shown in Figure 5.2, where six further spectra are shown, separated by intervals of 50 K. It is apparent from the figure that the depth of the trough in the spectrum is very sensitive to temperature. That is to say that the ratio between the heights of the leftmost peak and the adjacent trough ('peak-to-trough ratio') changes substantially with temperature at flame conditions. This effect is shown over a wider range of temperatures in Figure 5.3, where the relative change in the peak-to-trough ratio as a function temperature is plotted together with the relative change in the overall width (FWHM) of the $5^2P_{1/2} \rightarrow 6^2S_{1/2}$ transition system. Note that what is displayed in Figure 5.3 is not the width of an individual hyperfine component but the overall width of the spectral feature shown in Figure 5.1.

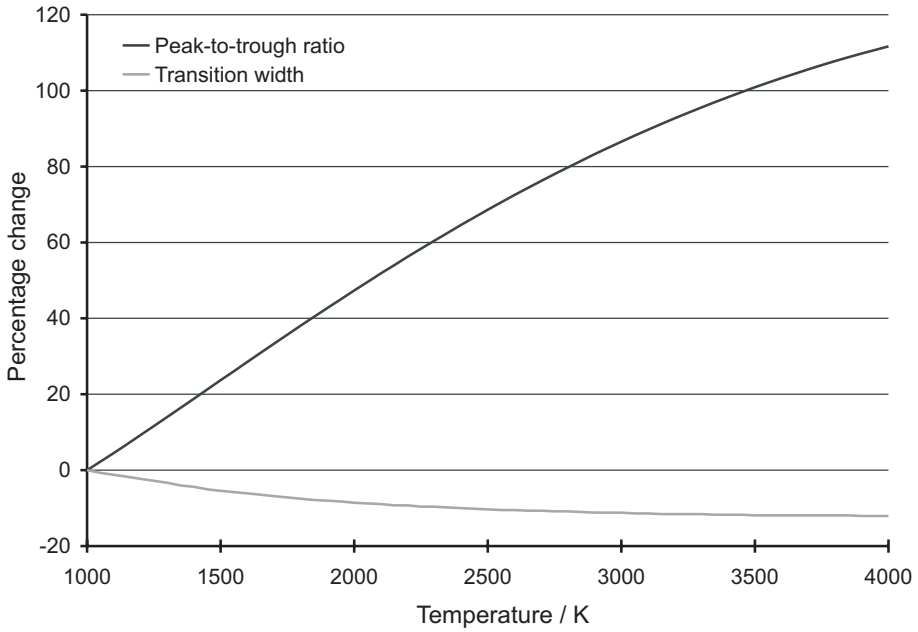

Figure 5.3 The percentage change in the peak-to-trough ratio, and in the composite width (FWHM) of the $5^2P_{1/2} \rightarrow 6^2S_{1/2}$ transition system, as a function of temperature.

It is clear that the composite transition width shows little sensitivity to temperature change, especially at more elevated temperatures, where the increasing Doppler width compensates for the falling Lorentzian width to result in no overall change. By contrast, a substantial change in the spectral shape is apparent from the large variation in the peak-to-trough ratio. The contrast is that the lower line in Figure 5.3 refers to changes in the *spectral width* of the transition, whereas the upper line describes changes in the relative *intensity* between two points on the spectrum. Therefore, the choice of a transition system with several appropriately spaced hyperfine lines allows for greater temperature sensitivity than would be possible with a single hyperfine line, where the location of the line flanks would need to be determined very accurately. The fidelity of the indium LIF spectra obtained during this study, and the corresponding quality of the spectral fits (see Figure 5.5) mean that the technique is sensitive even to small changes around typical flame temperatures.

5.3 Experimental method

It will have become apparent that the experimental set-up for the line-width-based temperature measurements is very similar to the one described in Chapter 3, when the spectroscopy of atomic indium was being investigated. Therefore, only a brief description of the method is given here.

The widely tunable extended cavity diode laser, operating around 410 nm, which was used during this work, has been described in detail in Chapter 2 and elsewhere (Hult et al. 2005b). Due to the wide mode-hop free tuning range of this laser system, it was possible to perform mode hop-free scanning over the entire $5^2P_{1/2} \rightarrow 6^2S_{1/2}$ transition structure. Spectra of this indium

transition have already been presented in Chapter 3, and their use together with fluorescence spectra of the $5^2P_{3/2} \rightarrow 6^2S_{1/2}$ transition of indium (near 451.1 nm) to determine two-line temperatures has been addressed in Chapter 4. The laser wavelength scans were performed at a rate of 20 Hz, and the laser power varied between approximately 1.4 mW to 0.8 mW during the scan, due to tuning of the injection current. The experimental set-up for the thermometry experiment is shown in Figure 5.4. The main difference from the set-up for the TLAF experiments described in Chapter 4 is that, in this case, only one extended cavity diode laser is required. The substantial difference from the forgoing chapter is not in the experimental method, but in the way in which the data are analysed.

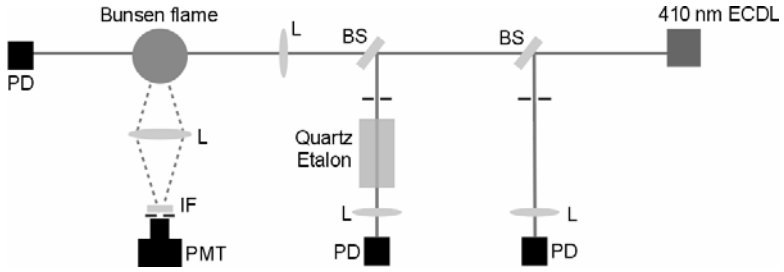

Figure 5.4 The experimental set-up for the OLAF thermometry experiments (L: lens; IF: interference filter centred around 451.1 nm; PMT: photomultiplier tube; PD: photodiode; BS: beamsplitter; ECDL: extended cavity diode laser)

The output beam of the extended cavity diode laser was focussed (f = 300 mm) to a beam diameter of around 100 μm on the central axis of the flame. The burner was mounted on a translation stage which allowed for the adjustment of its height. Prior to passing through the flame, part of the laser beam was reflected by a glass plate towards a quartz etalon (FSR = 3.02 GHz); the transmitted fringe pattern of this etalon was used to ensure that the laser scans were mode-hop free, and also made it possible to compensate for

slight non-linearities in the wavelength scanning rate. A second glass plate was used to reflect part of the laser beam to a photodiode as a reference power measurement, which was used to normalise the fluorescence intensity. Another photodiode was used to measure the power of the laser beam after the flame. This allowed the absorbance spectrum to be evaluated, and thus to be used to compensate the LIF spectra for attenuation of the laser beam prior to the measurement volume. The fluorescence signal was imaged at $f^{\#} = 2.4$ through a pin-hole (d = 500 μm) and an interference filter centred around 451.1 nm (CVI, $\Delta\lambda$ = 3 nm) onto a photomultiplier tube (Hamamatsu, R3788); the photomultiplier signal was pre-amplified (Gain = 10^5; bandwidth = 20 kHz). This resulted in a measurement volume defined by a cylinder with a diameter of 0.1 mm and length of 0.5 mm. The detection of non-resonant fluorescence in the $5^2P_{3/2} \rightarrow 6^2S_{1/2}$ transition, at around 451.1 nm, avoided any interference that could otherwise have resulted from scattered laser light from the surface of the burner plate. The electronic signals were digitised using an oscilloscope, and the averages of 128 individual wavelength scans were stored. Measurements of the background readings were taken and were subtracted from the experimental data. It has previously been confirmed that the values of laser irradiance such as that used here are well within the linear excitation regime (Hult et al. 2005a).

The line-shape thermometry experiments were performed in a one-dimensional laminar flame of CH_4 and air, stabilised on the Mèker burner described in Chapter 3. Seeding of indium atoms was done by passing a portion of the air stream through a nebuliser containing an aqueous solution of $InCl_3$ (~0.05 M), which resulted in a concentration of indium atoms in the flame of approximately 100 ppb. The unseeded co-flow flame (d=60 mm)

which was run at the same stoichiometry as the inner seeded flame (d=40 mm), which meant that the seeded region was homogeneous in temperature, thus allowing accurate path-integrated temperature measurements to be performed by the Na-line reversal technique, for the purpose of comparison. Reference temperature measurements were made, at precisely the same flow conditions, by Na-line reversal, and by vibrational coherent anti-Stokes Raman scattering (CARS) of N_2. The characterisation of the Mèker burner by CARS, Na-line reversal, and numerical simulation were performed by Mr G. Hartung of the Laser Analytics Group, and are presented here solely for the purpose of comparison to the diode laser LIF measurements.

Due to the long path length and flat flame front of the burner used during these experiments, there was non-negligible absorption of the laser beam by atomic indium as it passed through the flame (typically around 10%); absorbance spectra have been presented in Chapter 3. This could be thoroughly compensated for, however, because of the homogeneity of the flame, which meant that the laser power at the measurement volume could be determined. Signal trapping did not influence the line-shape of the acquired spectra since these experiments involved an excitation scan and broadband detection. Spectra were taken at a range of stoichiometries at 12 mm height above burner (HAB), and at a range of heights above the burner for $\phi = 1.0$.

Theoretical spectra comprising the sum of four Voigt profiles were fitted to the experimental data for each of the flames conditions studied. In the case of both the ϕ scan and the height scan, the point at $\phi = 1.0$ and HAB = 12 mm was used as a calibration point. For these points, $\Delta\nu_D$ was fixed to the temperature that was measured at the same conditions by the Na-line reversal method. The relative spectral positions and relative intensities of the four

hyperfine lines are well-known (Hult et al. 2005a). The four fitted parameters were: the spectral location and intensity of the leftmost hyperfine component, $\Delta\nu_L$, and the background. The calibration therefore allowed a relationship to be developed for $\Delta\nu_L$ at other temperatures:

$$\Delta v_L = \Delta v_L^{ref} \left(\frac{T^{ref}}{T} \right)^{0.7} \qquad (5.7)$$

Thus for the rest of the measurements, T was a fitted parameter and $\Delta\nu_D$ and $\Delta\nu_L$ were related to T by Eqn. 5.1 and by Eqn. 5.7, respectively. The resulting temperature data are presented and discussed in the following section.

5.4 Results and discussion

Figure 5.5 shows an example of a fluorescence spectrum with a fitted spectrum superimposed. It is clear from the small residual that there is a very close agreement between the theoretical spectrum and the experimental data. For this reason, the fitted spectra allow an accurate evaluation of the Lorentzian width of the transitions.

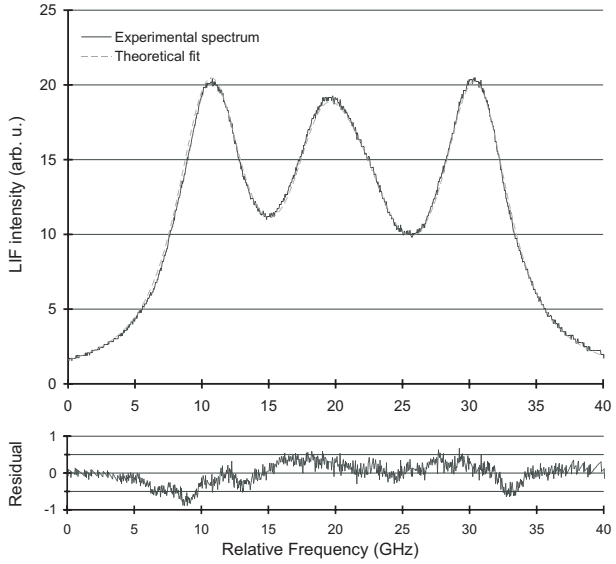

Figure 5.5 The average of 128 indium fluorescence spectra is shown along with a theoretical fitted spectrum. The residual between the experimental and fitted spectra is shown on a separate axis.

Figures 5.6 and 5.7 show the results of the stoichiometry scan in the flat-flame burner. Firstly, Figure 5.6 shows the measured temperature (T_{line}) as a function of ϕ at HAB = 12 mm. The results of reference measurements performed with Na-line reversal (T_{Na}), and of numerical calculations using PREMIX (Kee et al. 1993), are also shown as a comparison. It can be seen that there is good agreement between the results of the two experimental techniques. There is agreement between T_{line} and T_{Na} to within 6% at all stoichiometries, and the model results also concur with the experimental data.

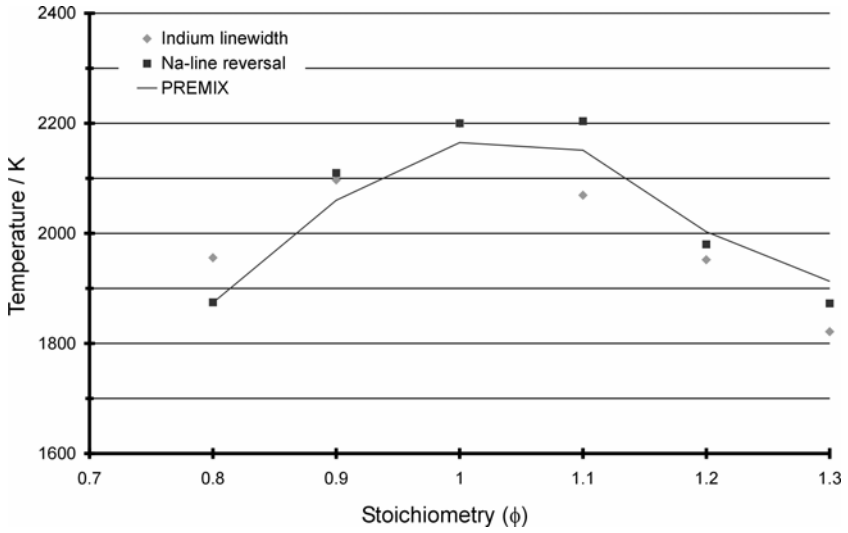

Figure 5.6 Measured flame temperatures at 12 mm HAB as a function of ϕ. The line-width temperature at ϕ = 1.0 was fixed to the value measured by Na-line reversal, and the temperatures for the other points were calculated from Eqn. 5.7. Temperatures measured by Na-line reversal in the same burner are shown for comparison.

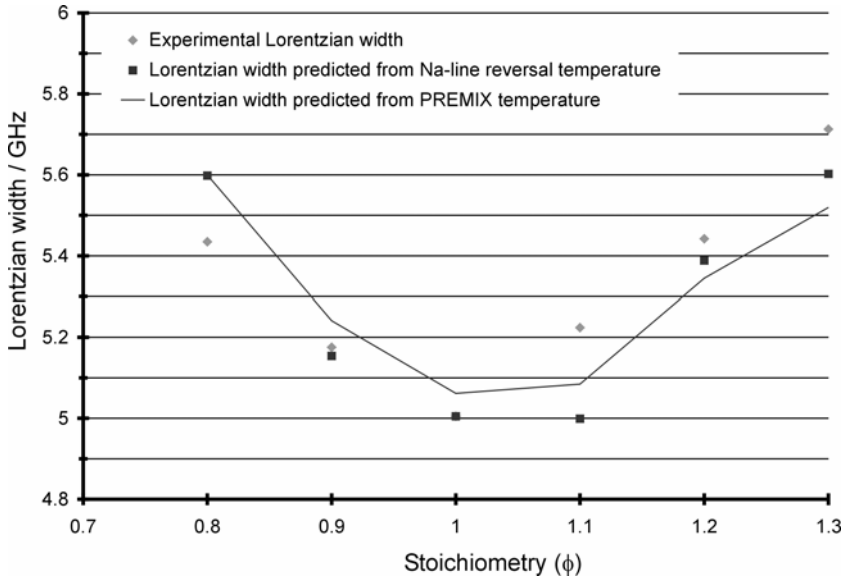

Figure 5.7 Fitted Lorentzian widths as a function of ϕ, and Lorentzian widths predicted from the Na-line reversal temperature measurements at the same conditions.

Figure 5.7 shows the relationship of the fitted Lorentzian widths to ϕ. The value of $\Delta\nu_L$ that would be expected from T_{Na}, using Eqn. 5.7, is also shown. This plot reveals that the model for temperature dependence of $\Delta\nu_L$ does not give perfect agreement with the experimental data. This may result from a combination of several factors: the true exponent describing the relationship between $\Delta\nu_L$ and T differs from the estimated value of 0.7. This could result from the influence of non-adiabatic collisions, or from adiabatic collisions that are not well-described by the impact approximation and the use of the C_6 potential. Alternatively, the dependence of $\Delta\nu_L$ on T may be correctly described by the exponential coefficient of 0.7, but there may be a weak influence of composition on $\Delta\nu_L$. For adiabatic collisions with molecules described by the C_6 potential, $\Delta\nu_L$ is directly proportional to the polarizability, α, of the colliding partner (Nefedov et al. 1999), and is related through Eqn. 5.5 to the relative mean velocity. It is thus possible to estimate the expected variation in $\Delta\nu_L$ over the stoichiometry range studied here (ϕ=0.8-1.3). The major species compositions at 12 mm HAB for ϕ=1.0 were calculated using PREMIX (Kee et al. 1993) and are shown in Figure 5.8. These data were used along with available polarizability data (Lide (Ed) 1996) to calculate the percentage change in $\Delta\nu_L$ that would be expected for the range of stoichiometries being considered. Interestingly, it was noticed that the influence of the variation of the relative mean velocity, u, was the dominant effect. It is clear from Figure 5.8 that the maximum expected percentage change in $\Delta\nu_L$ over this range of ϕ would be 0.6%. This would translate into a systematic error in evaluated temperatures of around 15 K.

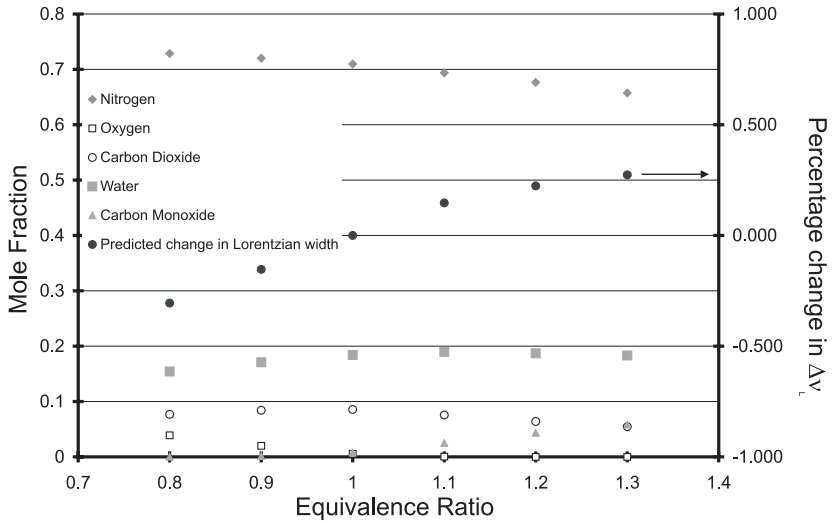

Figure 5.8 Calculated mole fractions at 12 mm above the burner for a range of equivalence ratios. The corresponding percentage change in pressure broadening is shown on a separate axis.

Since the species that differs most from N_2 in its properties as a broadening partner is H_2O, it is anticipated that any such effects of composition on $\Delta\nu_L$ would probably be somewhat less significant for other types of hydrocarbon-air flames: for hydrocarbon fuels other than methane, the C:H ratio is higher so the mole fraction of H_2O in the product gases would be lower. Similarly, in turbulent flames in which ambient air is entrained in the flow, the mole fraction of N_2 increases, thereby reducing the influence of composition on $\Delta\nu_L$. Despite this, it is also possible that a significant part of the deviation between T_{line} and T_{Na} may simply be caused by stochastic scatter of the data resulting from an error in the estimation of $\Delta\nu_L$ from the experimental spectra. It is interesting to note that the data point in Figure 5.6 with the largest deviation between T_{line} and T_{Na} corresponds to a stoichiometry of 1.1. There is no systematic increase in the error as the composition departs further from

the conditions at ϕ =1.0, where the calibration was made. Furthermore, the reference measurements are also subject to experimental error: in particular, the temperature T_{Na} for ϕ = 1.1 seems unreasonably high. Another source of error is that the indium line-shape and Na-line reversal measurements were not performed simultaneously, so there is an uncertainty in reproducing the gas flow rates to the burner.

Such scatter is clearly evident in Figure 5.9, which shows the results of a height scan in the flame. There is very little composition change as a function of HAB, and the temperature gradient is only significant close to the surface of the burner plate. The temperature was measured by Na-line reversal only at HAB = 12 mm. Therefore, the results of CARS temperature measurements performed at the same conditions, and of a model performed using the PREMIX code (Kee et al. 1993), are also shown in Figure 5.9.

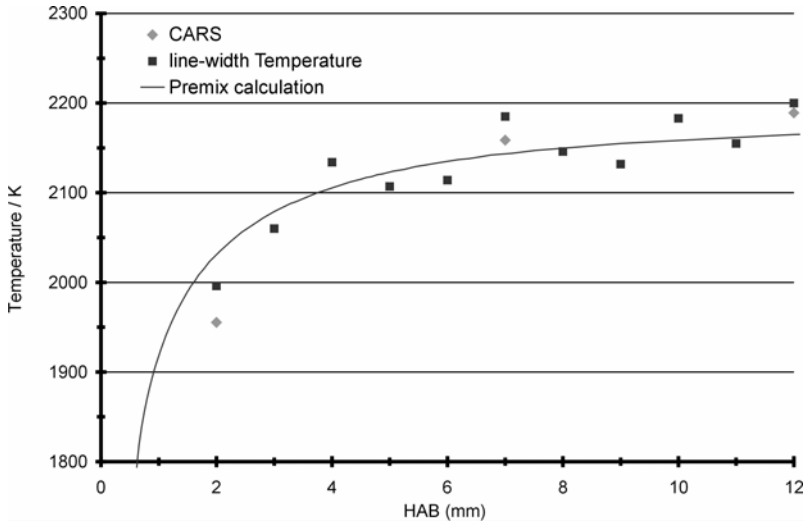

Figure 5.9 Measured temperature as a function of height above burner (HAB) for stoichiometry ϕ = 1.0. The line-width temperature scale is locked to the value measured by Na-line reversal at HAB = 12 mm. Temperature measurements by CARS, and the results of calculations from the PREMIX code, are also shown.

The CARS measurements represent averages of temperatures obtained by theoretical fits (using the CARSFT code (Palmer 1989)) to 600 individual experimental spectra with an associated accuracy of ±40 K. It is clear that the line-width measurements correctly follow the trend in fairly sharp temperature increase in the region just above the flame front, which results from the slow exothermic reaction of CO to form CO_2. This is followed by a gentle increase above about HAB = 4 mm. By comparing T_{line} to the model results, it is evident that the T_{line} data are scattered by approximately ±40 K around the mean, which can only be attributed to random error.

The measurements reported here represent the first spatially resolved measurements of flame temperature using a single diode laser. Any future development would be directed toward the possibility of much faster measurements, since thermometry in dynamic systems requires both high temporal and spatial resolution. It might be envisaged that future ECDL designs that would allow substantially quicker mode-hop free tuning to be performed, might do so at the expense of tuning range. Therefore, a method of analysing the line-shape of a small segment of the spectrum to determine $\Delta\nu_L$, and thus T, would be of substantial interest. One way to do this would be to rapidly sweep the laser over only the spectral region shown in the expanded-scale graph in Figure 5.2. The ratio of the LIF intensity at the peak to that in the trough has a sensitive dependence on temperature and could be used as the basis for a future high-speed sensor.

5.5 Conclusions

This Chapter has described the development of a novel flame temperature measurement technique based on the analysis of the line-shapes of

fluorescence spectra of atomic indium. The spectra were generated using a single diode laser and this technique therefore offers the advantage of greater simplicity by comparison to multi-laser diagnostics, while retaining favourable aspects such as spatial resolution and accuracy. Atomic indium was chosen as the probe species due to the sensitivity of the spectral shape to temperature at flame conditions. A theoretical model was employed to describe the relationship of T with $\Delta\nu_L$, instead of forcing the predicted temperature to agree with the reference measurements by introducing an empirical calibration constant. The measurements of temperature by the single-diode laser OLAF technique have been carefully compared to accurate reference measurements in a stable one-dimensional flame that was stabilised on a burner allowing seeding of metal atoms. The OLAF results show good agreement with the expected temperatures but reasons for small discrepancies have been highlighted. It is accurate, inexpensive, and simple to implement, and, combined with independent pressure measurements, has the potential even for measurements in environments where the pressure fluctuates. Faster laser-scanning rates would allow the study of dynamic flame behaviour, and lead to the possibility of performing sensitive temperature measurements by the analysis of a small, temperature sensitive, portion of the full fluorescence spectrum.

5.6 References

Aizawa, T. (2001). "Diode-laser wavelength modulation absorption spectroscopy for quantitative *in situ* measurements of temperature and OH radical concentration in combustion gases." Applied Optics **40**: 4894-4903.

Allen, M. G. (1998). "Diode laser absorption sensors for gas-dynamic and combustion flows." Measurement Science & Technology **9**: 542-562.

Arroyo, M. P. and R. K. Hanson (1993). "Absorption measurements of water-vapor concentration, temperature, and line-shape parameters using a tunable InGaAsP diode laser." Applied Optics **32**(30): 6104-6116.

Hult, J., I. S. Burns and C. F. Kaminski (2005a). "Two-line atomic fluorescence flame thermometry using diode lasers." Proceedings of the Combustion Institute **30**: 1535-1543.

Hult, J., I. S. Burns and C. F. Kaminski (2005b). "Wide-bandwidth mode-hop-free tuning of extended-cavity GaN diode lasers " Applied Optics **44**: 3675-3685.

Kee, R. J., J. F. Grcar, M. D. Smooke and J. A. Miller (1993). A FORTRAN program for modelling steady laminar one-dimensional premixed flames, Sandia National Laboratories.

Laurila, T., R. Oikari and R. Hernberg (2005). "Tunable diode laser spectrocopy of copper, cadmium, and indium at 325 nm." Spectrochimica Acta, Part B: Atomic Spectroscopy **60**: 783-791.

Lide (Ed), D. R. (1996). CRC Handbook of Chemistry and Physics. Boca Raton, USA, CRC Press.

Marago, O. M., B. Fazio, P. G. Gucciardi and E. Arimondo (2003). "Atomic gallium laser spectroscopy with violet/blue diode lasers." Applied Physics B-Lasers and Optics **77**(8): 809-815.

Nefedov, A. P., V. A. Sinel'shchikov and A. D. Usachev (1999). "Collisional broadening of the Na-D lines by molecular gases." Physica Scripta **59**(6): 432-442.

Palmer, R. E. (1989). The CARSFT computer code for calculating coherent anti-Stokes Raman spectra: user and programmer information, Sandia National Laboratories.

Sanders, S. T., D. W. Mattison, J. B. Jeffries and R. K. Hanson (2002a). "Sensors for High-Pressure, Harsh Combustion Environments using Wavelength-Agile Diode Lasers." Proceedings of the Combustion Institute **29**: 2661-2667.

Sanders, S. T., D. W. Mattison, L. Ma, J. B. Jeffries and R. K. Hanson (2002b). "Wavelength-agile diode-laser sensing strategies for monitoring gas properties in optically harsh fows: application in cesium-seeded pulse detonation engine." Optics Express **10**: 505-513.

Sanders, S. T., J. Wang, J. B. Jeffries and R. K. Hanson (2001). "Diode-laser absorption sensor for line-of-sight gas temperature distributions." Applied Optics **40**(24): 4404-4415.

Scheibner, H., S. Franke, S. Solyman, J. F. Behnke, C. Wilke and A. Dinklage (2002). "Laser absorption spectroscopy with a blue diode laser in an aluminum hollow cathode discharge." Review of Scientific Instruments **73**(2): 378-382.

Sobelman, I. I., L. A. Vainshtein and E. A. Yukov (1981). Excitation of Atoms and Broadening of Spectral Lines. Berlin, Springer-Verlag.

Wills, J. B., M. N. R. Ashfold, A. J. Orr-Ewing, Y. A. Mankelevich and N. V. Suetin (2003). "Number density and temperature of acetylene in hot-filament and arc-jet activated CH_4/H_2 gas mixtures measured using diode laser cavity ring-down absorption spectroscopy." Diamond and Related Materials **12**: 1346-1356.

Zhou, X., J. B. Jeffries and R. K. Hanson (2005). "Development of a fast sensor for combustion gases using a single tunable diode laser." Applied Physics B **81**: 711-722.

Chapter 6

High-resolution spectroscopy of $^{130}Te_2$ and active frequency-locking of a diode laser to a molecular resonance line

6.1 Introduction

This Chapter presents a second strategy directed toward high temporal-resolution flame temperature measurements using the novel diode-laser TLAF technique. The proposed scheme is based on rapidly switching between the two laser beams whose wavelengths are fixed near the centres of the respective indium transitions. This has the advantage that each laser is always at full power, and well-overlapped with the indium transition, thus maximising the signal-to-noise ratio. The increasing impact of shot-noise at faster measurement rates has already been referred to in Chapter 4.

A simple approach will be demonstrated here to stabilise actively the wavelengths of the two extended-cavity diode lasers by monitoring absorption of the laser light by molecular tellurium in a heated cell. The two ECDLs described previously were used to perform high-resolution spectroscopy of

$^{130}Te_2$ which was found to have closely-spaced absorption lines overlapping with the indium transitions at around 410.2 nm and 451.1 nm. It was thus shown that $^{130}Te_2$ absorption lines suitable for referencing purposes in gas sensing applications exist below the lower limit (417 nm) of the spectral region covered by the tellurium atlas (Cariou and Luc 1980). This leads to the possibility of locking the laser wavelengths to remain on resonance with the indium lines. Such locking has been successfully demonstrated for the 410 nm ECDL by implementing a straightforward feedback control loop. The laser emission was stabilised to within a frequency range of 40 MHz (Burns et al. 2006), which is negligible in comparison to the width of the indium transitions at atmospheric pressure. The absolute spectral positions of the $^{130}Te_2$ lines were estimated by comparison to a simultaneously acquired fluorescence spectrum of atomic indium, and, in the case of the scan around 410 nm, were identified by comparison to literature data.

Previous studies have investigated the use of advanced techniques to lock the wavelength of extended-cavity diode lasers with very high precision (Hayasaka 2002; Park and Yoon 2003). Such systems are developed for use in fundamental atomic physics experiments that are conducted at low pressure. By contrast, industrial and environmental gas sensing applications are typically performed at atmospheric pressure (Hult et al. 2005), giving rise to much higher transition widths. Therefore, the upper limit of the laser frequency fluctuations that can be tolerated in such applications is much greater. It is nonetheless important to avoid any long-term drifts in the laser wavelength, which may result from the influence of changes in the ambient temperature or pressure on the extended cavity length. The straightforward

method presented here for stabilising the emission wavelength of ECDLs is thus expected to find application in gas-sensing experiments.

Diatomic molecules of species such as tellurium and iodine are frequently used for referencing the frequency scale of a laser scan, or for locking the wavelength of a laser source because they have a dense spectrum of strong absorption lines. While the iodine spectrum extends from 500 nm to 675 nm (Gerstenkorn and Luc 1978), the strong tellurium lines occur in the region 385 nm to 523 nm (Barrow and du Parcq 1972). An atlas tabulating the positions of the strong lines in the spectrum of the tellurium isotope $^{130}Te_2$ is available (Cariou and Luc 1980), covering the wavelength region above 417 nm. Absorption lines of Te_2 have been used to reference the frequency scale of spectral scans, in the region covered by the atlas (Cariou and Luc 1980), in numerous experimental studies; some examples of this have involved the use of blue dye lasers (Cacciani et al. 1995; Kaminski et al. 1997; Hori et al. 2003). Spectroscopy of Te_2 has been performed with a near-infrared diode laser, which was frequency doubled to 493 nm (Raab et al. 1998). The $^{130}Te_2$ molecule has also been used to lock the wavelength of visible lines of Ar^+ lasers (Cancio and Bermejo 1997).

The first section of this Chapter gives a brief overview of the background theory of molecular energy levels, which is required to understand the spectra that will be shown. A description of the experimental method is then given, and is followed by a presentation and discussion of the results, addressing the $^{130}Te_2$ absorption spectra followed by the laser locking experiment.

6.2 Molecular spectroscopy background

6.2.1 Underlying principles

As was mentioned in Chapter 3, the spectra of molecules are much more complicated than those of atoms due to the influence of the vibration of the covalent bonds, and the angular momentum associated with molecular rotation. Due to the limitations of space, only an abbreviated summary of the relevant aspects is given here. During this overview, the underlying reason for the choice of molecular tellurium for the purpose of frequency-locking a blue laser will become evident.

The effects of molecular rotation will be considered first. A diatomic molecule such as Te_2 can be considered to have two rotational degrees of freedom since the moment of inertia around the axis of the bond is very low; the moments of inertia (I) around the two axes perpendicular to the bond are virtually identical. In many cases, it is reasonable to approximate the diatomic molecule as a rigid rotator, although in reality the bond length increases for faster rotation due to centrifugal distortion. This leads to the following equation (Banwell 1994) for the potential (in cm^{-1}) of the J'th rotational sub-level above that of the rotational ground state ε_0:

$$\varepsilon_j = BJ(J+1) - DJ^2(J+1)^2 \qquad (6.1)$$

Here, J is the rotational quantum number (J=0,1,2,…), D is the centrifugal distortion constant, which compensates for the fact that the real molecule is not a rigid rotator, and B (cm^{-1}) is the rotational constant, defined as:

$$B = \frac{h}{8\pi^2 Ic} \tag{6.2}$$

In Eqn. 6.2, h is Planck's constant and I is given by:

$$I = \mu r_0^2 \tag{6.3}$$

Here, r_0 represents the bond length (286 pm), and μ the reduced mass. Pure rotational transitions correspond to the absorption or emission of electromagnetic radiation in the microwave region of the spectrum; the selection rule governing such transitions is $\Delta J=\pm 1$. Interaction with electromagnetic radiation can, however, only occur for heteronuclear molecules because there is no dipole component change during the rotation of homonuclear molecules (Banwell 1994). As a consequence of this, the rotational structure of homonuclear molecules such as $^{130}Te_2$ can only be investigated spectroscopically by probing transitions in which there is also a change in the electronic energy level.

Vibrations of the covalent bond are another source of internal energy in molecules. The vibration results from the elasticity of the bond, which allows the position of the bound molecules to oscillate around their mean locations. The potential energy of the system as a function of internuclear distance is described empirically by the Morse function (Banwell 1994), which leads to the following equation for the energies of the vibrational states:

$$\varepsilon_v = \omega_e \left[1 - x_e\left(v + \frac{1}{2}\right)\right]\left(v + \frac{1}{2}\right) \tag{6.4}$$

Here, ω_e is an oscillation frequency and x_e is an 'anharmonicity constant', which is always small and positive. The selection rule for vibrational transitions is $\Delta\nu$ = ±1, ±2, ±3…, but the transition probability decreases rapidly with increasing $\Delta\nu$ and transitions with $\Delta\nu$ = ±3 typically have negligible intensity. It follows from Eqn. 6.4 that the energy change for an absorption from ν=0→ ν=1 is: $\Delta\varepsilon = \bar{\omega}_e(1-2x_e)$, while for ν=0→ ν=2, the energy change is: $\Delta\varepsilon = 2\bar{\omega}_e(1-3x_e)$. Since x_e is small, the energy change in the latter case is roughly double that of the former. Therefore, the ν=0→ ν=1 transition is referred to as a fundamental absorption, whereas the ν=0→ ν=2 transition is referred to as the first harmonic overtone. Vibrational transitions of molecules correspond to the absorption or emission of radiation in the infra-red spectral region. As was the case for molecular rotations, the molecule can only interact with light if the vibration involves a change in the dipole moment of the molecule. Therefore, homonuclear diatomic molecules can be probed neither by pure rotational spectroscopy nor by pure vibrational spectroscopy. To perform spectroscopy of such molecules, electronic transitions can instead be studied.

In general, transitions of molecules from one electronic state to another tend to correspond to the emission of light in the UV-visible spectral range. Electronic transitions can be probed spectroscopically in all molecules since changes in the electronic configuration of the molecule always lead to a change in the dipole moment. For molecules in general, the lowest electronic energy states is denoted by the letter *X*, and the next levels are called *A*, *B*, *C*, etc (Eckbreth 1996). The electronic states of molecules are categorised

according to the quantum number (Λ) describing the axial component of the total orbital angular momentum (Herzberg 1950). These types of state are denoted by the term symbols Σ, Π, Δ, Φ, etc., for $\Lambda = 0, 1, 2, 3$, etc.

Vibrational and rotational transitions may occur together with the electronic transitions; therefore, each electronic transition consists of a large number of individual lines. The total energy change can, by the Born-Oppenheimer approximation, be written as (Banwell 1994):

$$\Delta\varepsilon_{total} = \Delta\varepsilon_{electronic} + \Delta\varepsilon_{vibrational} + \Delta\varepsilon_{rotational} \qquad (6.5)$$

The rotational transitions that may occur together with changes in the electronic energy state are governed by the general selection rule ΔJ= -1,0,1. These three situations are denoted respectively as the *P*, *Q*, and *R* branches. If however, $\Lambda = 0$ in both electronic states of the transition, then $\Delta J = 0$ is forbidden and there is no Q branch.

An electronic transition may be accompanied by transitions between any vibrational states, but absorption transitions originating in the lowest vibrational level are strongest since that level is most highly populated. The intensity of molecular absorption lines is also affected by the Franck-Condon principle, which states that, during the electronic transition, there is unlikely to be a substantial change in the internuclear separation or of the molecular velocity (Herzberg 1950). An example of this situation is given in Figure 6.1, in which two electronic energy levels are shown. The electronic potential is plotted for each level as a function of internuclear separation; the minimum of this function corresponds to the bond length. The wavefunctions (ψ) for

selected vibrational levels are also shown. The internuclear separation for a particular vibrational level is described by a probability density function which is equal to ψ^2. The consequence of the Franck-Condon principle is that the transition corresponds to a vertical line on Figure 6.1.

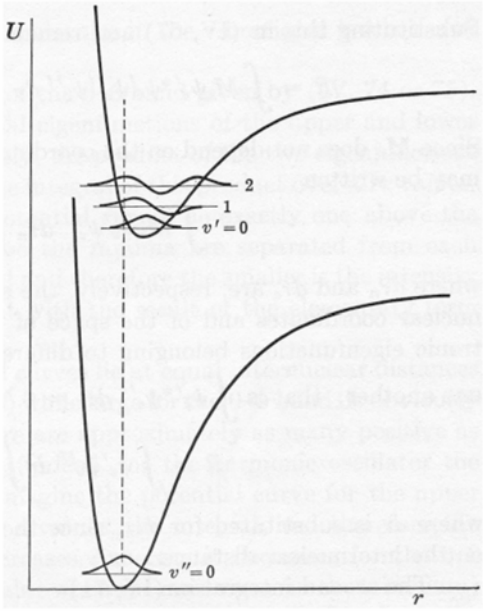

Figure 6.1. Franck-Condon principle for electronic-vibration transitions. The potential curves for two electronic states and the wavefunctions for selected vibrational levels are shown. For the internuclear separation depicted here, the best overlap of the wavefunctions occurs for $v' = 2$, $v'' = 0$. This diagram has been taken from Herzberg (Herzberg 1950)

The pairs of levels for which the maximum of ψ^2 occurs at the same internuclear separation are thus 'well-overlapped', and these transitions have highest probability. Having briefly addressed the general basis of molecular spectra, some further details will now be given concerning the spectra of molecular tellurium, which was studied during the present work.

6.2.2 Spectroscopy of molecular tellurium

Diatomic molecules of species such as tellurium and iodine exhibit a dense spectrum of strong absorption lines resulting from the rotational fine structure of electronic-vibration transitions; this is because their high reduced mass (μ) gives rise to a low rotational constant (B) of 0.032 cm^{-1}, according to Eqn. 6.2. This leads to close rotational line spacing and causes a large number of rotational energy levels to be significantly populated. This is part of the reason why the tellurium was chosen for the purpose of laser-locking: there was a high probability that strong absorption lines would be found overlapping with the spectrum of each of the two indium transitions being probed. Several natural isotopes of tellurium exist in abundant quantities and this leads to especially large numbers of lines being present in the spectrum of naturally occurring Te_2. It is interesting to note that it was not until isotopically purified tellurium samples such as $^{130}Te_2$ and $^{128}Te_2$ became available that it was possible to interpret the visible band spectrum of the molecule (Barrow and du Parcq 1972).

The three relevant electronic energy states of the $^{130}Te_2$ molecule are depicted in Figure 6.2, which also shows the potentials of selected vibrational levels. These electronic states have been classified as being $X0_g^+$, $A0_u^+$, and $B0_u^+$ (du Parcq and Barrow 1966; Jha et al. 1969; Barrow and du Parcq 1972). This nomenclature is required because Hund's case (c) (Herzberg 1950) must be used to describe the behaviour of these states (Jha et al. 1969). This added complexity is a result of the high molecular mass, and entails the splitting of X, which would otherwise be a $^3\Sigma_g^-$ state, into 0_g^+ and 1_g states, of $B^3\Sigma_u^-$ into 0_u^+ and 1_u states, and of $A^3\Pi_u$ into 0_u^+ and 1_u states. These states are,

however, analogous to Σ states in that transitions between them have $\Delta J = \pm 1$; thus the Q-branch is absent. It has been reported that at wavelengths between 400.0 nm to 411.5 nm, there is a $v'' = 0$ progression in the $X0_g^+ \rightarrow B0_u^+$ transition (Barrow and du Parcq 1972), whereas at wavelengths longer than 425 nm, the spectrum becomes increasingly complicated due to the appearance of the $v'' = 0$ progression in the $X0_g^+ \rightarrow A0_u^+$ transition. Absorption only occurs in Te_2 from lower states having an even value of the rotational quantum number J'', which according to (Jha et al. 1969) is characteristic in a Σ-Σ type transition of some molecules having zero nuclear spin. The values of potential energy shown on the right-hand axis of Figure 6.2 correspond to transitions in the blue-violet spectral region, and this is another reason for the suitability of Te_2 for use in wavelength stabilisation of GaN diode lasers.

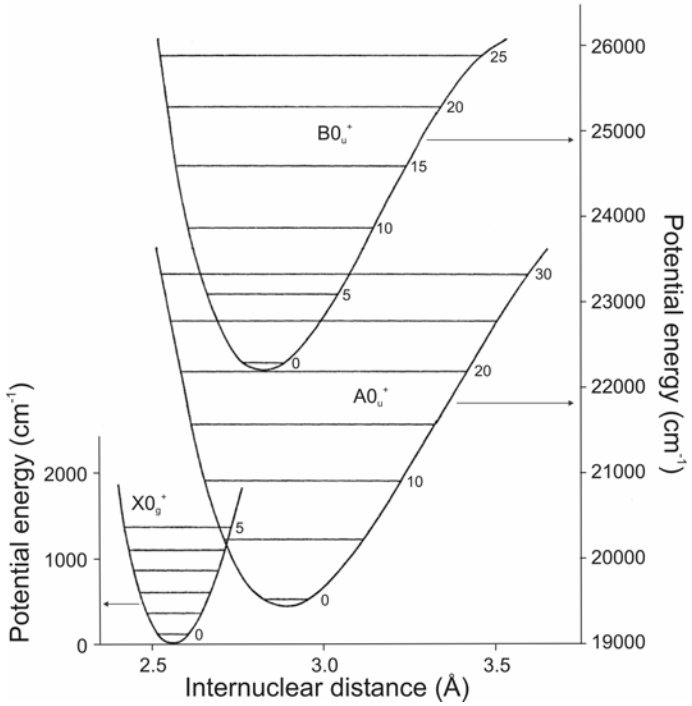

Figure 6.2. The energy level structure of the Te_2 molecule. The X, A and B electronic states are shown and the vibrational levels of each state are indicated. This diagram is based on one shown in the literature (Barrow and du Parcq 1972).

6.3 Experimental method

The experiments were performed using two extended-cavity diode lasers (ECDLs) emitting at around 410 nm and 451 nm respectively. These laser systems were described in detail in Chapter 2, and are capable of performing mode-hop free tuning over wide bandwidths. In the first part of the experiment, absorption spectra of $^{130}Te_2$ and fluorescence spectra of atomic indium were acquired simultaneously; the experimental set-up is shown in

Figure 6.3. Similar experiments were performed in turn with each of the two ECDLs.

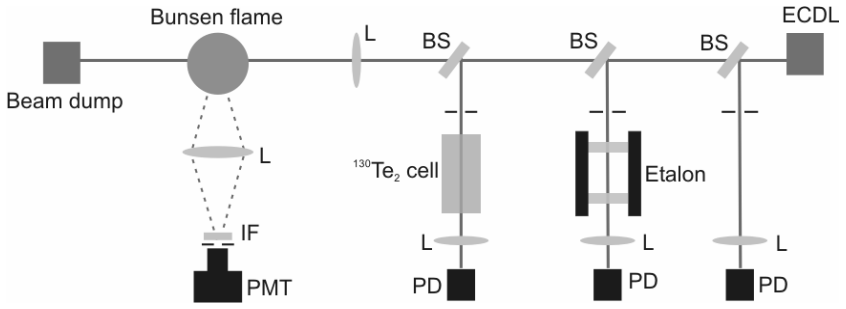

Figure 6.3. The experimental set-up for the simultaneous acquisition of $^{130}Te_2$ absorption spectra, and In fluorescence spectra. (L: lens; IF: interference filter centred around 451 nm; PMT: photomultiplier tube; PD: photodiode; BS: beam splitter; ECDL: extended-cavity diode laser)

Indium LIF spectra were acquired in the same way as outlined previously in Chapter 3. The Bunsen burner described in Chapter 4 was used to stabilise a slightly fuel-rich flame of methane and air. There was negligible absorption of the laser beam in the flame during these experiments, so no correction of the LIF spectra for this effect was required. The indium fluorescence spectrum was used to calibrate the frequency scale of the simultaneously acquired tellurium absorption spectra. Before passing through the flame, a part of the laser beam was reflected by a glass plate and directed towards a quartz cell containing isotopically pure $^{130}Te_2$ (Opthos Instruments; path length = 10 cm). The cell had been mounted in a ceramic furnace and was held at a constant temperature (670 ºC for the 410 nm laser experiment; 600 ºC in the case of the 451 nm laser) throughout the experiment; the temperature was measured by a thermocouple in contact with the exterior of the absorption cell. No buffer gas was present so the total pressure in the cell was equal to the vapour pressure of $^{130}Te_2$, which was estimated to be around 3 Torr.

Single-mode tuning of the laser wavelength was performed at a scan-rate of 20 Hz over a range of approximately 70 GHz. The intensity of the beam transmitted through the cell was measured by a photodiode. Another reflection of the main laser beam was directed on to a second photodiode as a reference intensity measurement. A third reflection from the laser beam was directed towards a Fabry-Perot etalon. The etalon transmission pattern was later used to linearise the frequency scale of the scans. The signals were digitised using a data acquisition card (National Instruments PCI-6014).

In the case of the 410 nm ECDL, the $^{130}Te_2$ spectrum was extended in the following manner. Having acquired $^{130}Te_2$ absorption spectra in the region that overlaps with the indium $5^2P_{1/2} \rightarrow 6^2S_{1/2}$ spectrum, the wavelength of the laser scan was shifted by temperature tuning of the diode laser. This allowed four overlapping regions of the spectrum (each of which was at least 55 GHz wide) to be recorded covering an overall spectral range of 170 GHz. In principle, this region could have been further extended by performing coarse tuning of the grating angle, for example through the use of a stepper motor.

In a second experiment, a proportional-integral (PI) control algorithm was used to achieve active stabilisation of the wavelength of the 410 nm ECDL by locking it to one of the strong lines in the spectrum of $^{130}Te_2$. This was done using software written by the present author in the LabVIEW environment. The laser locking was done in the following way: a single-mode scan of the laser wavelength was performed as described above, while viewing on an oscilloscope the measured intensity of the light transmitted through the heated $^{130}Te_2$ vapour cell. The spectral range of this scan was then narrowed down around the line of interest by reducing the amplitude (and dc offset) of the triangular waveforms used to modulate the grating position and the diode

laser injection current. Then the modulation was turned off and the PI control program (time constant = 100 ms) was activated. Its purpose was to record the intensity of the laser beam transmitted through the $^{130}Te_2$ cell and thereby to determine a control signal to add to the voltage on the piezo-actuators in the grating mount, thus adjusting the laser wavelength so as to return the value of transmitted intensity to the specified set-point.

6.4 Results and discussion

6.4.1 $^{130}Te_2$ absorbance spectra

Figure 6.4 shows simultaneously acquired spectra of $^{130}Te_2$ absorbance and atomic indium fluorescence (normalised by the simultaneously recorded laser output power). The spectra were obtained by taking the average of 100 individual single-mode wavelength scans. The scale shown is in vacuum wavenumbers; a correction was made for the pressure shift of the indium spectrum, which was estimated to be around -0.065 cm^{-1}, using the parameter for broadening of In by N_2 (Eberz et al. 1984). A theoretical fit of the sum of four Voigt profiles was made to the indium fluorescence spectrum in the same way as has been described in Chapter 3, and is also shown in Figure 6.4.

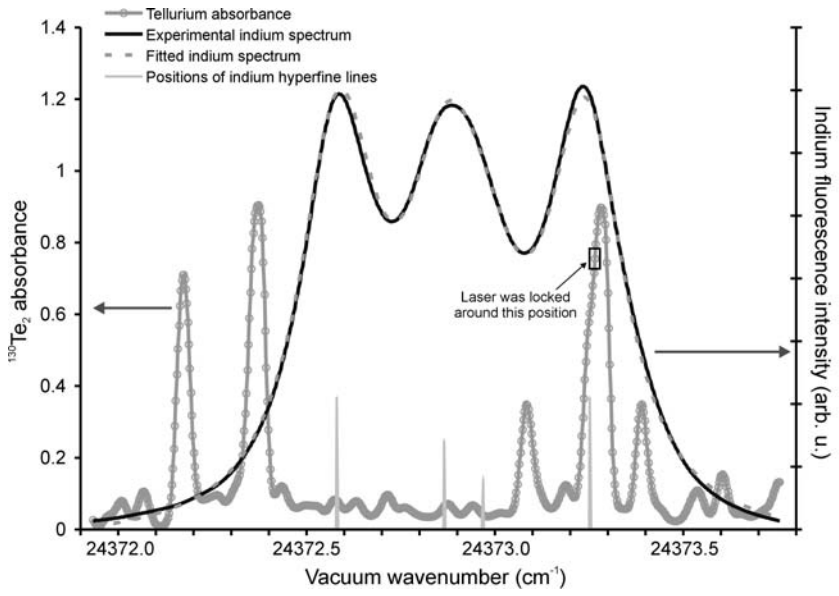

Figure 6.4 Spectra of simultaneously acquired $^{130}Te_2$ absorbance and In fluorescence in the $5^2P_{1/2} \rightarrow 6^2S_{1/2}$ transition. The spectra correspond to the average of 100 ECDL wavelength scans. Also shown are a theoretical fit of the sum of four Voigt profiles to the indium spectrum, and the locations of the indium hyperfine lines.

The good agreement between the experimental data and the fitted spectrum confirms that the laser was emitting on a single-mode throughout the scan. Since the absolute wavelengths of the four hyperfine components of the indium spectrum are known (Deverall et al. 1953), this allowed the absolute frequency scale of the scan to be established.

The composite spectrum shown in Figure 6.5 was obtained from the averaged $^{130}Te_2$ absorption spectra that were recorded for four overlapping wavelength ranges. At the positions where the recorded spectra overlapped, the average absorbance is shown.

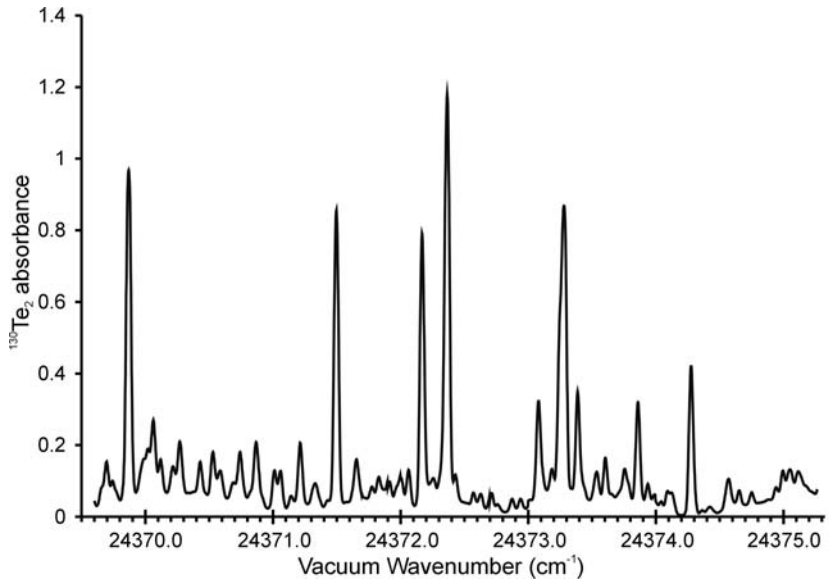

Figure 6.5 A composite spectrum of $^{130}Te_2$ absorbance compiled by making ECDL scans over four overlapping wavelength ranges.

There is a small degree of uncertainty in the absolute values of the absorbance because a slight etalon effect within the cell windows caused a weak ripple on the base line. Nonetheless, the line positions were of principal interest in this work. Several error sources resulted in a small inaccuracy in the determination of the line positions. The error results from uncertainties in the FSR of the etalon, the experimental determination of the position of the first hyperfine line, and the pressure shift for indium. Taken together, these result in an upper estimate of ±0.1 cm^{-1} for the $^{130}Te_2$ line positions shown on Figure 6.4 and in Table 6.1.

The features at 24,369.87 cm^{-1}, 24,372.37 cm^{-1} and 24,373.28 cm^{-1}, have been identified as being, respectively, the $X0_g^+ \rightarrow B0_u^+(15,0)R(96)$, $X0_g^+ \rightarrow B0_u^+(15,0)P(88)$, and $X0_g^+ \rightarrow B0_u^+(15,0)R(94)$ lines, since they agree to within the error margin with the line positions listed by (Jha et al. 1969), as shown in

Table 6.1. The nomenclature of the line $X0_g^+ \rightarrow B0_u^+(15,0)R(96)$, for example, means that $v'' = 0$, $v' = 15$, $J'' = 96$, and $J' = 97$.

Experimental line positions (cm^{-1})	Identified transitions	Positions listed by (Jha et al. 1969)	Calculation based on data of (Barrow and du Parcq 1972)
24 369.87	(15,0)R(96)	24 369.93	24 370.28
24 371.50	(17,1)P(104)		24 370.82
24 372.17	(17,1)R(110)		24 371.54
24 372.37	(15,0)P(88)	24 372.44	24 372.62
24 373.08	(16,0)R(148)		24 373.47
24 373.28	(15,0)R(94)	24 373.36	24 373.67
24 373.39			
24 373.86			
24 374.28	(16,0)R(154)		24 374.75

Table 6.1. The wavelengths of the $^{130}Te_2$ lines estimated from the experimental data, and selected line positions from the literature and from calculations based on spectroscopic data. All of the transitions listed are in the $X0_g^+ \rightarrow B0_u^+$ band. The maximum uncertainty in the experimental line positions has been estimated as ± 0.1 cm^{-1}.

The other lines observed here do not appear to correspond to any data that have been published in tabular form. In order to assign these, a simple calculation was made, based on published spectroscopic data (Barrow and du Parcq 1972), to predict the positions of the lines in a number of bands of the $X0_g^+ \rightarrow B0_u^+$ transition that are situated in this spectral region. The potentials of upper vibrational states ($\varepsilon_{v'}$) above the minimum of the potential curve of the ground electronic state are given by (Barrow and du Parcq 1972) in tabular form. The same authors give an equation to calculate the term values for the lower vibrational state:

$$\varepsilon_{v''} = \omega_e \left[1 - x_e \left(v + \frac{1}{2} \right) - y_e \left(v + \frac{1}{2} \right)^2 \right] \left(v + \frac{1}{2} \right) \qquad (6.6)$$

The values given for the constants are: $\omega_e = 247.07$, $x_e = 2.084 \times 10^{-3}$, and $y_e = 2.226 \times 10^{-6}$. The similarity to Eqn. 6.4 will be noted, but in this case a third-order term has been added to describe more accurately the behaviour of the anharmonic oscillation. This example confirms the statement above that $x_e << \omega_e$, but this effect must nevertheless be taken account of in order to predict the line positions with accuracy.

The rotational constants (B) for each vibrational level in the $X0_g^+$ and $B0_u^+$ states were determined empirically and are tabulated in the literature (Barrow and du Parcq 1972). These empirical coefficients take account of centrifugal distortion of the molecule, mentioned previously, and could thus be used to calculate the energies of rotational lines in the upper ($\varepsilon_{J'}$) and lower ($\varepsilon_{J''}$) electronic-vibrational states via $\varepsilon_j = BJ(J+1)$.

Taken together, these coefficients allowed the calculation of line-positions in the P- and R-branches (there is no Q-branch as already highlighted) via the following equation:

$$\Delta\varepsilon_{total} = \varepsilon_{v'} + \varepsilon_{J'} - \varepsilon_{v''} - \varepsilon_{J''} \qquad (6.7)$$

Table 6.1 lists the positions of lines predicted to be within the range of the spectrum shown in Figure 6.5.

The results of the calculation are of limited accuracy since they are derived from parameters that were found by least-squares fitting to experimental data (Barrow and du Parcq 1972) over a wide spectral range. Nevertheless, there is moderate agreement with the experimental data for the X→B (15,0) lines

identified above. The calculated line positions also indicate that two of the weaker lines shown in Figure 6.5, at 24,373.08 cm^{-1} and 24,374.28 cm^{-1}, are likely to be $X0_g^+ \rightarrow B0_u^+(16,0)P(148)$ and $X0_g^+ \rightarrow B0_u^+(16,0)R(154)$. A further two strong lines in the spectrum, at 24,371.50 cm^{-1} and 24,372.17 cm^{-1}, are likely to be the P(104) and R(110) lines of the $X0_g^+ \rightarrow B0_u^+(17,1)$ band. Although there is a discrepancy for this pair between the calculated and experimental line positions, there is a good agreement for the line spacing. This discrepancy is therefore likely to be the result of an inaccuracy in the data used in the calculation, such as in the term value for the $v''=1$ state or in the rotational constant of one of the levels of the transition. The two lines at 24,373.39 cm^{-1} and 24,373.86 cm^{-1} in the spectrum shown in Figure 6.5 have not being identified; it is probable that these could result from transitions with higher J'' values, or from overlapping weak lines.

As a comparison, the $^{130}Te_2$ absorbance spectrum acquired around 451.1 nm and overlapping with the $5^2P_{3/2} \rightarrow 6^2S_{1/2}$ is shown in Figure 6.6. An even greater density of $^{130}Te_2$ lines is observed in this spectral region. These are likely to be due to both the $X0_g^+ \rightarrow B0_u^+$ and the $X0_g^+ \rightarrow A0_u^+$ transitions, and no attempt to identify the individual lines was made in this case. Instead a comparison was made to the line positions plotted in the tellurium atlas (Cariou and Luc 1980), and it was found that there is close agreement in the positions of the fifteen strongest absorbance peaks shown here.

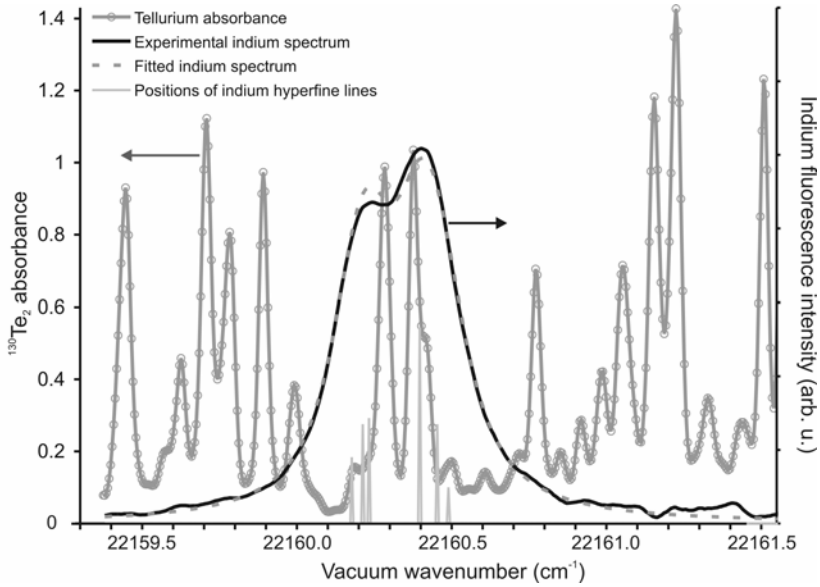

Figure 6.6 Spectra of simultaneously acquired $^{130}Te_2$ absorbance and In fluorescence in the $5^2P_{3/2} \rightarrow 6^2S_{1/2}$ transition. The spectra correspond to the average of 100 ECDL wavelength scans. Also shown are a theoretical fit of the sum of six Voigt profiles to the indium spectrum, and the locations of the indium hyperfine lines.

6.4.2 Laser-locking

The violet ECDL was locked to the $X0_g^+ \rightarrow B0_u^+$ (15,0)R(94) $^{130}Te_2$ line at a frequency of 24,373.3 cm^{-1}, as indicated in Figure 6.4. The variations in transmitted intensity of the locked laser were translated into frequency fluctuations using the gradient of the line (change in transmitted intensity per MHz), which was calculated from a spectrum that was recorded immediately prior to the laser-locking experiment. The variation of the laser frequency as a function of time is plotted in Figure 6.7; the sampling interval was 100 ms. It can be seen that the laser frequency fluctuates around a mean value, rarely deviating by more than 30 MHz (i.e. < 1 part in 10^7); no long term drift in the laser frequency was observed. One outlying data point is apparent in Figure

6.7, and this may be the result of a mechanical disturbance. The control signal increased gradually throughout the experiment, corresponding to a shortening of the extended cavity, to compensate for an apparent increase in the ambient temperature or pressure. In order to stabilise the laser wavelength over longer time periods, it would be necessary to achieve a greater degree of passive stability by improving the temperature stabilisation and pressure isolation of the laser housing (Talvitie et al. 1997).

Also shown in Figure 6.7 is a histogram of differences from the mean frequency, along with a fitted Gaussian (FWHM = 39.1 MHz). When compared to the typical transition widths at atmospheric pressure, such as that of the $5^2P_{1/2} \rightarrow 6^2S_{1/2}$ transition of atomic indium shown in Figure 6.4, the fluctuations in the intensity of the locked laser are very small. This set-up is therefore shown to be appropriate to use for frequency stabilisation of diode lasers for use in gas sensing applications at atmospheric pressure.

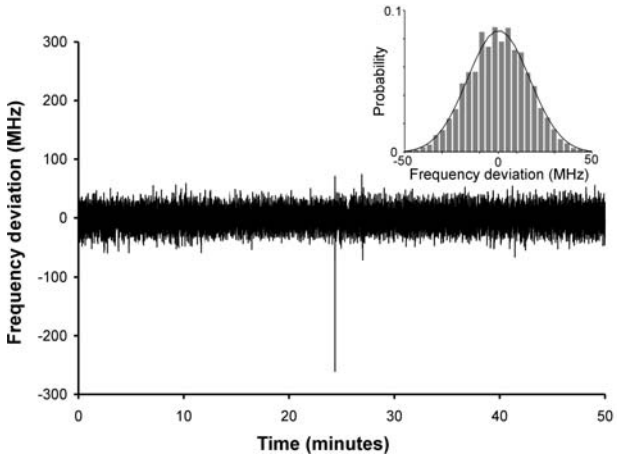

Figure 6.7. Variation in frequency of the actively locked 410 nm ECDL; the variation was calculated from the fluctuations in the intensity of the laser beam transmitted through the $^{130}Te_2$ absorption cell. Insert: Histogram of deviations from the mean laser frequency.

6.5 Conclusions

It has shown that there are strong $^{130}Te_2$ absorption lines suitable for use in frequency referencing of laser scans and for active locking of lasers at wavelengths overlapping with the $5^2P_{1/2}\rightarrow 6^2S_{1/2}$ and $5^2P_{3/2}\rightarrow 6^2S_{1/2}$ transitions of atomic indium at wavelengths of around 410.2 nm and 451.1 nm respectively. In the former case this is below the spectral range covered by the tellurium atlas (Cariou and Luc 1980), which stops at 417 nm. The 410 nm ECDL was stabilised to one of the Te_2 lines and the frequency fluctuations were within the range of 40 MHz, which is negligible compared to typical transition widths at atmospheric pressure. It has been noted that a number of atomic and molecular species have strong electronic transitions in the wavelength range 394 nm to 417 nm, and frequency-referencing and laser-locking techniques based on $^{130}Te_2$ absorption could therefore find application in gas sensing experiments.

The overall purpose of the present project is the measurement of flame temperatures using diode-laser TLAF. As mentioned at the beginning of this Chapter, the wavelength-locking technique described here could be useful in this context. One way of increasing the temporal resolution of the temperature sensor would be to lock each of the two ECDLs to overlap with the respective indium transitions, and then to switch rapidly between the two beams using an optical chopper. In this way the integrated line strength would no longer be measured but the intensity of the fluorescence at one point on the spectrum is proportional to the integrated line-strength. The ratio of the two fluorescence signal would thus be related to the temperature, although a calibration constant 'C' would be required, whose value would depend on

the positions at which the lasers were stabilised. Since the lasers remain at full power and well-overlapped with the indium transitions, this method would maximise the signal-to-noise ratio, which is an important consideration for high-temporal resolution measurements. It is therefore worth pursuing this laser-locking approach as a part of the effort to achieve high-speed TLAF thermometry suitable to dynamic combustion systems.

References

Banwell, C. N., McCash, E.M. (1994). Fundamentals of Molecular Spectroscopy. London, McGraw-Hill.

Barrow, R. F. and R. P. du Parcq (1972). "Rotational Analysis of the A 0_u^+, B 0_u^+-X 0_g^+ systems of gaseous Te_2." Proceedings of the Royal Society of London, Series A: Mathematical and Physical Sciences **327**: 279-287.

Burns, I. S., J. Hult and C. F. Kaminski (2006). "Use of $^{130}Te_2$ for frequency referencing and active stabilisation of a violet exended cavity diode laser." Spectrochimica Acta, Part A: Molecular Spectroscopy **in press**.

Cacciani, P., W. Hogervorst and W. Ubachs (1995). "Accidental predissociation phenomena in the $E^1\Pi$, ν=0 and ν=1 states of $^{12}C^{16}O$ and $^{13}C^{16}O$." Journal of Chemical Physics **102**: 8308-8320.

Cancio, P. and D. Bermejo (1997). "Absolute wavelengths in $^{130}Te_2$: new reference lines for laser spectroscopy coinciding with emissions of the Ar^+ laser." Journal of the Optical Society of America B: Optical Physics **14**(6): 1305-1311.

Cariou, J. and P. Luc (1980). Atlas du spectre d'Absorption de la Molecule Tellure. Paris, CNRS.

Deverall, G. V., K. W. Meissner and G. J. Zissis (1953). "Hyperfine Structures of the Resonance Lines of Indium (In^{115})." Physical Review **91**(2): 297-299.

du Parcq, R. P. and R. F. Barrow (1966). "The Internuclear Distance of the Te_2 Molecule." Chemical Communications: 270a.

Eberz, J., G. Huber, T. Kuhl and G. Ulm (1984). "Pressure Broadening and Pressure Shift of the 410-Nm Indium Line Perturbed by Foreign Gases." Journal of Physics B-Atomic Molecular and Optical Physics **17**(15): 3075-3082.

Eckbreth, A. C. (1996). Laser Diagnostics for Combustion Temperature and Species. Amsterdam, Gordon and Breach.

Gerstenkorn, S. and P. Luc (1978). Atlas du Spectre d'Absorption de la molecule d'Iode. Paris, CNRS.

Hayasaka, K. (2002). "Frequency stabilization of an extended-cavity violet diode laser by resonant optical feedback." Optics Communications **206**(4-6): 401-409.

Herzberg, G. (1950). Molecular Spectra and Molecular Structure. New York, Van Nostrand Reinhold.

Hori, M., R. S. Hayano, E. Widmann and H. A. Torii (2003). "Resolution enhancement of pHe^+ atomic line profiles measured with a pulsed dye laser and a Fizeau wavelength meter." Optics Letters **28**: 2479-2481.

Hult, J., I. S. Burns and C. F. Kaminski (2005). "Two-line atomic fluorescence flame thermometry using diode lasers." Proceedings of the Combustion Institute **30**: 1535-1543.

Jha, B. L., K. V. Subbaram and D. Ramachandra Rao (1969). "Electronic Spectra of $^{130}Te_2$ and ^{128} Te_2." Journal of Molecular Spectroscopy **32**: 383-397.

Kaminski, C. F., I. G. Hughes and P. Ewart (1997). "Degenerate four-wave mixing spectroscopy and spectral simulation of C_2 in an atmospheric pressure oxy-acetylene flame." Journal of Chemical Physics **106**: 5324-5332.

Park, C. Y. and T. H. Yoon (2003). "Frequency stabilisation of injection-locked violet diode laser with Doppler-free absorption signal of ytterbium." Japanese Journal of Applied Physics, Part II: Letters **42**: L754-L756.

Raab, C., J. Bolle, H. Oberst, J. Eschner, F. Schmidt-Kaler and R. Blatt (1998). "Diode laser spectrometer at 493 nm for single trapped Ba^+ ions." Applied Physics B: Lasers and Optics **67**: 683-688.

Talvitie, H., A. Pietilainen, H. Ludvigsen and E. Ikonen (1997). "Passive frequency and intensity stabilization of extended-cavity diode lasers." Review of Scientific Instruments **68**(1): 1-7.

Chapter 7

Conclusions and Future Work

7.1 Conclusions

This thesis has described the development of an innovative flame thermometry technique, which has been used to perform spatially resolved temperature measurements in laminar flames. An improved design for extended cavity diode lasers (ECDLs) was conceived, in which the technique of using a multi-piezo actuator grating mount to optimise independently the tuning rates of the extended cavity length and grating angle, was combined with simultaneous tuning of the diode current. Two such laser systems were built, emitting at wavelengths of around 410 nm and 451 nm respectively, and these were found to possess the favourable tuning properties required for high-resolution spectroscopy. Significantly greater mode-hop free tuning ranges (> 90 GHz) were achieved than have previously been reported for blue ECDLs.

The two ECDLs were used to perform high resolution spectroscopy of the $5^2P_{1/2} \rightarrow 6^2S_{1/2}$ and $5^2P_{3/2} \rightarrow 6^2S_{1/2}$ transitions of neutral indium atoms seeded to atmospheric pressure flames. The extremely narrow line-width of the ECDLs (measured to be less than 8 MHz) allowed high resolution fluorescence

spectra to be recorded. The spectra show excellent agreement with theoretical fits based on a sum of Voigt profiles representing the individual hyperfine components of the transition.

The two ECDLs were then used to implement flame temperature measurements based on the principle of two-line atomic fluorescence. A single detector approach was adopted so that the calibration constant mentioned in previous TLAF studies was no longer needed. Temperature measurements were successfully performed in a laminar Bunsen flame and the vertical and horizontal temperature profiles show good agreement with the literature.

An alternative thermometry scheme was developed whereby spatially-resolved temperature measurements could be performed using a single diode laser by analysing the fluorescence line-shape. The results of these measurements show good agreement with reference measurements and simulation results. This represents a further simplification of the experimental set-up required for flame thermometry.

Finally, a strategy was considered to increase the temporal resolution of the temperature measurements for future implementation in turbulent flames. A method of locking the laser wavelengths to resonance lines of molecular tellurium was demonstrated, and the laser was stabilised to within 40 MHz, which is negligible compared to the transition width of indium at atmospheric pressure. Locking the laser wavelengths near the peaks of the indium transitions would have the advantage of maximising the signal strength, therefore optimising the precision of the measurements.

7.2 Future Work

In this section, some brief remarks will be made about a number of possible extensions to this research. These areas include: thermometry in sooting flames, increasing the temporal resolution of the measurements for application to turbulent combustion, and investigation of novel techniques for rapid scanning of the ECDL wavelength.

7.2.1 Measurements in sooting flames

Firstly, the TLAF thermometry technique has the potential to be implemented in sooting flames, in which many other laser diagnostics are subject to interferences. In fact, the TLAF technique is especially well-suited to implementation in sooting flames since the consumption of indium atoms to form InOH occurs at a slower rate in fuel rich flames than in lean flames. Studies of sooting flames are often conducted in low pressure burners and such an environment would also be of interest, due to the shallower gradient at the flame front, which could potentially be resolved with TLAF due to the small measurement volume. For implementation in sooting flames a two-detector scheme would be required, since resonance fluorescence is unsuitable in particle-laden systems due to strong light scattering. Since the line-shape temperature measurement could also be implemented in sooting flames, a comparison of the two approaches could be made.

7.2.2 Measurements in turbulent flames

It was shown in Chapter 4 that the fluorescence signal levels obtained are sufficient to perform temperature measurements with a temporal resolution of

10 kHz, which would allow the study of turbulent flames. The rapid TLAF measurements would be performed by actively locking the laser wavelengths, as described in Chapter 6, and switching between the two beams using a mechanical chopper. This approach represents a convenient strategy for obtaining high-repetition rate measurements, since the excitation sources are continuous-wave. These would provide an insight into the dynamics of temperature fluctuations in turbulent combustion.

7.2.3 Rapid modulation of ECDL wavelength

A strategy has been developed during the present research for tuning the wavelength of ECDLs much faster than is usually possible (Hult et al. 2005). These results have not been presented in this thesis due to the limitations of space, but they represent another exciting aspect of the project. The restriction imposed on the tuning rate by the need for mechanical movement of the grating is obviated here by tuning only the diode laser injection current. This causes the laser to mode-jump between different extended cavity modes. At times the wavelength jumps to a mode that is off-resonance with the indium transition, subsequently returning to resonance after further mode-hops. This leads to a spectrum comprised of peaks that are separated by the free-spectral range of the extended cavity as shown in Figure 7.1. The spectrum shown here was recorded at a scanning frequency of 10 kHz. The LIF spectrum is obtained from the raw data by extracting the locations of the peaks in signal intensity. Also shown in Figure 7.1 is a theoretical spectrum; it can be seen that the peak positions in the experimental spectrum lie close to the theoretical spectrum.

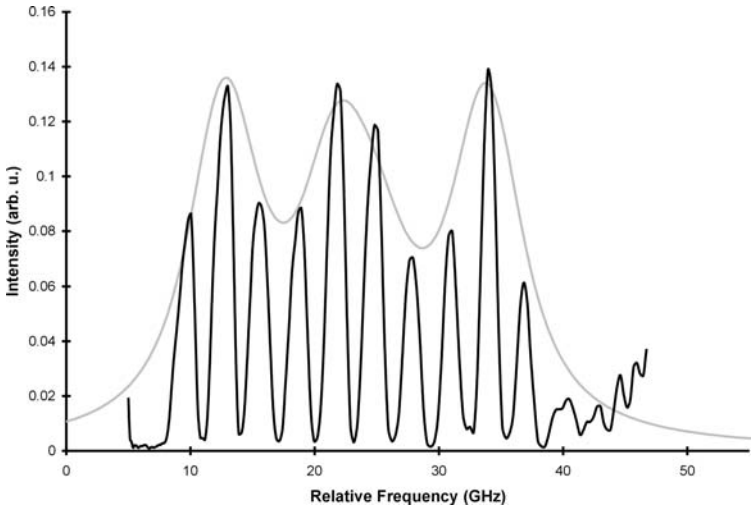

Figure 7.1. A fluorescence spectrum of the $5^2P_{1/2} \rightarrow 6^2S_{1/2}$ transition of atomic indium recorded in a time of 100 μs by tuning only the laser current. The darker line is the experimental data. The peak positions on this trace are extracted to form the LIF spectrum. A theoretical spectrum is also shown.

This novel rapid tuning approach opens possibilities for implementation of flame temperature measurements by either TLAF or by the line-shape technique, and could also find application in other high-speed spectroscopy experiments.

References

Hult, J., I. S. Burns and C. F. Kaminski (2005). "High repetition-rate wavelength tuning of an extended cavity diode laser for gas phase sensing." Applied Physics B **81**: 757.

Appendix A

Calculation of the optimal theoretical ratio of piezo-actuator extensions for single-mode wavelength tuning

As was noted in Chapter 2, it is possible to calculate theoretically the ratio of the extensions that must be generated in each of the piezo-actuators in the grating mount to achieve optimal conditions for mode-hop free tuning. The derivation of this relationship is presented in this Appendix.

Figure A1 shows a plan view of the extended-cavity diode laser (ECDL) configuration. At the right hand side of the main figure, there are two piezo-actuators one above the other which are always moved synchronously and are collectively denoted ‘B’ as was represented in Figure 2.4.

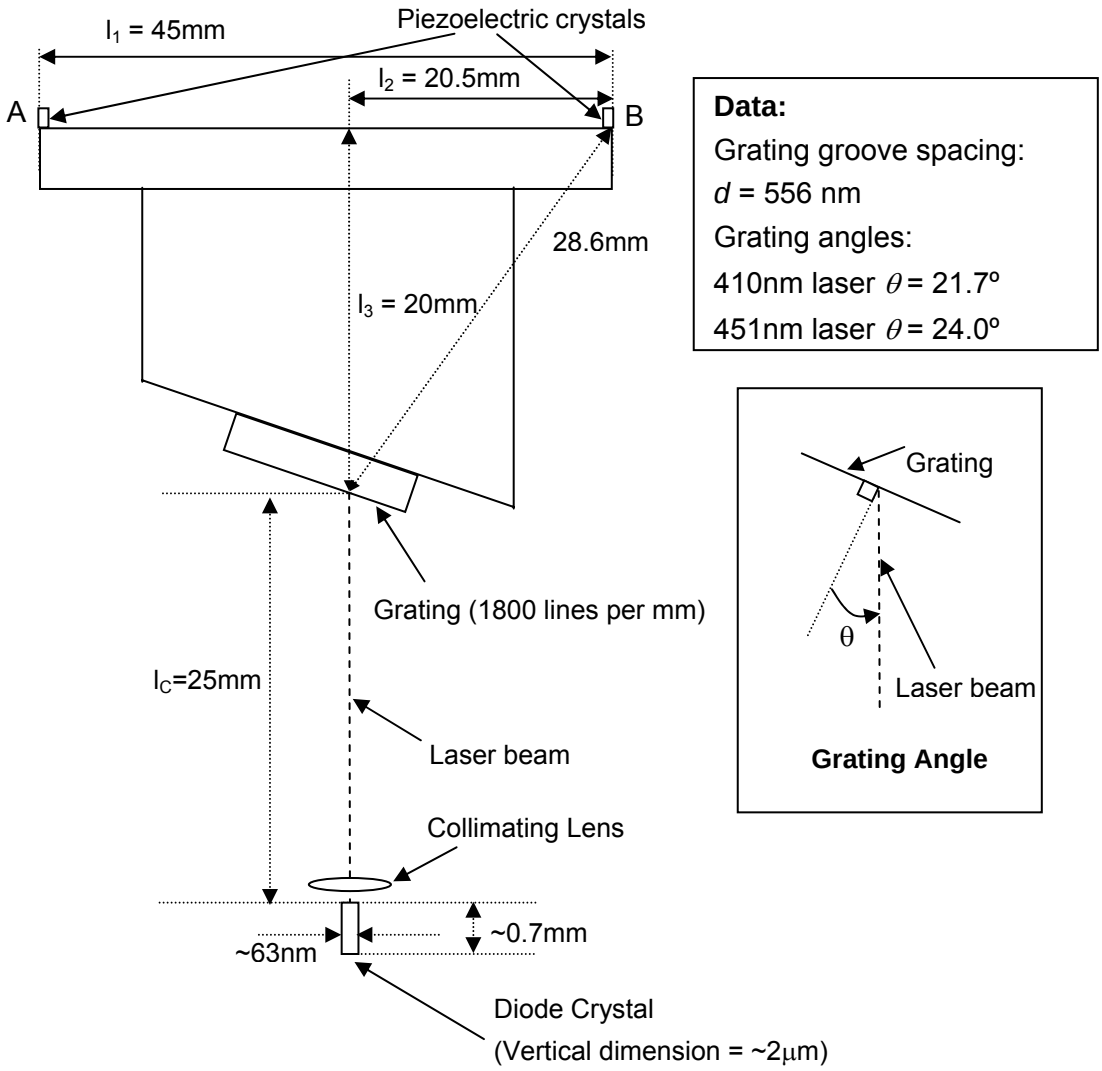

Figure A1. Configuration of the external cavity laser with indication of important dimensions used in calculations.

The objective is to calculate the ratio between the length change of the piezo-actuator denoted 'A' to that of piezo-actuators 'B' to obtain the correct proportion between translation and rotation. This allows the tuning of the grating feedback profile to be matched with the tuning of the extended cavity mode structure. If we consider applying a voltage ramp to piezo-actuator 'A' only, then grating rotation by angle $\Delta\theta$

will result, as shown in Figure A2. The rotation will be about a pivotal axis defined by the two piezo-actuators at B. The translation of the grating is performed by an additional voltage modulation applied to all three piezo-actuators synchronously (for 'A' this is simply added to the "pivot" signal). The result is a change in the cavity length of the laser.

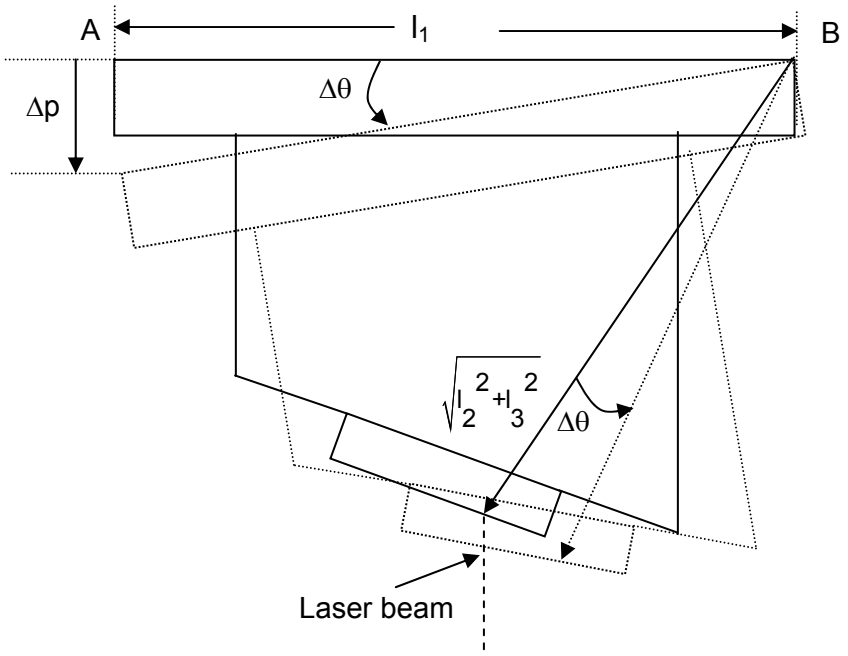

Figure A2. Rotation of the grating.

Let Δp be that part of ΔA which causes the angle change:

$$\Delta p = \Delta A - \Delta B \qquad \text{(A1)}$$

The positive direction of Δp is considered to be downward as indicated in Fig A2. Note that for the angle change shown in Figure A2, $\Delta\theta$ is negative.

$$\tan(\Delta\theta) = -\Delta p / l_1 \qquad \text{(A2)}$$

Since $\Delta\theta$ is tiny (of order 0.01°), it can be assumed that:

$$\tan(\Delta\theta) \approx \sin(\Delta\theta) \approx \Delta\theta \quad \text{(A3)}$$

$$\Delta\theta = -\Delta p / l_1 \quad \text{(A4)}$$

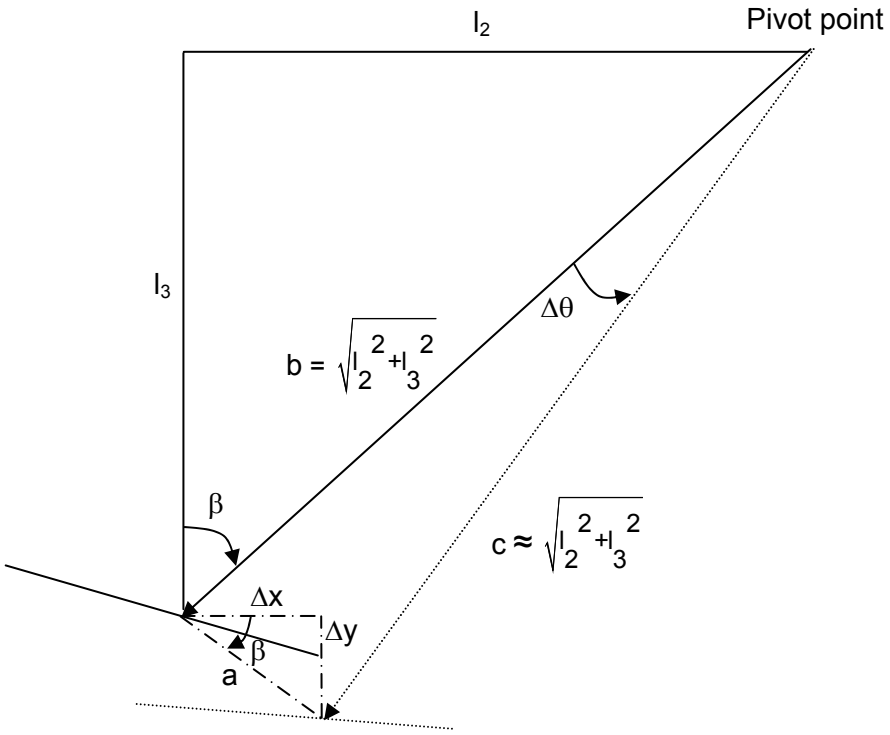

Figure A3. Longitudinal translation of the grating as it rotates.

The grating can be thought of as rotating through $\Delta\theta$ around the point at which the laser was initially incident and then translating distance a, as is represented in Figure A3. For small angle changes, the direction of movement a is perpendicular to line b. Application of the cosine rule gives:

$$a^2 = b^2 + c^2 - 2bc\cos(\Delta\theta) \quad \text{(A5)}$$

$$|a| = \sqrt{2\left(l_2^{\,2} + l_3^{\,2}\right)\left(1 - \cos\left(\Delta\theta\right)\right)} \tag{A6}$$

The translation of the grating resulting from the angle change can be represented as two perpendicular components (Δx and Δy) as shown in Figure A3.

$$\Delta x = a\cos\beta \quad = a\frac{l_3}{\sqrt{l_2^{\,2} + l_3^{\,2}}} \tag{A7}$$

$$\Delta y = a\sin\beta \quad = a\frac{l_2}{\sqrt{l_2^{\,2} + l_3^{\,2}}} \tag{A8}$$

As noted by Levin (Levin 2002), the parameter that is crucial in changing the number of standing wave nodes present in the cavity is not the extension of the cavity itself but the movement of the individual grating grooves towards the diode, represented by the movement Δy alone. Combining Eqn. A6 and Eqn. A8 we obtain:

$$\Delta y = l_2\sqrt{2\left(1 - \cos\left(\Delta\theta\right)\right)} \tag{A9}$$

For small angles, we approximate:

$$\cos\left(\Delta\theta\right) \approx \sqrt{1 - \left(\Delta\theta\right)^2} \tag{A10}$$

From which the following can be obtained after substitution into Eqn. A9.

$$\left(\Delta y\right)^2 = 2l_2^{\,2}\left(1 - \sqrt{1 - \left(\Delta\theta\right)^2}\right) \tag{A11}$$

$$1-(\Delta\theta)^2 = 1-\frac{(\Delta y)^2}{{l_2}^2}+\frac{(\Delta y)^4}{4{l_2}^4} \tag{A12}$$

Since $\Delta y^2 >> \Delta y^4$, and by substitution of Eqn. A4, one finally obtains:

$$\Delta y = \Delta p \frac{l_2}{l_1} \tag{A13}$$

The change in the central wavelength of the grating feedback profile corresponding to a specific angle θ is given by:

$$2d\sin\theta = \lambda \tag{A14}$$

Here, d is the grating groove spacing (m). For small changes, one obtains by differentiation:

$$\Delta\lambda = 2d\cos\theta\ \Delta\theta \tag{A15}$$

Having established the relationship between angle change ($\Delta\theta$) and the shift in the central wavelength of the optical feedback ($\Delta\lambda$), let us now determine the magnitude of the longitudinal grating translation (Δl_C) required to avoid mode hops. The number of standing waves in the cavity is given by:

$$N_C = \frac{2l_C}{\lambda} \tag{A16}$$

Here, l_C is the external cavity length. Hence, for small changes:

$$\Delta l_C = \frac{N_C}{2}\Delta\lambda = \frac{l_C}{\lambda}\Delta\lambda \tag{A17}$$

Substitution of Eqns. A4 and A15 gives:

$$\Delta l_C = -\frac{2d\cos\theta\ l_C \Delta p}{\lambda\ l_1} \tag{A18}$$

By then substituting Eqn. A14, the following is obtained:

$$\Delta l_C = -\frac{l_C \Delta p}{l_1}\sqrt{\frac{4d^2}{\lambda^2}-1} \tag{A19}$$

Now we can find the final ratio between the extensions of piezo-actuators 'A' and 'B', to give optimal mode-hop free tuning:

$$\Delta B = -\Delta l_C - \Delta y \tag{A20}$$

$$\Delta A = \Delta p + \Delta B \tag{A21}$$

$$\frac{\Delta A}{\Delta B} = 1 + \frac{\Delta p}{-\Delta l_C - \Delta y} \tag{A22}$$

Therefore by substitution of Eqns. A13 and A19, the following relationship is obtained:

$$\frac{\Delta A}{\Delta B} = 1 + \frac{l_1}{l_C\sqrt{\frac{4d^2}{\lambda^2}-1} - l_2} \tag{A23}$$

Equation A23 describes the theoretical ratio of extensions in the piezo-actuators that would lead to the maximum mode-hop free tuning range.

The required tuning of the diode laser injection current will now be addressed. The objective here is to develop an equation that relates the amplitude of the current

tuning signal (ΔI) to the amplitudes of the extensions of the piezo-actuators (ΔA and ΔB). The number of standing-wave nodes (N_D) in the diode Fabry-Perot cavity is related to the cavity length (l_D) by the following equation:

$$l_D = N_D \lambda / 2n \tag{A24}$$

Here, n is the refractive index of the diode crystal. As has been noted in Chapter 2, we shall assume a linear relationship between the tuning of the diode injection-current and the laser wavelength:

$$\Delta\lambda = \beta \Delta I = \frac{2n}{N_D} \Delta l_D \tag{A25}$$

The last step here is taken by differentiation of Eqn. 2.3. A linear proportionality between the piezo-actuator driving voltage and its extension has also been assumed in Chapter 2.

$$\alpha = \frac{\Delta B}{\Delta V_B} = \frac{\Delta A}{\Delta V_A} \tag{A26}$$

The relationship will describe the ratio between the current tuning and the tuning of the 'B' piezo-actuators:

$$\frac{\Delta I}{\Delta V_B} = \frac{\alpha \Delta \lambda}{\beta \Delta B} \tag{A27}$$

By substitution of Eqns. A17 and A20:

$$\frac{\Delta I}{\Delta V_B} = \frac{\alpha \lambda}{\beta l_C} \frac{\Delta l_C}{\Delta B} = -\frac{\alpha \lambda}{\beta l_C} \left(1 + \frac{\Delta y}{\Delta B} \right) \tag{A28}$$

Then, by substitution of Eqns. A13 and A21:

$$\frac{\Delta I}{\Delta V_B} = -\frac{\alpha\lambda}{\beta l_C}\left(1+\frac{\Delta A}{\Delta B}\frac{l_2}{l_1}-\frac{l_2}{l_1}\right) \tag{A29}$$

Finally, by substitution of Eqn. A26:

$$\frac{\Delta I}{\Delta V_B} = \frac{\alpha\lambda}{\beta l_C}\left(\frac{l_2}{l_1}\left(1-\frac{\Delta V_A}{\Delta V_B}\right)-1\right) \tag{A30}$$

Note that Eqn. A30 can be used to calculate the required current tuning signal for *any* ratio of piezo-actuator tuning signals, not only the optimal one specified by Eqn. A23.

References

Levin, L. (2002). "Mode-hop-free electro-optically tuned diode laser." Optics Letters **27**(237-239).